F-region Dusk Ion Temperature Spikes at the Equatorward Edge of the High Latitude Convection Region

A Thesis Submitted to the
College of Graduate Studies and Research
in Partial Fulfillment of the Requirements
for the degree of Master of Science
in the Department of Physics and Engineering Physics
University of Saskatchewan
Saskatoon

By
Lindsay Victoria Goodwin

Permission to Use

In presenting this thesis in partial fulfilment of the requirements for a Postgraduate degree from the University of Saskatchewan, I agree that the Libraries of this University may make it freely available for inspection. I further agree that permission for copying of this thesis in any manner, in whole or in part, for scholarly purposes may be granted by the professor or professors who supervised my thesis work or, in their absence, by the Head of the Department or the Dean of the College in which my thesis work was done. It is understood that any copying or publication or use of this thesis or parts thereof for financial gain shall not be allowed without my written permission. It is also understood that due recognition shall be given to me and to the University of Saskatchewan in any scholarly use which may be made of any material in my thesis.

Requests for permission to copy or to make other use of material in this thesis in whole or part should be addressed to:

Head of the Department of Physics and Engineering Physics
163 Physics Building
116 Science Place
University of Saskatchewan
Saskatoon, Saskatchewan
Canada
S7N 5E2

Abstract

By examining continuous data from the Poker Flat Incoherent Scatter Radar (PFISR) in Poker Flat, Alaska, short-lived enhancements in the F-region ion temperature, or "T_i spikes", were discovered in the evening while the radar was on the equatorward edge of the high latitude convection region. These enhancements were several hundred Kelvin above the background temperature, would last less than 15 minutes and were preceded by sharp depletions in plasma density (of roughly one half). Though they were mostly detected in the summer, 25 events throughout a whole year of data were identified in which the spike occurred within 1.5 hours of the density drop. By examining the location of PFISR at the time of the enhancements, as well as the conditions under which these spikes occurred, it was concluded that these enhancements were the result of electric fields increasing the frictional heating between ions and neutrals. By then examining geophysical data, it was found that these events were temporal and related to changes in magnetic indices. One possible explanation for the observations is that the electric field is at its strongest near the plasmapause during substorms. Another more likely possibility is that during substorms the region of sunward ion convection expands into a region in the evening side where the neutral gas moves in a direction opposite to the ions, thereby enhancing the frictional heating rate.

Acknowledgements

I would first like to thank my supervisor, Dr. Jean-Pierre St-Maurice, who gave me the opportunity to come to the University of Saskatchewan and work on this project. I am very grateful for his encouragement, advice and his push for me to be my best. I truly feel blessed to have had such a supervisor for my Master's thesis. As well, I would like Dr. Phil Richards, whose discussions with Dr. St-Maurice resulted in this work.

Several organizations and groups made this work possible. I would like to thank the University of Saskatchewan for providing circumstances under which I could receive a Master's. I wish to thank NSF, NSERC and the CSA for funding this project in one form or another. Additionally, I would like to thank the NSF for providing funding for me to attend the 2012 ISR School and CEDAR 2013. For providing equipment and data vital to this work, I wish to thank SRI International, PFISR, DMSP, Madrigal, SuperDARN and the World Data Center for Geomagnetism, Kyoto.

Last, but not least, I wish to thank my family and friends for their love and support. A special "thank you" is reserved for my Grandpa, Glen Pridham and Cody Crewson who all truly helped me feel at home in Saskatoon.

Contents

List of Tables

List of Figures

List of Abbreviations

AC	Alternating Code
AMISR	Advanced Modular Incoherent Scatter Radar
CTIPe	Coupled Thermosphere Ionosphere Plasmasphere electrodynamics
EUV	Extreme Ultra-Violet
DMSP	Defense Meteorological Satellite Program
DTNL	Distant Tail Neutral Line
FTE	Flux Transfer Events
HF	High Frequency
IMF	Interplanetary Magnetic Field
IPY	International Polar Year
ISR	Incoherent Scatter Radar
MLT	Magnetic Local Time
MSIS	Mass Spectrometer and Incoherent Scatter radar
NASA	National Aeronautics and Space Administration
NENL	Near Earth Neutral Line
NSF	National Science Foundation
PFISR	Poker Flat Incoherent Scatter Radar
RADAR	RAdio Detection And Ranging
RISR	Resolute Bay Incoherent Scatter Radar
RTI	Range-Time-Intensity
SAIDs	Sub-Auroral Ion Drifts
SAPS	Sub-Auroral Polarization Streams
SRI	Stanford Research Institute
SuperDARN	Super Dual Auroral Radar Network
UT	Universal Time
UV	Ultra-Violet

List of Nomenclature

$\mathbf{B}$	Geomagnetic field strength
$\mathbf{E}$	Electric field
$\mathbf{E}'$	Electric field in the frame of neutrals
e	Charge of an electron
f_0	Normalized one-dimensional velocity distribution function
H	Scale height
J	Current density
$\mathbf{k}$	Wavenumber, $\mathbf{k}_i - \mathbf{k}_s$
$\mathbf{k}_i$	Scattered wavenumber
$\mathbf{k}_s$	Incident wavenumber
k_b	Boltzmann constant
m	Mass
n	Number density
$\mathbf{P}$	Stress tensor
P	Pressure, nk_bT
$\mathbf{p}$	Parameter vector
p	Momentum
$\mathbf{q}$	Heat flow
q	Charge of a particle
$q(z^*)$	Production rate when $\theta = 0^\circ$ for a reduced height
q_{max}	Maximum production rate when $\theta = 0^\circ$ for a given reduced height
S	Spectral density function
T	Temperature
t	Time
$\mathbf{V}$	Velocity
w	Plasma dispersion
y	Data
z	Altitude
z^*	Reduced altitude
$\frac{D}{Dt}$	Convective derivative $(\frac{\partial}{\partial t} + \mathbf{V}_i \cdot \nabla)$
ω	Angular frequency, $\omega_i - \omega_s$
ω_i	Incident angular frequency
ω_s	Scattered angular frequency
ϵ	Dielectric function, $1 + G_e + G_i$
γ	Dampening term
ρ	Mass density
Ω	Cyclotron frequency
ν_{12}	Particle 1-particle 2 collisional frequency
ψ_{in}	Correction function for ion-neutral interaction
ϕ_{in}	Correction function for ion-neutral interaction

λ_D	Debye length
σ	Uncertainty
σ_P	Pedersen conductivity
σ_H	Hall conductivity
τ^*	Optical depth when $\theta = 0^\circ$
θ	Solar zenith angle
α, i, e, n	If not otherwise stipulated, these are the subscripts to charges (general), ions, electrons, and neutrals, respectively

Chapter 1

Introduction

Incoherent Scatter Radars (ISRs) are powerful tools for examining the upper atmosphere. By sending out radio waves that probe small wave amplitudes and receive backscatter echoes that have bounced off high altitude plasma, high resolution information about the ionosphere can be obtained. These ISRs allow one to measure such parameters as electron density, electron and ion temperature, and ion velocity. From these, it is then possible to infer other properties of the upper atmosphere, such as electric fields. This is an important capability of ISRs because electric fields play a key role in high altitude phenomenology.

Given that ISRs probe waves produced by thermal noise they require a lot of power, and it is rare for ISR measurements to be taken continuously. However, by lowering the time resolution to conform to power constraints, the International Polar Year (IPY) experiment that used the Poker Flat Incoherent Scatter Radar (PFISR) was able to provide information regularly for most days within a year's worth of data. This experiment provided a unique opportunity to observe continuously while effects of Earth's rotation and/or magnetic activity moved PFISR into and out of ionospheric regions that mapped to the plasmasheet or the plasmasphere, given the latitude of PFISR. This opened the possibility for new phenomena to be discovered as shown in this thesis.

This thesis revolves around the discovery of sudden short lived ion temperature enhancements, or "spikes", found in the IPY dataset. In particular for a span of 9 days, the spikes occurred daily during quiet to moderate conditions when the radar was in the evening sector near the auroral boundary. The motivation behind this thesis is to unravel the origin of these ion temperature enhancements.

The present thesis will provide evidence that the ion temperature spikes were due to electric field spikes. In order to reach this conclusion several ionospheric processes must be

understood, including the chemistry, the electrodynamics and the energetics of the region. As well, we require a look into the principles underlying the operation of ISRs and an understanding of the specific radar being used for this work. These topics will be covered in the rest of this Chapter and Chapter 2.

The steps taken to come to the conclusion that the ion temperature enhancements were caused by electric field enhancements are outlined in Chapter 3. First, the events of interest were isolated and examined in relation to SuperDARN convection maps that are coincident in time and space. Next, the cause of coincident electron density depletions was found by investigating both the ion temperature and electron density through line and epoch studies. Models of plasma and neutral winds, as well as electron temperature plots, were then used to rule out several possible factors potentially responsible for an ion temperature enhancement. Finally, an epoch study of the ion-neutral relative drift was examined.

Chapter 4 discusses the possible geophysical factors behind the T_i spike observations. First, there is the context of the magnetic indices, particularly the correlation of the spike events with changes in the AE index while the radar was in the dusk sector. This finding was instrumental in linking the T_i spike events to a global enhancement in ionospheric convection. In turn, Chapter 4 shows that this implies that the spikes had to be related to the equatorward boundary of the convection pattern at dusk. We considered that Subauroral Ion Drifts (SAIDs) might have been the reason for the observed T_i enhancements. However, we found that a more likely cause was that ions and neutrals drift in opposite directions in the lower latitude portion of the measured convection pattern after an increase in the size of the convection cell.

The final chapter of this thesis summarizes the findings and proposes future research directions in relation to this work.

1.1 Ionospheric Composition

Before we discuss anything in the context of the ionosphere, we must first discuss what creates the ionosphere and what it is. This section examines briefly the origin of the ionosphere and its variations in time and space.

1.1.1 Radiation and Ionization

EUV radiation ionizes neutral particles, creating ions and free electrons (photoelectrons) above 100 km. In the upper atmosphere, photoionization is dominated by the following reactions [*Rees* (1989), Chapter 2]:

$$\mathrm{O} + h\nu \rightarrow \mathrm{O}^+ + \mathrm{e}^-$$

$$\mathrm{O}_2 + h\nu \rightarrow \mathrm{O}_2^+ + \mathrm{e}^-$$

$$\mathrm{N}_2 + h\nu \rightarrow \mathrm{N}_2^+ + \mathrm{e}^-$$

The production rates for these ions and electrons follow the "Chapman profile", seen in Figure 1.1. As radiation moves down towards the Earth's surface, the density of neutral gas increases. Neutrals become more abundant and production rates increase as long as there are enough photons available. However, an altitude is reached (as the altitude decreases) where there are enough neutrals to use up all of the available photons and the production rate drops off abruptly for decreasing altitudes beyond that point. This creates a nose-like altitude production profile. The production function of the Chapman profile can be described as [*Schunk and Nagy* (2000), Chapter 11]:

$$q(z^*) = q_{max} \exp\left(1 - z^* - \sec(\theta)\, e^{-z^*}\right) \tag{1.1}$$

where $q(z^*)$ is the production rate for a given reduced height, z^* is the reduced altitude given as:

$$z^* = \frac{z - z(\tau^* = 1)}{H}$$

q_{max} is the maximum peak production, θ is the solar zenith angle, z is the altitude, H is the scale height (the distance over which the density depletes by a factor of e, in this case, the density of the neutrals being ionized) and τ^* is the optical depth, τ, when $\theta = 0^\circ$ (where $\tau = \sigma n H \sec\theta$, while σ is the cross-section and n is the density of the species being ionized). The solar zenith angle affects this curve through changes in the amount of incident radiation in a region. As a result, as the day progresses, the production rate increases at first, then

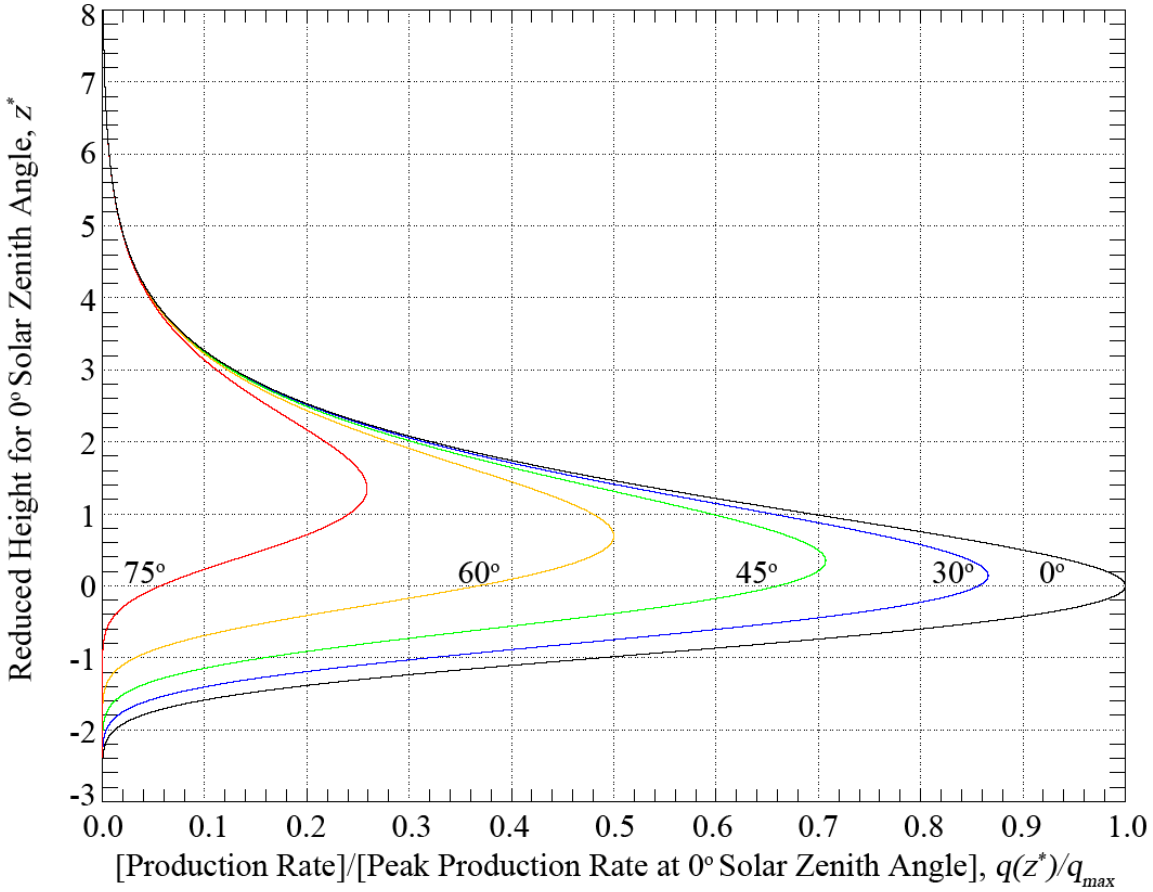

Figure 1.1: Chapman production curves for different solar zenith angles (curve labeled with respective angle).

decreases in sync with the solar zenith angle, thereby producing a strong diurnal variation in production rates in chemically controlled regions (typically, below 250 km altitude).

The photoionization reactions give way to interaction reactions:

$$O^+ + N_2 \rightarrow NO^+ + N$$

$$O^+ + N_2 \rightarrow N_2^+ + O$$

$$O^+ + O_2 \rightarrow O_2^+ + O$$

$$N_2^+ + O \rightarrow NO^+ + N$$

as well as the following recombination reactions:

$$N_2^+ + e^- \rightarrow N + N$$

$$NO^+ + e^- \rightarrow N + O$$

$$O_2^+ + e^- \rightarrow O + O$$

High altitude chemistry creates an electron density profile that peaks at a higher altitude than the production rate (Figure 1.4). Between roughly 150 km and about 250 km, the electron density profile comes from balancing the production rate with the recombination rate. In this region, the density increases steadily with altitude, even though the production rate decreases with altitude. This is because the recombination rate decreases even more rapidly with altitude. However, above 250 km transport processes are more rapid than chemistry. It is at this point that the density, which had been increasing with altitude, starts to decrease through diffusion.

At high latitudes additional complications are introduced by energetic particles (precipitation). These particles can also ionize and produce secondary ion-electron pairs in the ionosphere. Figure 1.2 gives the ionization rates for primary electrons precipitating along magnetic field lines. Figure 1.3 gives the altitude profiles of the ionization rates produced by primary protons as a function of their energy at the top of the atmosphere. In both of these plots, the ionization rate increases with decreasing altitude until a density limit is reached.

1.1.2 Regions of the Ionosphere

The ionosphere lies below the region formed by the interaction of solar wind and the magnetic field of a planet, known as the magnetosphere (seen in Figure 1.13) [*Harra and Mason* (2004), Chapter 4]. The ionosphere is the region of the atmosphere with a high density (greater than 10^3 cm^{-3}) of weakly ionized gas, mostly produced by solar Extreme Ultra-Violet (EUV) radiation ionizing neutral particles in the upper atmosphere through the production process described by equation 1.1 [*Schunk and Nagy* (2000), Chapter 9]. Figure 1.4 features a profile plot of plasma density in the upper atmosphere of the Earth, to further define this region. As shown in Figure 1.4, the Earth's ionosphere can be broken into three sub-regions: the D, E and F-regions. The chemistry of the D-region, between 60 km and 90 km, includes a region defined by dissociative recombination, ion recombination, ion-ion neutralization, three-body reactions, photo detachment and associative detachment [*Schunk and Nagy* (2000), Chapter

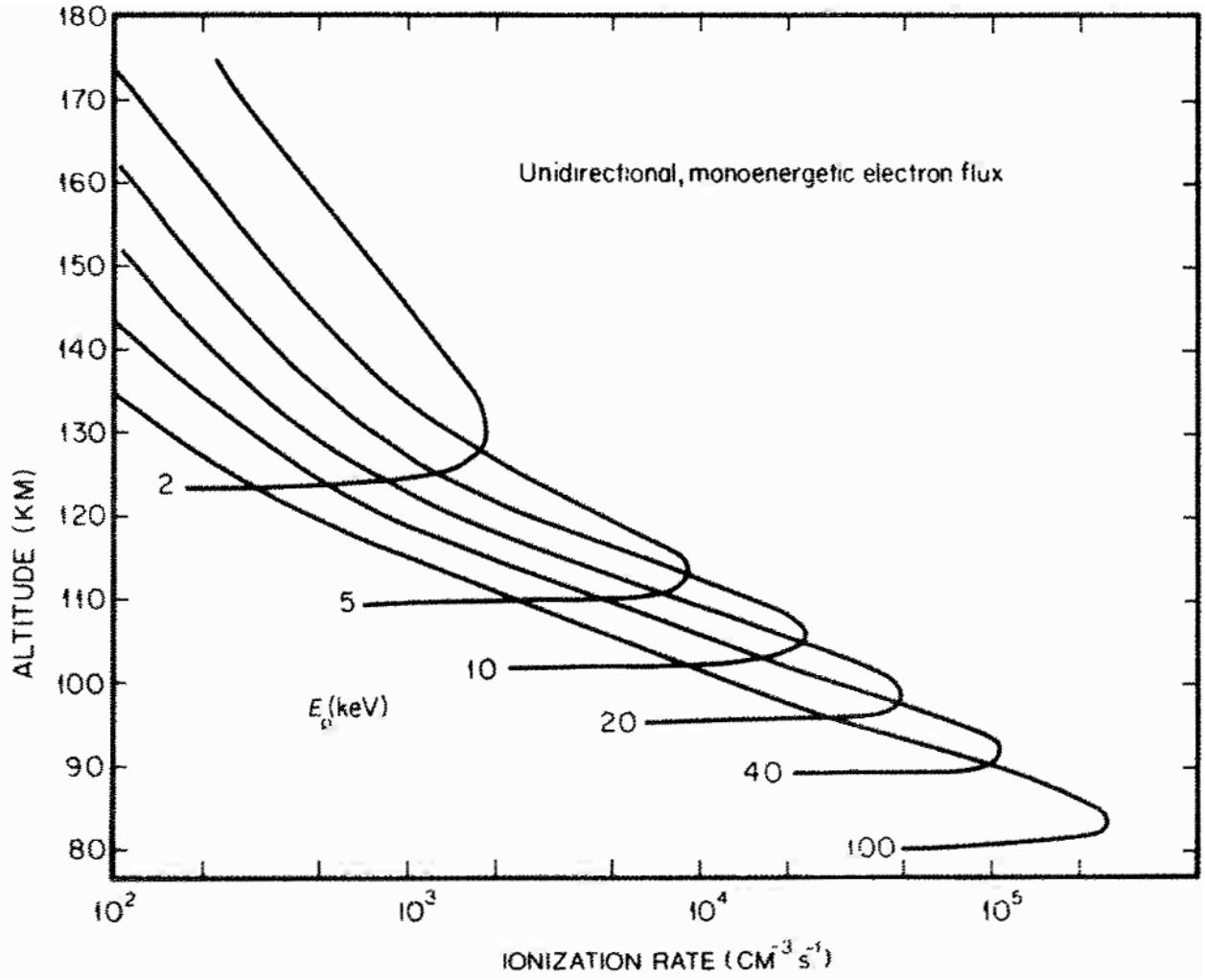

Figure 1.2: Profile plot of ionization rates produced by a flux of 10^8 electrons cm^2 s^{-1} precipitating along the magnetic field lines into the Earth's atmosphere. A variety of different initial rates E_p (keV) are shown [*Rees* (1989), Chapter 3].

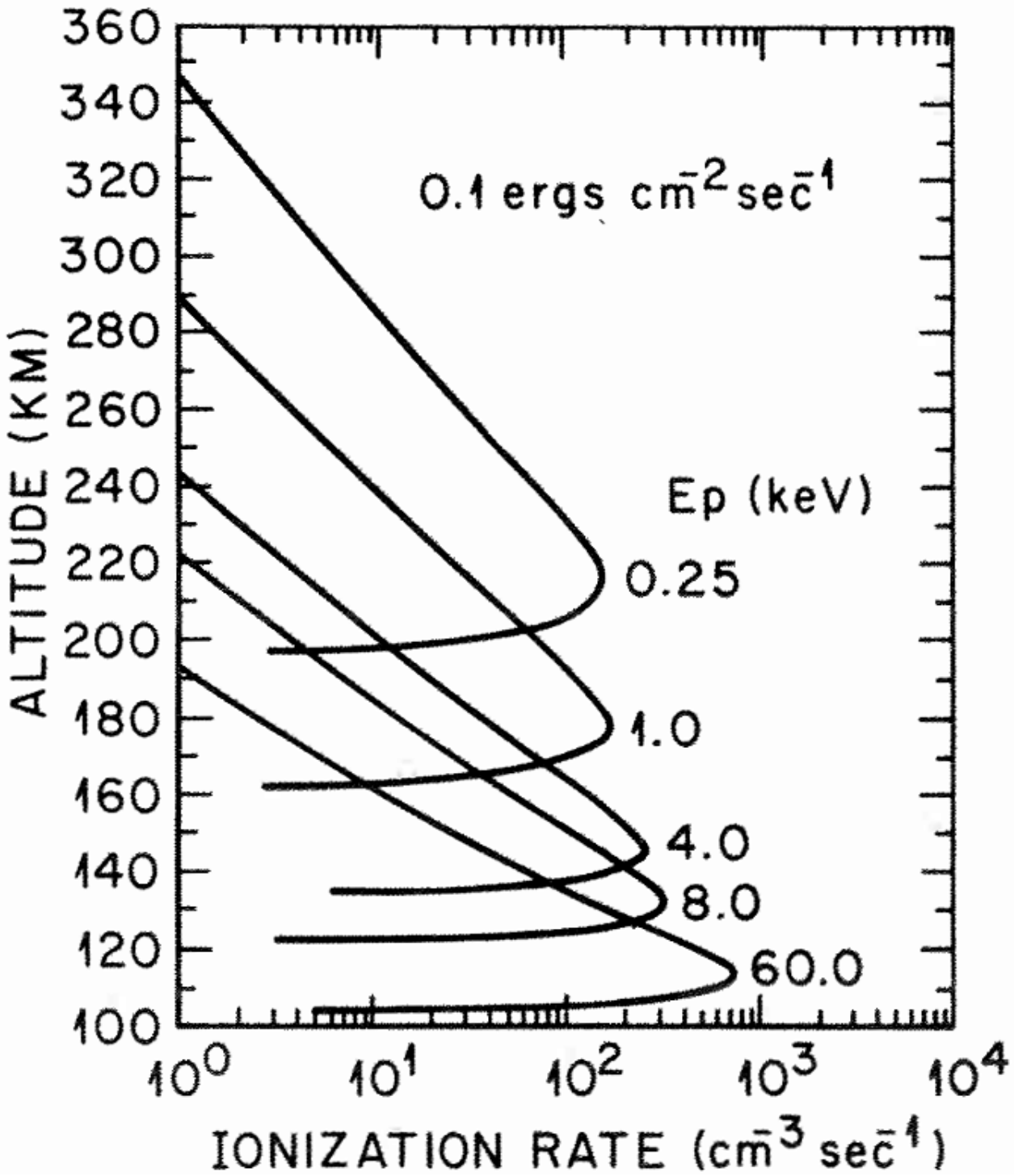

Figure 1.3: Profile plot of ionization rates produced by precipitating primary proton fluxes with energy E_p at the top of the atmosphere. Assumes isotropic flux and an energy flux of 0.1 erg cm^{-2} s^{-1} [*Rees* (1989), Chapter 3].

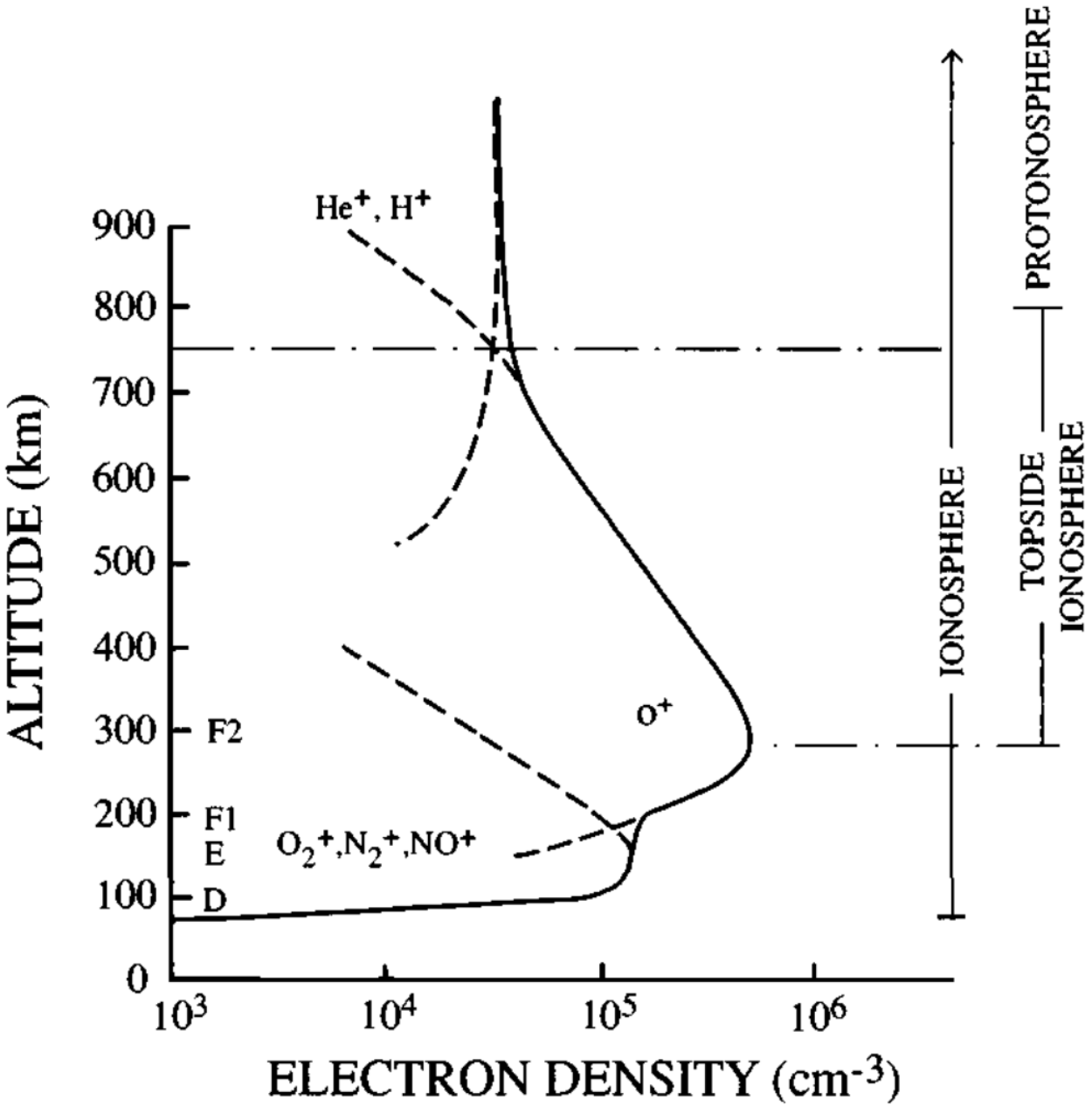

Figure 1.4: A plot of electron density as a function of height. In this plot, the ionosphere and its regions are indicated [*Schunk and Nagy* (2000), Chapter 2].

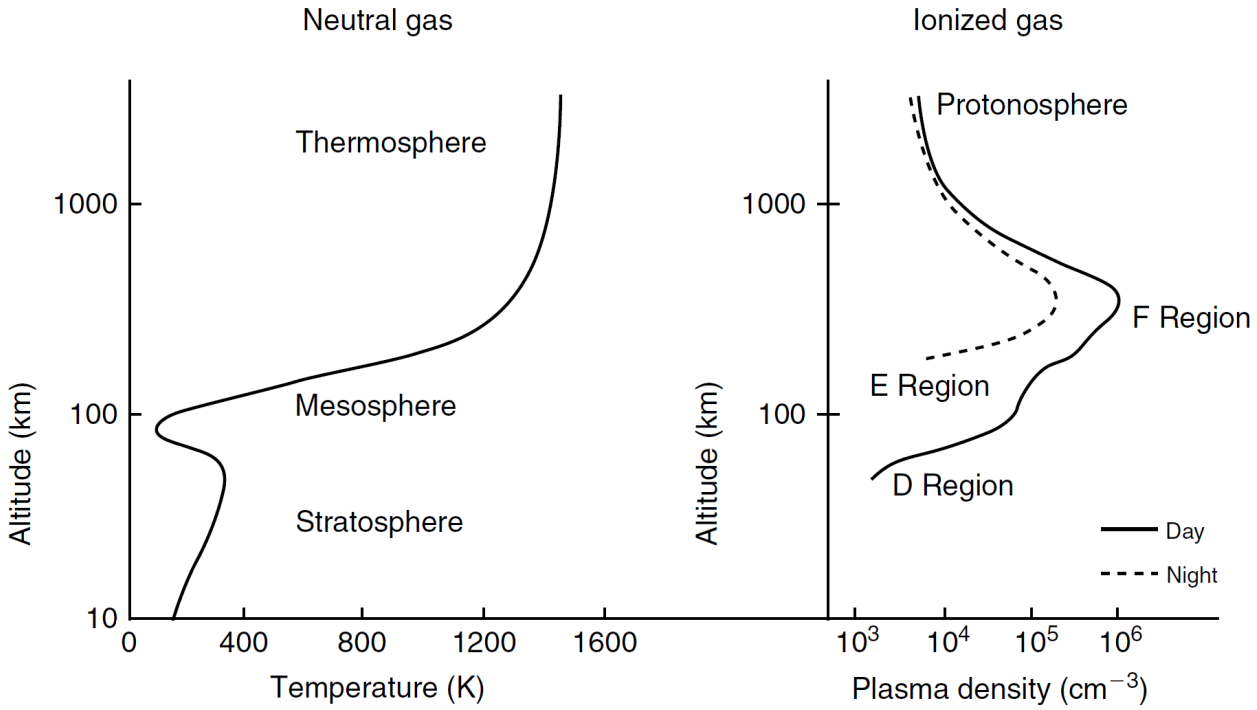

Figure 1.5: A plot of neutral temperature as a function of height. In this plot, the ionosphere and its regions are indicated alongside [*Kelley* (2009), Chapter 1].

11]. The main sources of ions in this region are Lyman alpha absorption and photoionization of O_2 and NO. The *E*-region, between 90 and 150 km, is defined by ionization from soft X-rays (1-10 nm) and Ultra-Violet (UV) ionization of O_2 and N_2. Lastly, the highest layer is the *F*-region, which exists from 150 km to the edge of the ionosphere (roughly 1000 km). For this region, EUV radiation ionizes O, creating O^+. Figure 1.5 indicates the depletion of plasma at night as well as the neutral temperatures of the ionosphere. Around 90 km, radiative cooling reduces the neutral temperature, while higher altitudes have a low density of radiators. Heat is carried down from higher altitudes to the radiative region through heat conduction.

1.2 Large Scale Picture of Electric Fields

Electric fields in the ionosphere are generated through several sources. For this research, there are two worth discussing: electric fields from the ionospheric dynamo and electric fields produced by magnetospheric processes. Electric fields within the ionosphere occur

mainly from an ionospheric dynamo. This happens when ionospheric winds, created by uneven heating and/or tidal forces, move charges across the magnetic field at different rates, depending on their mass and charge (*Pudovkin*, 1974). This wind dynamo is capable of generating electric fields of the order of 1 mV/m at middle latitudes and 5 to 10 mV/m in the equatorial region (*Park*, 1976).

One magnetospheric electric field generator results from the interaction of the Earth's magnetic field and the magnetic field of the solar wind. As the solar wind approaches the Earth, the magnetic field of the wind merges with the geomagnetic field of the Earth (dayside merging), opening flux tubes. These open "lobe" magnetic field lines then move to the nightside, carrying plasma with them. At some point in the nightside the antiparallel lobe field lines from north and south of the magnetic equator reconnect, closing the flux tubes (nightside merging). These newly closed stretched geomagnetic field lines then move earthward with the plasma and the process repeats itself (briefly outlined for a solar magnetic field that is purely in the -z direction in Figure 1.6). The merging magnetic fields create a generator, which drives a perpendicular electric field in the ionosphere (*Kelley*, 2009). This electric field, in turn, creates a plasma drift in the ionosphere. In the magnetosphere, the particles also have curvature drift (drift caused by field line curvature) and gradient drift (drift from a charge moving into a stronger or weaker magnetic field). These drifts are charge-dependent, so separation of positive ions and electrons can occur, resulting in non-inductive voltages that cause current flow and field aligned currents that map into the ionosphere. Both the curvature and gradient drift decrease rapidly with latitude, so they are very important near the magnetosphere at the equator, but are not seen in the high latitude ionosphere.

Two regions can be defined in the context of moving magnetic field lines and merging: the polar region, consisting of open (lobe) flux tubes (solar wind and geomagnetic field lines), and the auroral region, containing closed flux tubes (just geomagnetic field lines) [*Harra and Mason* (2004), Chapter 9]. If the magnetic field of the solar wind is purely southward, magnetic field lines are dragged towards the nightside of the Earth by the solar wind, causing plasma in the polar region to be pulled antisunward by a dawn-to-dusk electric field (*Heelis*, 1984). Eventually, the magnetic field lobe lines will experience nightside merging, and the resulting closed stretched flux tubes reach down to the Earth, defining the auroral region.

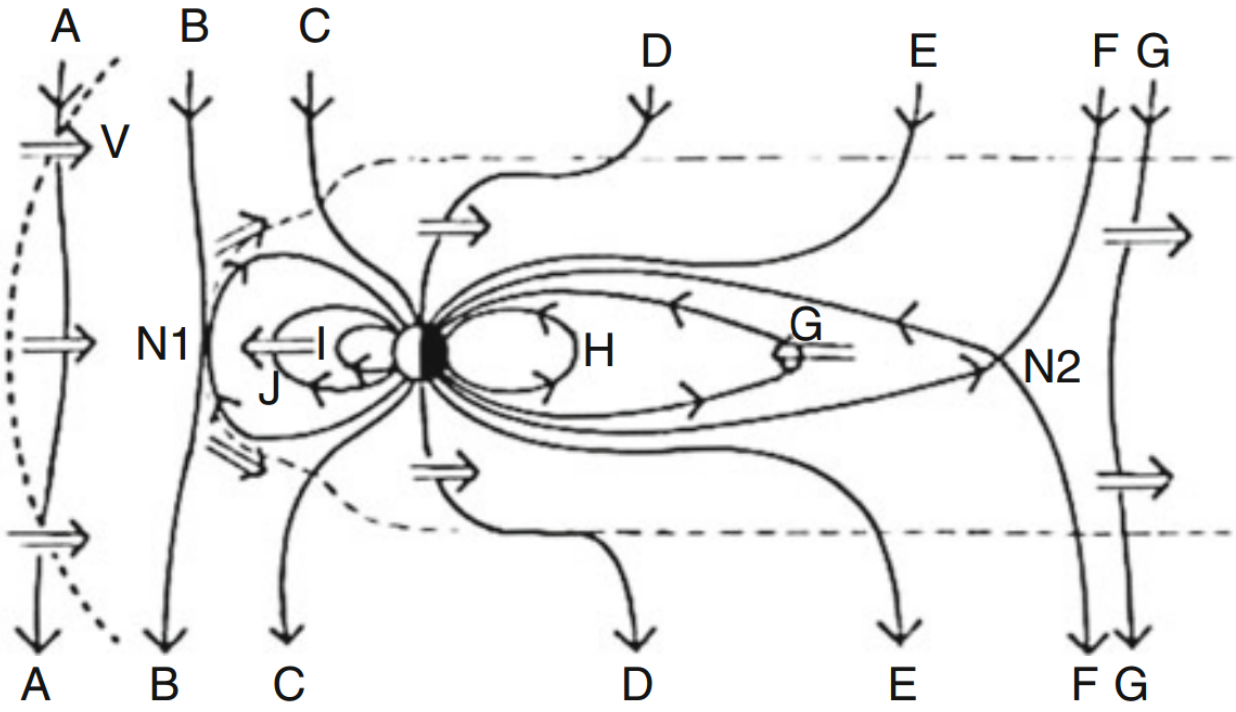

Figure 1.6: Cartoon of magnetospheric convection. Letters indicate the order of events, N1 and N2 indicate the location of the merging events [*Zarka* (2011), Chapter 13].

The magnetic field lines then convect the plasma and closed flux tubes of the auroral region along the dawn and dusk side of the Earth, back to the dayside through a dusk-to-dawn electric field (*Reiff*, 1982). When these flux tubes are back on the dayside, merging in the magnetic field lines occurs and flux tubes open again, pushing plasma back towards the nightside and into higher latitudes, into the polar region. This process creates two large convection cells in the ionosphere, a dawn and a dusk convection cell. At lower latitudes lies the co-rotation region, where, as seen from above the north pole, closed flux tubes and plasma move counter-clockwise with the Earth's rotation [*Harra and Mason* (2004), Chapter 9]. These three regions are labeled in Figure 1.7 while a more precise illustration of the ionospheric convection cycle is shown in Figure 1.8[1].

These convection processes, however, are ideal and occur only when the Interplanetary Magnetic Field (IMF) of the solar wind is purely southward. It is not uncommon for the IMF to have an east-west component (B_y), incurring a merging process that drives a field working off-centre. In this case, while there is still a two-cell convection pattern, these cells become anti-symmetric (*Reiff and Burch*, 1985). With a positive B_y component, the dayside merging occurs more on the dusk side of the northern hemisphere. So, instead of seeing two even convection cells there exists something more like a circular cell and a banana shaped cell, where, generally, the B_y component will point from the circle to the banana. This, as well as the effect of a negative B_y component, can be seen in Figure 1.9. Beyond affecting the shape of the convection cells, the IMF direction will alter the speed of the flows present in plasma convection. The speed of antisunward flows in the noon and midnight sectors are influenced by the north-south component of the IMF (*Gillies et al.*, 2011). This is because a larger southward IMF will elicit more dayside merging.

The orientation and strength of the IMF also influences substorm occurrences (*Gillies et al.*, 2012). Substorms are frequent, sudden (on the order of hours) ejections of energy from the magnetosphere into the ionosphere [*Harra and Mason* (2004), Chapter 4]. There are three phases to a substorm; the growth phase, the expansion phase and the recovery phase. These steps are outlined in Figure 1.10. The growth phase is the initial stage in which a large amount of kinetic energy from the solar wind (roughly 10^6 J) is stored in the magnetosphere

[1] A more precise/completed version is presented in the CTIPe model, Figure 3.12

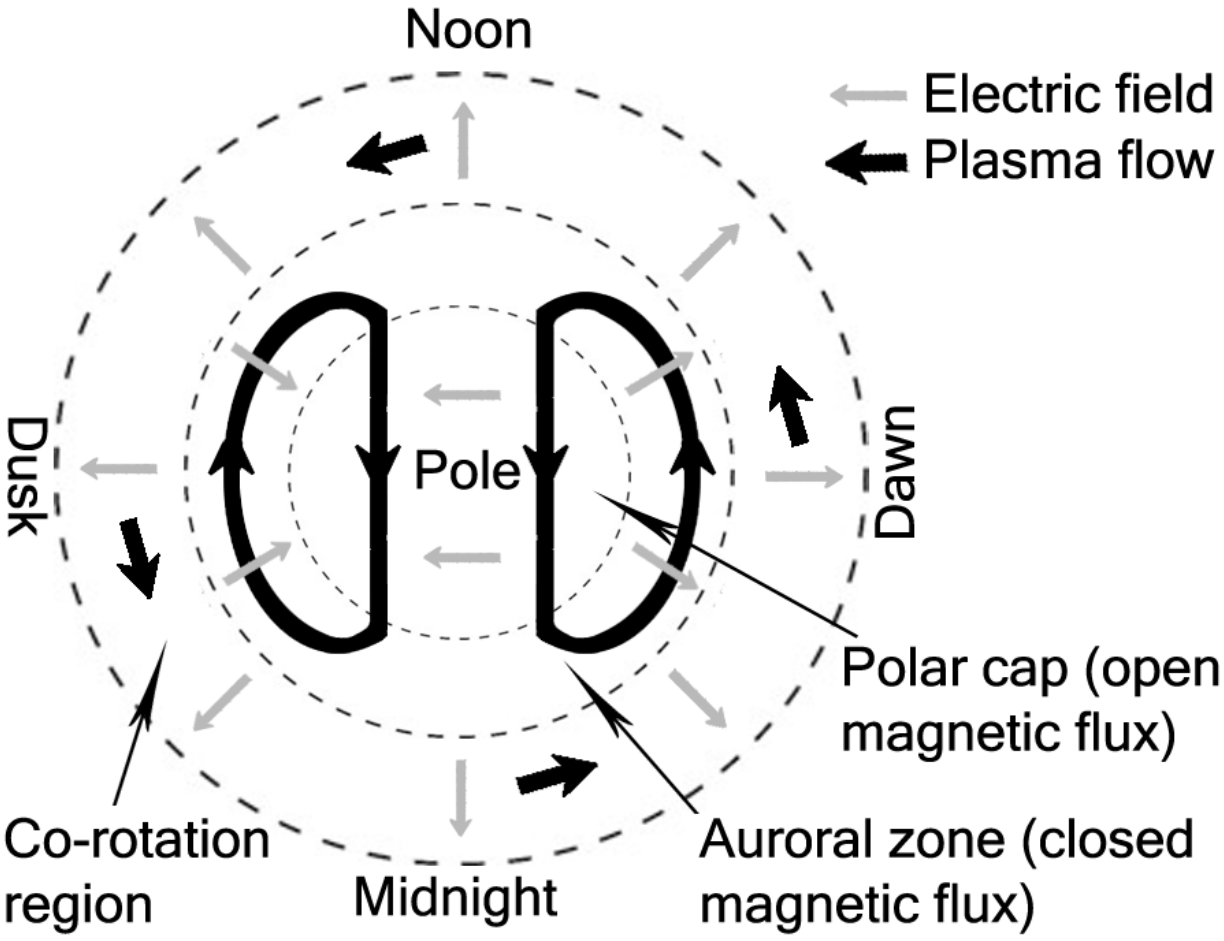

Figure 1.7: Cartoon of the convection cycle and regions seen in the Earth's northern ionosphere [*Harra and Mason* (2004), Chapter 4].

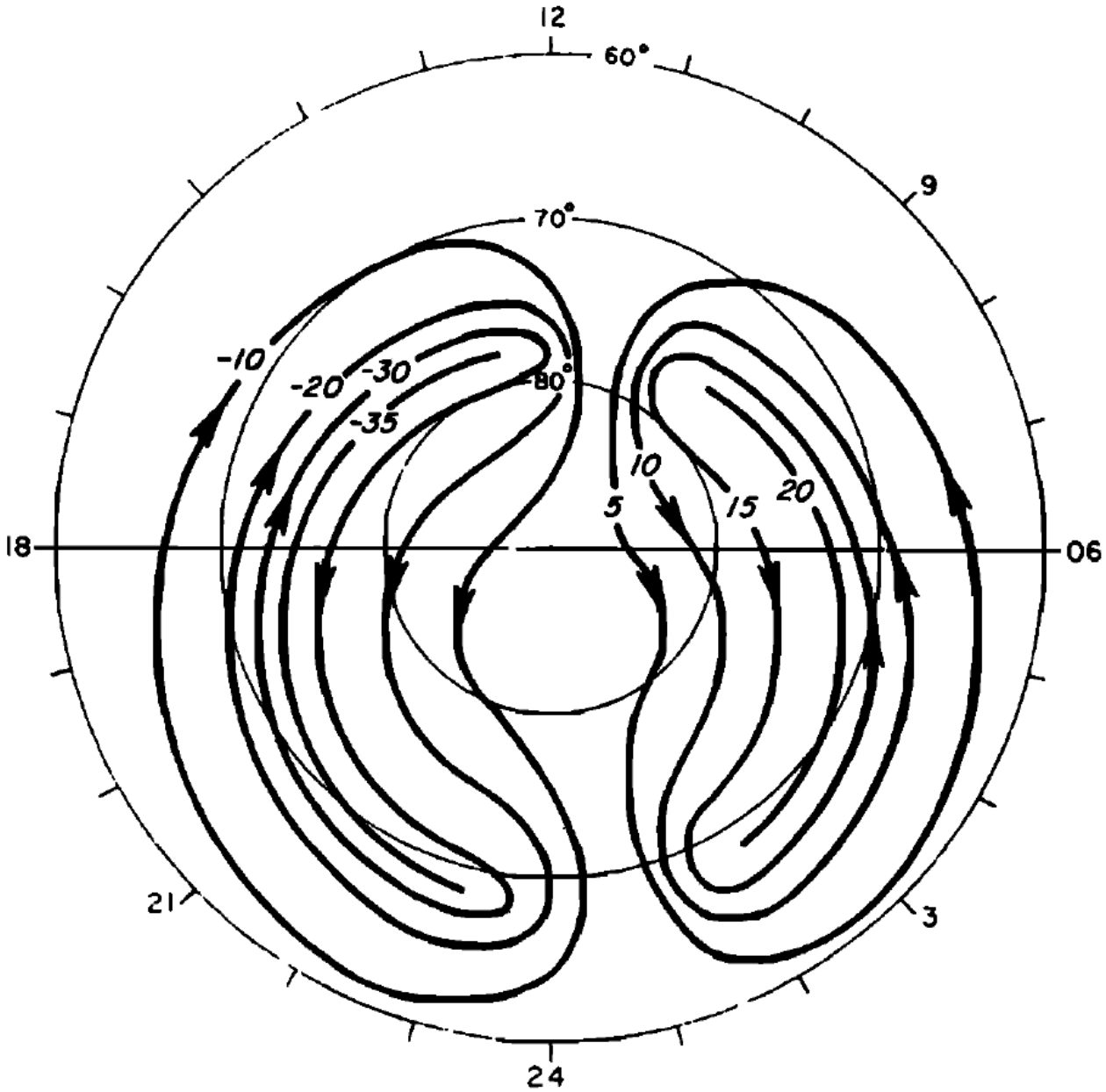

Figure 1.8: A more precise illustration of the convection cycle as seen looking down on the Earth's northern ionosphere. Values represent electric potential, arrows give convection direction (*Heelis et al.*, 1982).

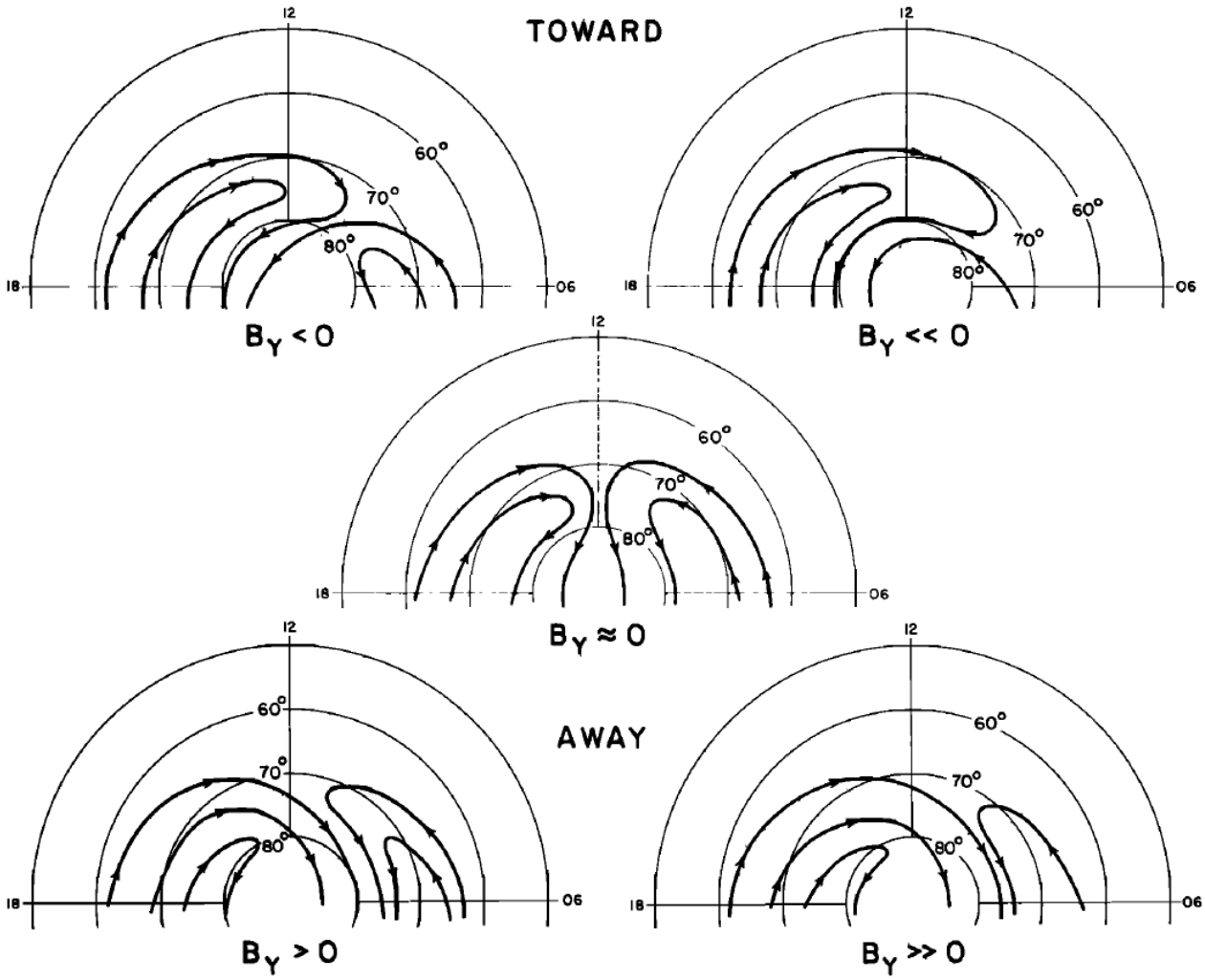

Figure 1.9: A schematic representation of the flow geometries observed in the dayside northern hemisphere for different magnitudes of B_y when B_z is negative and $|B_x|$ is constant (*Heelis*, 1984).

as magnetic energy (Figure 1.10, panel 1). This is believed to come from an increase in the dayside merging rate brought on by a southward turning of the IMF either increasing merging at the quasi-neutral line or increasing Flux Transfer Events (FTE) (*Arnoldy*, 1971; *Foster et al.*, 1971). Because this IMF is not immediately felt on the nightside, merging will be relatively slower at the neutral line in the distant tail, allowing for open lobe flux tubes to be added to the magnetosphere (*McPherron*, 1970). These extra flux tubes will thereby increase the magnetotail diameter and the field strength, as well as flare the outward surface of the magnetopause. In response to the increased field strength, the plasmasheet will thin and the cross-tail currents will increase. By the end of this process there will be a third "neutral line" (a equatorial region where the magnetic field lines oppose each other), besides the one on the dayside of the magnetosphere (referred to as the Dayside Neutral Line) and the one located in the tail (Distant Tail Neutral Line, DTNL). Between the end of the tail and the Earth, the Near Earth Neutral Line (NENL) is formed, which is the first step of the expansion phase [*McPherron* (1995), Chapter 13; *Nishida and Nagayama* (1973)].

The expansion phase is the response of the magnetosphere to this increased energy (Figure 1.10, roughly panel 2 and 3). In this stage of the substorm, the excess of energy collected during the growth phase is quickly expelled and a jet of plasma flows back towards the Earth (*McPherron*, 1979). Though there is much uncertainty in the mechanics of this phase, one of the current theories suggests that the space between the NENL and the DTNL holds a loop of reconnected field lines that have trapped hot plasma contracted from the accelerated plasmasheet. This bubble of plasma between the Earth and the end of the tail is known as a plasmoid (*Hones et al.*, 1984). The pressure associated with the magnetosphere near the Earth, as well as the force in the magnetic field lines, causes the plasmoid to move farther from the Earth and, eventually, off into the downstream solar wind. As well, by the end of this phase, the NENL has disappeared.

The final stage, the recovery phase, is the magnetosphere returning to normal after the loss of plasma from a plasmoid onset event (Figure 1.10, roughly panel 4 and 5). Once the plasmoid has been released, there will be a reduced field strength in the tail (less magnetic energy) as well as a movement of closed flux tubes towards the dayside and open flux tubes downstream of the Earth (*Forbes et al.*, 1981). By the end of this phase the magnetosphere

is back to its original, quiet time configuration [*Harra and Mason* (2004), Chapter 5].

A change in B_z may elicit a geomagnetic storm. Geomagnetic storms differ from substorms in that geomagnetic storms last longer, occur less frequently than substorms and inject charges into the Van Allen belts [*Harra and Mason* (2004), Chapter 5]. They cause large depletions in geomagnetic indices (the SYM-H index during a storm is seen in Figure 1.11), as well as increase the size of the auroral oval (Figure 1.12).

Substorms are one example of how the IMF orientation and strength are important for different ionospheric processes. However, changes in the solar wind currents will also change ionospheric processes by affecting the magnetic field (*Gillies et al.*, 2012). When the solar wind meets the geomagnetic field of the Earth, the solar wind is shielded from the magnetic field of the Earth through boundary currents that increase and double the magnetic field of the Earth downwind, while reducing the magnetic field to zero upwind. Increases in the solar wind currents will compress the dayside magnetosphere until it is matched by those of the Earth. These increases in the geomagnetic field strength and the magnetopause current lead to a northward deflection of the magnetic field at the Earths surface (*Shue et al.*, 1997). This then raises the ionospheric plasma drift speed in the noon sector, the dayside convection velocities, and the average drift speed in the midnight sector (*Boudouridis*, 2007; *Gillies et al.*, 2012). These current changes are usually caused by solar ejections and regions where shocks are created by fast solar wind plasma overtaking slower solar wind plasma (*Borovsky and Denton*, 2006; *Zhang et al.*, 2007).

Given that we will be examining data from near the convection boundary, it would be important to discuss in detail a common effect of electric fields in the evening subauroral region. Occurrences of layers of intense westward drift in the subauroral region of the ionosphere are referred to as Sub-Auroral Polarization Streams (SAPS). SAPS is a term that includes phenomena like penetration electric fields (penetrating fields seen during disturbed geophysical conditions), polarization jets (a subauroral supersonic narrow stream of plasma seen during substorms) and Sub-Auroral Ion Drifts (SAIDs) (*Foster and Burke*, 2002; *Foster and Vo*, 2002; *Galperin et al.*, 1974; *Yeh et al.*, 1991).

Past observations describe SAIDs as large westward ion flows (larger than 1 km/s, with a maximum flow velocity of 1.4 km/s near the mid-latitude ionization trough and exceeding 500

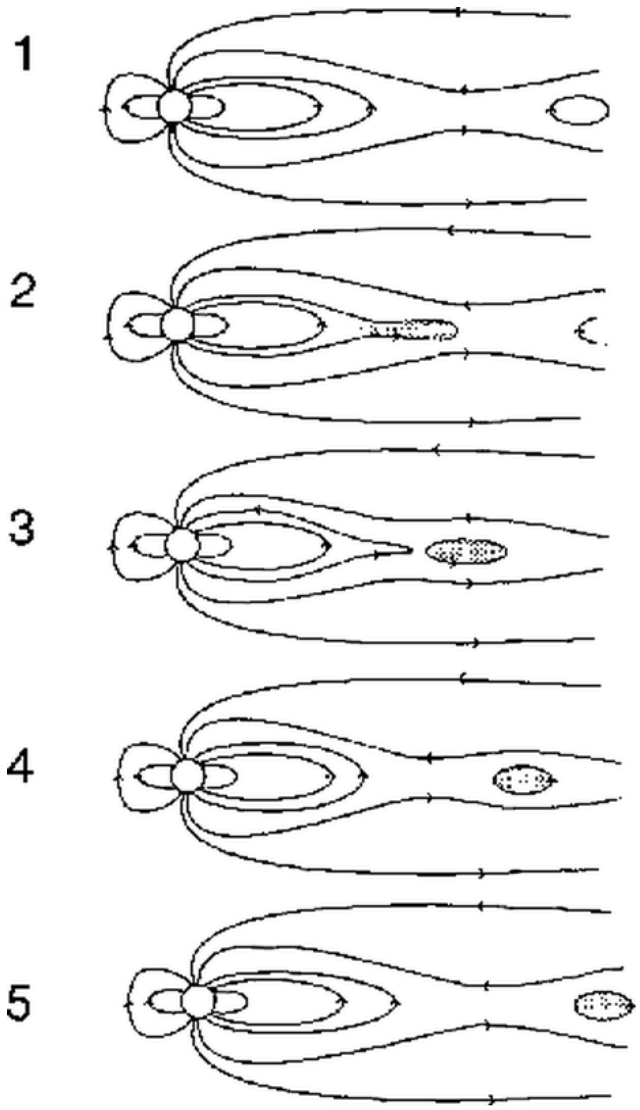

Figure 1.10: A substorm visualization in terms of the field lines in the magnetosphere. The numbers indicate the order of events (*Hones et al.*, 1984).

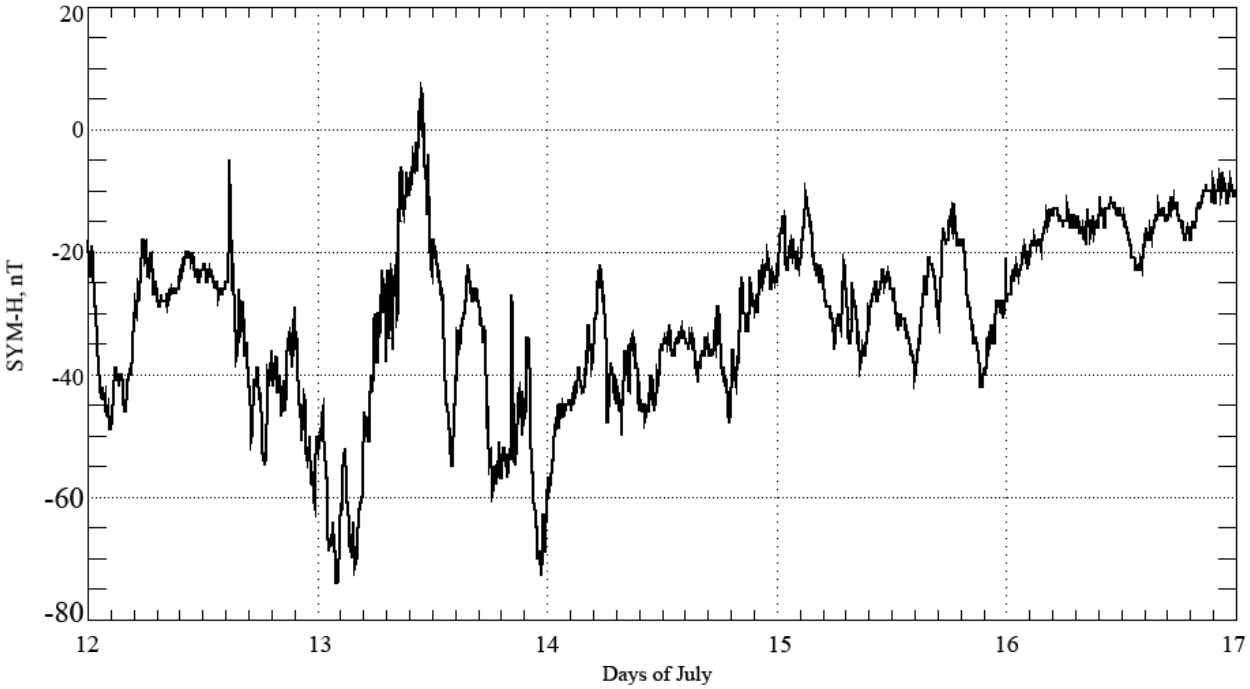

Figure 1.11: SYM-H during the great magnetic storm of 12-16/July/1982.

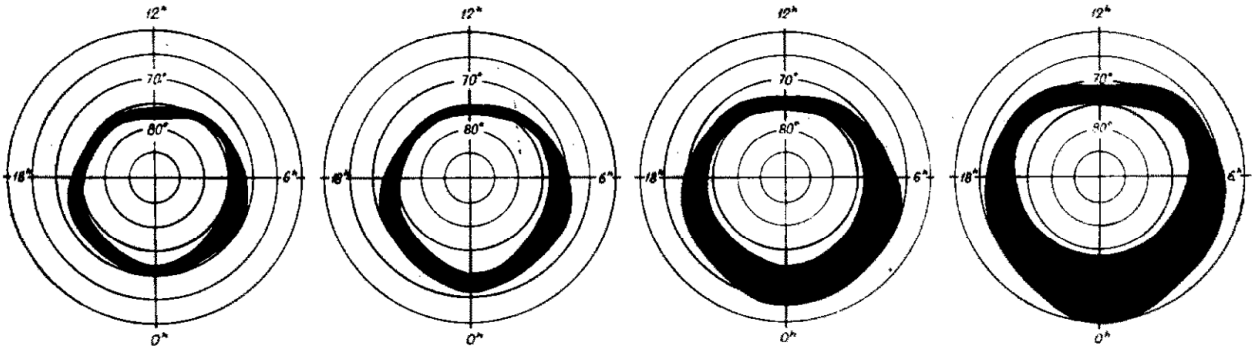

Figure 1.12: Different auroral ovals with varying degrees of geomagnetic activity on a geomagnetic coordinate system (increasing activity from left to right) (*Feldstein and Starkov*, 1967).

m/s equatorward of the high latitude convection pattern) observed in the evening just equatorward of the auroral boundary (roughly 60-65° latitude) during strong poleward-directed electric fields (*Anderson et al.*, 1993; *Karlsson et al.*, 1998; *Spiro et al.*, 1979). These flows are latitudinally narrow, existing for roughly 30 minutes to 3 hours and only extending 1-2° of latitude (*Anderson et al.*, 2001). Though SAIDs can occur without substorms, they are often observed during the substorm recovery phase (*Anderson et al.*, 1993, 2001; *Karlsson et al.*, 1998). They generally occur in the winter near the mid-latitude trough (*Wang and Lühr*, 2011; *Wang et al.*, 2008)

Roughly 85% of SAIDs are accompanied by an evening F-region mid-latitude ionization trough, which can be seen as a large, quick depletion in n_e (*Anderson et al.*, 2001). Since SAPS are faster in the winter (local) than in the summer, SAPS are thought to be inversely proportional to ionospheric conductivity brought on by radiation exposure (*Anderson et al.*, 2001). This is because a smaller conductivity will require increases in the polarization electric field (velocity) in order to maintain a continuous current in the subauroral region.

There are several theories as to why SAIDs occur. One theory proposes that strong downward field aligned currents close with upward field aligned currents through poleward horizontal Pedersen currents during substorms. Then the low ionospheric conductivity in the nightside sub-auroral region creates a poleward electric field, leading to fast westward ion drifts and depletions in the ionospheric density (*Anderson et al.*, 1993; *Karlsson et al.*, 1998). A different theory suggests a magnetospheric voltage generator is created by a moving plasma front, where the SAID is the result of an interface between a cold plasma trough and the hot injected particles (*De Keyser*, 1999, 2000; *De Keyser et al.*, 1998; *Lemaire et al.*, 1998). The shear and thermoelectric effects between the injected plasma and plasma trough would then cause the generation of intense electric fields in the evening sector.

1.3 Mapping Magnetospheric Regions to the Ionosphere

Figure 1.13 shows a three-dimensional cut of the plasma surrounding the Earth which includes the plasmasphere, the radiation belts (also called the Van Allen belts), and the ring current. The ring current flows westward around the Earth and is centered at the equa-

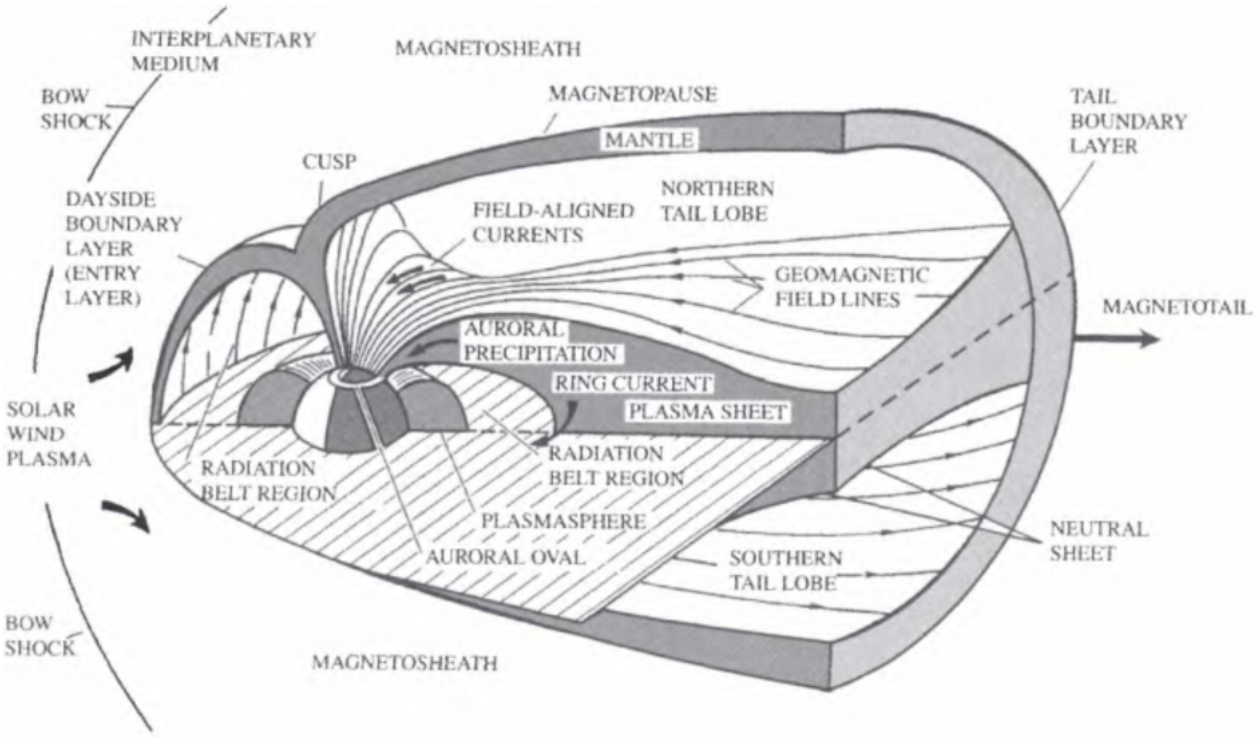

Figure 1.13: The anatomy of the Earth's magnetosphere [*Schunk and Nagy* (2000), Chapter 2].

tor, in the plasmasheet. It is formed by the drift of trapped charged particles (*Frank et al.*, 1964). The plasmasheet is the area of the magnetotail where the closed magnetic field lines and the particles on them are subject to the control of the solar wind and the IMF it carries. The nightside tail of the plasmasheet becomes stretched due to nightside merging at the DTNL, particularly when there is a southward IMF. During a substorm event, the tail becomes unstable and charged particles flow from the tail towards the Earth, leading to auroral precipitation. At the same time, auroral particles are injected into the ring current as the result of the near Earth merging during the growth phase of a substorm.

Overlapping the inner part of the ring current, one sees the Van Allen belts, two regions composed of trapped high energy particles. The inner belt is chiefly composed of protons, while the outer belt is almost completely composed of energetic electrons (*Frank et al.*, 1964). At ionospheric heights the radiation belts map to a narrow region between the plasmasphere and the ring current. A key feature that sets the Van Allen belt particles apart from the auroral particles are their energies. Auroral particles are typically 10 keV or less, while Van

Allen particles have energies in excess of 1 MeV. This means that if they precipitate, the Van Allen particles ionize the atmosphere at a much lower altitude than the auroral particles. It is also interesting to note that the ring current and the Van Allen radiation belts serve to block high latitude dynamo electric fields at mid- to low-latitudes [*Schunk and Nagy* (2000), Chapter 2].

The plasmasphere is the region where the plasma corotates with the Earth. It extends to upper mid-latitudes (typically near 60°) and, of course, it is in a region of dipole geomagnetic field lines (as seen in Figure 1.14) [*Schunk and Nagy* (2000), Chapter 11]. Within this region is a significant amount of plasma (roughly 10^3 cm^3) made of cold H^+ ions trapped by magnetic field lines [*Kelley* (2009), Chapter 5; *Lemaire and Gringauz* (2005), Chapter 4]. The boundary between the plasmasphere and the plasmasheet is named the plasmapause. The plasmapause is the boundary between the plasmasheet convection region and the corotation region, where the plasma and magnetic field rotate with the Earth. Above the ionosphere, this boundary can be seen in electron density data as a minimum in plasma density. Specifically, as latitude increases, there is a steady decrease in plasma density until the plasmapause is reached. The region of depleted densities poleward of the plasmapause is called the plasmatrough in the ionosphere, or the transition region (transition plasmasheet) in the magnetosphere.

Though it is clear that ions of lower mass densities would appear at higher altitudes, the dominant H^+ composition of the plasmasphere is not quite that straight-forward. At lower altitudes (600 to 1500 at mid-latitudes), where H^+ ions are a minor ion, H^+ ions are actually in chemical equilibrium with O^+ ions (the dominant ion) through an accidental resonant charge exchange reaction [*Schunk and Nagy* (2000), Chapter 11]:

$$O^+ + H \longleftrightarrow H^+ + O$$

At higher altitudes, chemical equilibrium turns into diffusive equilibrium, allowing the H^+ density to continue increasing with height as the protons move upward in response to the polarization electric field created by the O^+ ions and electrons. Eventually, an altitude is achieved in which the H^+ density is greater than the O^+ density, and the H^+ population decreases exponentially with increasing altitude. As latitude increases, a pressure decrease

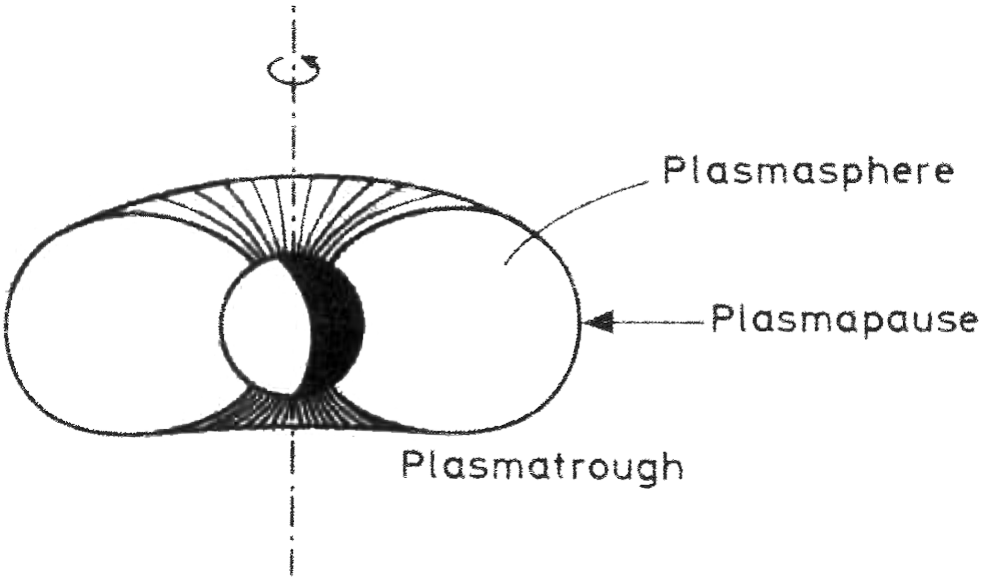

Figure 1.14: Cartoon of the Earth's plasmasphere [*Lemaire and Gringauz* (2005), Chapter 4].

comes from the volume increase of the plasmaspheric flux tubes, lowering the H^+ density and pressure [*Kelley* (2009), Chapter 5]. These lower latitude processes help to define the composition and shape (torus) of the plasmasphere, seen in Figure 1.14.

The size of the plasmasphere and the location of the plasmapause change with geomagnetic activity. During quiet periods, the plasmasphere is filled by the ionosphere. At the same time the size of the plasmasphere increases and the latitude of the plasmapause boundary mapped to the ionosphere increases (*Goldstein et al.*, 2003). As geomagnetic activity increases, the plasmasphere shrinks and the latitude of the plasmapause decreases (*Chappell*, 1970). This shrinking comes from erosion caused by dayside merging creating an enhancement in sunward convection in the inner magnetosphere, thereby making the whole high latitude convection pattern larger. (*Grebowsky*, 1970).

Though many things are understood about these regions of the magnetosphere, the processes occurring within the radiation belts are not well understood and there are many questions that need to be answered about their origin and their perturbations during magnetic storms. For this reason, the National Aeronautics and Space Administration (NASA) deployed satellites within the Van Allen belts, called the Van Allen Probes. The general goals of these probes are (*Zell*, 2013):

- "Discover which processes – singly or in combination – accelerate and transport the particles in the radiation belt, and under what conditions."
- "Understand and quantify the loss of electrons from the radiation belts."
- "Determine the balance between the processes that cause electron acceleration and those that cause losses."
- "Understand how the radiation belts change in the context of geomagnetic storms."

Of interest for the present thesis is the fact that the radiation belts are only disturbed in the presence of magnetic storms.

1.4 Overview of Momentum and Energy Balance

For this work it is not enough to understand the composition of the ionosphere and electric fields. In order to have a clearer understanding of the ionosphere it proves beneficial to discuss the momentum and energy balance in relation to charges, specifically in the F-region ionosphere (given that this work is focused there).

1.4.1 Momentum Balance and Plasma Motion

When an electric field is imposed in a region with charges, those charges experience a force either in the direction of the electric field (positive charges), or against the electric field (negative charges, like electrons). Electric fields can be produced by charge separation and time-varying magnetic fields. To make describing their effects easier to explain, electric fields will be broken into two categories: electric fields perpendicular to the geomagnetic field and electric fields parallel to the geomagnetic field. For both of these, a steady state equation of motion is reached in each species after a few collision times, $1/\nu_{\alpha n}$. The resulting equation is given by [*Schunk and Nagy* (2000), Chapter 5]:

$$0 = \frac{q_\alpha}{|q_\alpha|}\Omega_\alpha \left(\frac{\mathbf{E}'}{B} + (\mathbf{V}_\alpha - \mathbf{V}_n) \times \hat{b} \right) - \nu_{\alpha n} (\mathbf{V}_\alpha - \mathbf{V}_n) - \frac{\nabla P_\alpha}{\rho_\alpha} + \mathbf{g} \tag{1.2}$$

In this equation $\nu_{\alpha n}$ is the momentum transfer collision frequency between charges and neutrals, $\mathbf{V}_n$ is the mean velocity of the neutral gas, $\mathbf{V}_\alpha$ is the mean velocity of charges, $\mathbf{B}$ is the geomagnetic field strength, ∇P_α is the pressure gradient of the species α, q_α is the charge, $\mathbf{E}'$ is the electric field in the frame of the neutrals ($\mathbf{E}' = \mathbf{E} + \mathbf{V}_n \times \mathbf{B}$, where $\mathbf{E}$ is the electric field), Ω_α is the cyclotron frequency of the species (defined as being positive), ρ_α is the mass density, and $\hat{b}$ is the direction of the magnetic field line. We derive next an equation of motion for a charge when an electric field is perpendicular to a magnetic field, and an equation for when an electric field is parallel to a magnetic field.

Motion Perpendicular to the Geomagnetic Field

Since there is a perpendicular field component, taking the cross product of equation 1.2 against the direction of the magnetic field, $\hat{b}$, will leave us with terms that are perpendicular to the magnetic field.

$$0 = \frac{q_\alpha}{|q_\alpha|}\Omega_\alpha \left(\frac{\mathbf{E}'}{B} + (\mathbf{V}_\alpha - \mathbf{V}_n) \times \hat{b} \right) \times \hat{b} - \nu_{\alpha n} (\mathbf{V}_\alpha - \mathbf{V}_n) \times \hat{b} - \frac{\nabla P_\alpha}{\rho_\alpha} \times \hat{b} + \mathbf{g} \times \hat{b} \qquad (1.3)$$

It is easy to show from a simple scaling analysis that if E'/B is greater than 10 m/s the perpendicular gradient component of pressure, $\nabla_\perp P$, is negligible over scales greater than 1 km while $\mathbf{g} \times \mathbf{b}$ is even smaller. Our equation in this case reduces to:

$$0 = \frac{q_\alpha}{|q_\alpha|}\Omega_\alpha \left(\frac{\mathbf{E}'_\perp \times \hat{b}}{B} - (\mathbf{V}_\alpha - \mathbf{V}_n)_\perp \right) - \nu_{\alpha n} (\mathbf{V}_\alpha - \mathbf{V}_n) \times \hat{b} \qquad (1.4)$$

This can be rearranged to yield:

$$(\mathbf{V}_\alpha - \mathbf{V}_n)_\perp = \frac{\mathbf{E}'_\perp \times \hat{b}}{B} - \frac{|q_\alpha|\nu_{\alpha n}}{q_\alpha \Omega_\alpha} (\mathbf{V}_\alpha - \mathbf{V}_n) \times \hat{b} \qquad (1.5)$$

This can be solved generally, but by recognizing that in the F-region $\nu_{\alpha n}$ is much less than Ω_α, one can write:

$$(\mathbf{V}_\alpha - \mathbf{V}_n)_\perp \approx (\mathbf{V}_\alpha - \mathbf{V}_n)^{(0)}_\perp + \frac{\nu_{\alpha n}}{\Omega_\alpha} (\mathbf{V}_\alpha - \mathbf{V}_n)^{(1)}_\perp \qquad (1.6)$$

This gives:

$$(\mathbf{V}_\alpha - \mathbf{V}_n)_\perp^{(0)} = \frac{\mathbf{E'}_\perp \times \hat{b}}{B} \tag{1.7}$$

and

$$\begin{aligned}(\mathbf{V}_\alpha - \mathbf{V}_n)_\perp^{(1)} &= -\frac{q_\alpha}{|q_\alpha|}\left(\mathbf{V}_\alpha - \mathbf{V}_n\right)_\perp^{(0)} \times \hat{b} \\ &= -\frac{q_\alpha}{|q_\alpha|}\left(\frac{\mathbf{E'}_\perp \times \hat{b}}{B}\right) \times \hat{b} \\ &= \frac{q_\alpha \mathbf{E'}_\perp}{|q_\alpha| B}\end{aligned} \tag{1.8}$$

The final result is:

$$(\mathbf{V}_\alpha - \mathbf{V}_n)_\perp \approx \frac{\mathbf{E'}_\perp \times \hat{b}}{B} + \frac{\nu_{\alpha n}}{\Omega_\alpha}\frac{q_\alpha \mathbf{E'}_\perp}{|q_\alpha| B} \tag{1.9}$$

or equivalently:

$$\mathbf{V}_{\alpha\perp} \approx \frac{\mathbf{E'}_\perp \times \hat{b}}{B} + \frac{\nu_{\alpha n} q_\alpha \mathbf{E'}_\perp}{\Omega_\alpha |q_\alpha| B} + \mathbf{V}_{n\perp} \tag{1.10}$$

Equation 1.10 describes plasma motion that is perpendicular to the magnetic field in the F-region ionosphere.

Motion Parallel to the Geomagnetic Field

To find motion parallel to the magnetic field, one can take a dot product of equation 1.2 along the magnetic field line to obtain:

$$\begin{aligned}0 &= \frac{q_\alpha}{|q_\alpha|}\Omega_\alpha\left(\frac{\mathbf{E'}}{B} + \left(\mathbf{V}_\alpha - \mathbf{V}_n\right) \times \hat{b}\right) \cdot \hat{b} - \nu_{\alpha n}\left(\mathbf{V}_\alpha - \mathbf{V}_n\right) \cdot \hat{b} - \frac{\nabla P_\alpha}{\rho_\alpha} \cdot \hat{b} + \mathbf{g} \cdot \hat{b} \\ &= \frac{q_\alpha}{|q_\alpha|}\Omega_\alpha \frac{\mathbf{E}_{||}}{B} - \nu_{\alpha n}\left(\mathbf{V}_{\alpha||} - \mathbf{V}_{n||}\right) - \frac{\nabla_{||} P_\alpha}{\rho_\alpha} + \mathbf{g}_{||}\end{aligned} \tag{1.11}$$

Here, there is only one term for $\mathbf{V}_{\alpha||}$, making it easy to obtain the following solution:

$$\mathbf{V}_{\alpha||} = \left(\frac{q_\alpha \Omega_\alpha \mathbf{E}_{||}}{|q_\alpha| B} - \frac{\nabla_{||} P_\alpha}{\rho_\alpha} + \mathbf{g}_{||}\right)\frac{1}{\nu_{\alpha n}} + \mathbf{V}_{n||} \tag{1.12}$$

Equation 1.12 describes plasma motion along a magnetic field line in the ionosphere.

1.4.2 Energy and Plasma Temperature

Now that relevant plasma momentum mechanisms have been briefly discussed, the energy balance in the F-region ionosphere can be considered. This section briefly discusses heating processes relevant to the present study.

Ion Temperature

The general ion energy equation can be written as (*St.-Maurice and Hanson*, 1982):

$$\begin{aligned}
&\frac{3}{2}\left(\frac{D}{Dt}P_i + P_i\nabla\cdot\mathbf{V}_i\right) + \nabla\cdot\mathbf{q}_i + \mathbf{P}_i : \nabla\mathbf{V}_i \\
&= \sum_n \frac{n_i m_i \nu_{in}}{m_i + m_n}\left[3k_b(T_n - T_i)\psi_{in} + m_n(\mathbf{V}_i - \mathbf{V}_n)^2\phi_{in}\right] + \\
&n_i\nu_{ie}3k_b(T_e - T_i) + n_i\nu_{ie}m_e\left(\mathbf{V}_i - \mathbf{V}_e\right)^2
\end{aligned} \tag{1.13}$$

where t is time, $\frac{D}{Dt}$ is the convective derivative $\left(\frac{\partial}{\partial t} + \mathbf{V}_i\cdot\nabla\right)$, P_i is the ion pressure, $\mathbf{V}_i$ and $\mathbf{V}_e$ are the velocities of ions and electrons, respectively, $\mathbf{q}$ is the heat flow, $\mathbf{P}$ is the stress tensor, n_i is the number density of ions, m_i, m_e and m_n are the masses of ions, electrons and neutrals, respectively, ν_{in} is the ion-neutral collision frequency, ν_{ie} is the ion-electron collision frequency ($\nu_{ie} \approx 54.5 n_e T_e^{-3/2}$), k_b is the Boltzmann constant, T_i, T_e and T_n are the temperatures of ions, electrons and neutrals, respectively, $\sum_n$ is the sum over different neutrals, and ψ_{in} and ϕ_{in} are functions of order 1. On the left-hand side of equation 1.13 is the rate of change of internal energy, adiabatic heating/cooling (heating/cooling due to a pressure change), ion heat flow and viscous heating. The right side contains heat exchange between neutrals and ions, frictional heating through the relative drift of ions and neutrals, heat exchange between electrons and ions, and frictional heating through a relative drift between ions and electrons.

Equation 1.13 can be reduced considerably for F-region applications. The collision frequency is large in the F-region, typically over times extending longer than $1/\nu_{in}$, meaning that $\frac{\partial}{\partial t}$ is zero after a few seconds at most (*Schunk*, 1975). Also, because ν_{in} is large, heat advection, conduction and viscous heating are negligible at F-region altitudes, so that $\mathbf{V}_i\cdot\nabla p_i$, $\nabla\cdot\mathbf{q}_i$ and $\mathbf{P}_i : \nabla\mathbf{V}_i$ are approximately zero (*Schunk*, 1975; *Schunk and Sojka*, 1982). ψ_{in} and

ϕ_{in} are approximately 1 because $\mathbf{O}^+$ and $\mathbf{O}$ are the dominant gases ($\sum_n = \sum_1$) (*St.-Maurice and Hanson*, 1982). Since $\nabla \cdot (\mathbf{E} \times \mathbf{B})$ is zero (because $\frac{\partial \mathbf{B}}{\partial t}$ can be assumed to be small), $\nabla \cdot \mathbf{V}_i$ is negligible (*Rishbeth and Hanson*, 1974). Given the altitude being examined, as well as the small mass of electrons, to leading order equation 1.13 can then be written as (*St.-Maurice and Hanson*, 1984):

$$T_i \approx \frac{\frac{m_n}{3k_b}(\mathbf{V_i} - \mathbf{V}_n)^2 + T_n + \frac{m_i+m_n}{m_i}\frac{\nu_{ie}}{\nu_{in}}T_e}{1 + \frac{m_i+m_n}{m_i}\frac{\nu_{ie}}{\nu_{in}}} \tag{1.14}$$

From this equation, it can be seen that only a few factors affect the F-region ion temperature, namely, the electron temperature, the neutral temperature, the mean neutral mass and the relative drift between ions and neutrals. It should also be mentioned that, because ion heating and cooling comes from elastic collisions, the ions heat up at the same rate as they cool down, namely over a time scale of $1/\nu_{in}$, which is seconds below 400 km (*Schunk*, 1975).

The relative drift between ions and neutrals has the strongest impact on ion temperature in the F-region. The term that depends on the relative drift is specifically referred to as frictional heating. A key driver for frictional heating is electric fields. When an electric field is introduced, charged particles will move with an $\mathbf{E} \times \mathbf{B}$ drift relative to neutral particles, which can be quite large (several km/s at times). This process is most effective below roughly 400 km because at higher altitudes the collision frequency is not large enough and other processes compete with the simple notion of local friction. It is possible for higher areas to be affected by this heating lower down, in effect through heat conduction, but for this to occur there must be exceptionally hot frictional heating (*Loranc and St.-Maurice*, 1994). In the F-region, frictional heating is a major mechanism behind ion temperature enhancements, and, to a smaller degree, electron temperature enhancements.

Electron Temperature

Electron heating is governed in much the same way that ion heating is. Electrons can be heated through frictional heating via collisions with neutrals just like ions are. In other words, frictional heating through equation 1.14 applies to electrons as well. Not only collisions with neutrals will heat electrons, elastic collisions with hotter ions will pass heat onto electrons (*Schunk and Nagy*, 1978). As well, electrons can be heated through other processes that

are less effective in heating ions, such as conduction and heating through chemical reactions involving photoproduction or production by energetic precipitating particles. Essentially, during the photoionization process, photoelectrons are created. These photoelectrons will gain kinetic energy from the photoionization process (*Schunk and Nagy*, 1978). This raises the overall temperature of electrons.

Frictional heating, however, is a much less effective mechanism for electrons then for ions, due to the importance of inelastic collisions in cooling electrons. Although ions cool at the same rate that they heat, electrons cool at a faster rate than they heat. This is because electrons are heated by elastic collisions, but cool through inelastic collisions [*Schunk and Nagy* (2000), Chapter 9]. These inelastic collisions mostly excite vibrational N_2 and the fine structures of O (*Perkins and Roble*, 1978). This is emphasized in Figure 1.15, which shows different electron cooling rates as a function of altitude (or height). The ones of importance here are L_e and Q_e, which are the electron cooling and heating rates, respectively. As can be seen, below roughly 400 km the electron cooling rate is greater than the heating rate. Given that this is a steady state, the imbalance forces heat to flow from one altitude to another. In typical situations, such as the one illustrated in Figure 1.15, the heat flows downward from the upper altitudes.

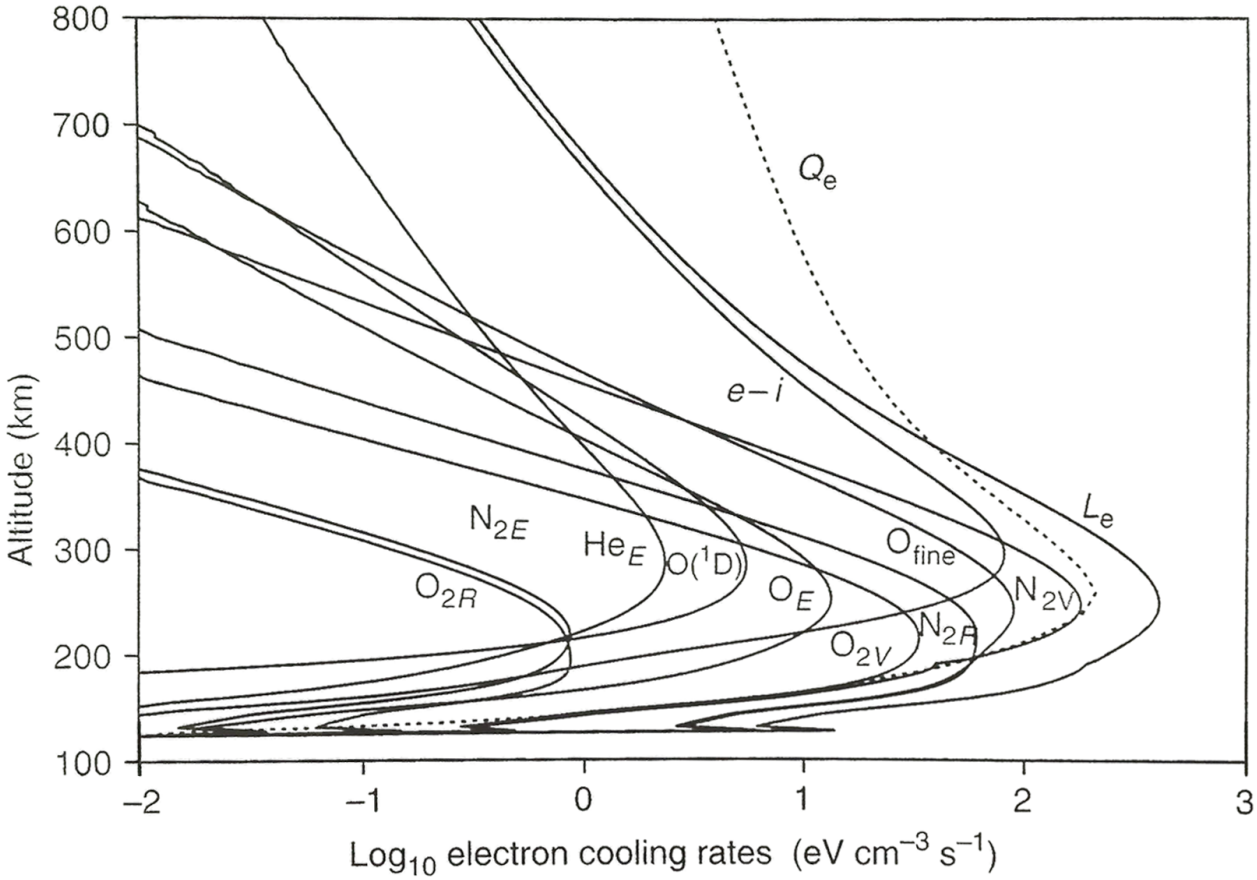

Figure 1.15: Electron cooling rates as a function of altitude. In this figure, L_e is the electron cooling rate, Q_e is the electron heating rate, subscripts R, V and E represent cooling rates associated with rotational, vibrational and elastic collisions, respectively, O(^1D) is loss due to excitation of O to the ^1D state, O_{fine} is loss due to excitation of fine structures in O and $e - i$ is losses in Coulomb collisions between ions and electrons [*Schunk and Nagy* (2000), Chapter 9].

Chapter 2

Instrumentation

In order to better understand ionospheric dynamics and electrodynamics, several techniques are used. These techniques include probes on satellites, rockets or balloons, drift measurements of chemical releases, and RAdio Detection And Ranging (RADAR or radar) stations (*Park*, 1976). Being that radars are the focus of this work, they will be examined carefully. Other instrumentation will be briefly described later in this Chapter.

2.1 Ionospheric Radars

A popular way to analyze electric fields is radars, which send radio signals into the ionosphere with radar echoes relaying information about the plasma. Different radar systems can relay different information about plasma. For example, the Super Dual Auroral Radar Network (SuperDARN) is a group of coherent radars which are able to output information relating to the line of sight velocity of plasma, spectral width and received power. This radar network is great at examining irregularities and interpreting electric fields on a global scale, however, it misses smaller structures. This is where Incoherent Scatter Radars (ISRs) are useful. For a finite region of space involving roughly (500 km)^3 or 10^8 km^3, ISRs can provide high resolution measurements in both time [down to second scales] and space [down to 100 m scales]. From ISR radio wave echoes, one can interpret the ion temperature, ion velocity, electron temperature and electron density. These parameters can then be used to infer changes in the F-region density, neutral atmosphere motion and electric fields (*Evans*, 1972). ISRs are particularly important because temperature values are generally difficult to come by (the only other means to get them is through rocket or satellite measurements). As well, they provide more detailed electron density profiles of the atmosphere than other sources,

like ionosondes.

Before ISR data can be properly examined, it is critical to first understand what the data mean and how they are derived. In the following, the theory behind incoherent scatter data is examined, as well as information about the specific radar being used, including its data set.

2.1.1 Incoherent Scatter Radars

When ISRs send out radio waves into the ionosphere they read in signals that have bounced off a large number of electrons. This results from operating at a frequency that is so high that only electrons react to the electromagnetic wave [*Hagfors* (1995), Chapter 1]. Originally, it was intended for ISRs to detect incoherent scattering, which is the result of electrons exhibiting independent and free behavior (*Gordon*, 1958). However, because these radars operate at a wavelength that is greater than the Debye length (the thickness of a cloud of charges shielding a potential in a plasma), they actually receive echoes from collective effects, called coherent scattering [*Sheffield* (1975), Chapter 1]. In coherent scattering the electrons are not free and independent, as they are orbiting ions and shield them through a negative cloud (Debye shielding) [*Chen* (2006), Chapter 1]. This means that ISRs are actually coherent scatter radars. The only difference between "coherent" radars and ISRs is that the latter probes the much smaller wave amplitudes from a stable plasma in near thermal equilibrium. This means, for one thing, that ISRs require much more power than coherent scatter radars.

Since ISRs send signals that probe large groups of charged particles, the echoes detected by these radars are different than those that observe a single hard target. In an ISR, the echo will contain a range of shifted frequencies, instead of a single shifted frequency, owing to random thermal motion on the molecular scale. This random motion occurring from a large group of charged particles causes a wide spectrum of waves (*Sedgemore-Schulthess and St.-Maurice*, 1982). This means that when a radar sends out a radio wave into the atmosphere, it receives more than one Doppler shift because the waves move about the mean Doppler shift. The radar then recovers the waves that decay the least, namely the ion acoustic waves (*Sheffield*, 2010). Regardless of this range of shifted frequencies, it follows from the thermal equilibrium of plasma waves in the plasma that the radar backscatter spectrum is a known

function of frequency. A distinct spectrum is extracted by assuming a Maxwellian (the distribution associated with the velocities for particles in a gas near thermal equilibrium).

When the effect of collisions can be neglected (appropriate above 110 km altitude), the general expression for an arbitrary backscatter spectra, $S(\mathbf{k},\omega)$, from an unmagnetized, low-temperature, singly-ionized plasma is given by [*Sheffield* (1975), Chapter 7]:

$$S(\mathbf{k},\omega) = \frac{2\pi}{k}\left|1 - \frac{G_e}{\epsilon}\right|^2 f_{e0}\left(\frac{\omega}{k}\right) + \frac{2\pi}{k}\left|\frac{G_e}{\epsilon}\right|^2 f_{i0}\left(\frac{\omega}{k}\right) \tag{2.1}$$

where $\mathbf{k}$ is the wavenumber ($\mathbf{k} = \mathbf{k}_i - \mathbf{k}_s$, where $\mathbf{k}_i$ is the incident wavenumber and $\mathbf{k}_s$ is the scattered wavenumber), ω is the angular frequency ($\omega = \omega_i - \omega_s$, where ω_i is the incident angular frequency and ω_s is the scattered angular frequency), ϵ is the dielectric function for ω real, and f_{i0} and f_{e0} are the normalized one-dimensional velocity distribution functions of ions and electrons, respectively. Here, $\epsilon = 1 + G_e + G_i$, where G_e is:

$$G_e(\mathbf{k},\omega) = \int_{-\infty}^{+\infty} d\mathbf{V} \frac{4\pi e^2 n_{e0}}{m_e k^2} \frac{\mathbf{k}\cdot\nabla_{\mathbf{V}} f_{e0}}{\omega - \mathbf{k}\cdot\mathbf{V} - i\gamma} \tag{2.2}$$

and G_i is:

$$G_i(\mathbf{k},\omega) = \int_{-\infty}^{+\infty} d\mathbf{V} \frac{4\pi e^2 n_{i0}}{m_i k^2} \frac{\mathbf{k}\cdot\nabla_{\mathbf{V}} f_{i0}}{\omega - \mathbf{k}\cdot\mathbf{V} - i\gamma} \tag{2.3}$$

with e the charge of an electron, n_{i0} and n_{e0} the normalized ion and electron number densities, respectively, and γ a small dampening term to account for causality (*Sheffield*, 1975). Parameters in Equation 2.1 are modified by ϵ such that when ϵ approaches 0, the peaks grow. When ϵ is zero, an eigenfrequency is obtained. For stable plasmas the eigenfrequency has a negative imaginary part. Note that if α is defined such that $\alpha^2 = 1/(k\lambda_D)^2$, where λ_D is the Debye length, the spectrum would truly become incoherent if α approached 0 (for coherent scattering $\alpha \geq 1$). In this truly incoherent scatter limit, equation 2.1 would become:

$$S(\mathbf{k},\omega)\,|_{\alpha\to 0} \to \frac{2\pi}{k} f_{e0}\left(\frac{\omega}{k}\right) \tag{2.4}$$

which simply states that the spectrum would reveal the electron velocity distribution. In general for $\alpha \neq 0$ and for a Maxwellian distribution function applicable to plasmas in near thermal equilibrium, $S(\mathbf{k},\omega)$ becomes:

$$S(\mathbf{k},\omega) = \frac{2\pi^{1/2}}{ka}\left\{\frac{A_e}{|\epsilon|^2} + \frac{A_i}{|\epsilon|^2}\right\} \tag{2.5}$$

with

$$A_e = \exp\left(-x_e^2\right)\left[\left(1+\alpha^2\frac{T_e}{T_i}\mathrm{R}w(x_i)\right)^2 + \left(\alpha^2\frac{T_e}{T_i}\mathrm{I}w(x_i)\right)^2\right] \tag{2.6}$$

and

$$A_i = \left(\frac{m_i T_e}{m_e T_i}\right)^{1/2}\exp\left(-x_i^2\right)\left[\left(\alpha^2\mathrm{R}w(x_e)\right)^2 + \left(\alpha^2\mathrm{I}w(x_e)\right)^2\right] \tag{2.7}$$

where $x_e = \omega/(ka)$, $x_i = \omega/(kb)$, $\alpha = 1/(k\lambda_D)$, $a = \left((2k_bT_e)/(m_e)\right)^{1/2}$ and $b = \left((2k_bT_i)/(m_i)\right)^{1/2}$. As well:

$$|\epsilon|^2 = \left[1+\alpha^2\left(\mathrm{R}w(x_e) + \frac{T_e}{T_i}\mathrm{R}w(x_i)\right)\right]^2 + \left[\alpha^2\mathrm{I}w(x_e) + \frac{\alpha^2 T_e}{T_i}\mathrm{I}w(x_i)\right]^2 \tag{2.8}$$

The real part of the plasma dispersion function, w, (Figure 2.1) is (*Fried and Conte*, 1961):

$$\mathrm{R}w(x) = 1 - 2x\exp\left(-x^2\right)\int_0^x \exp(p^2)dp \tag{2.9}$$

and the imaginary part of w, (Figure 2.1), is given by:

$$\mathrm{I}w(x) = \pi^{1/2}x\exp\left(-x^2\right) \tag{2.10}$$

The term A_e includes free electron contributions when $\alpha << 1$ and electron Debye shielding when $\alpha \geq 1$ while A_i includes scattering from electrons that are shielding ions.

At higher Doppler-shifted frequencies, x_i becomes much greater than 1 ($x_i \to \infty$), $A_i/|\epsilon|^2$ approaches zero, and x_e is small, leaving equation 2.5 largely dependent on $A_e/|\epsilon|^2$. These are called the "electron lines". However, for lower frequencies, the $A_i/|\epsilon|^2$ is greater when $T_e/T_i \approx 1$ and $A_e/|\epsilon|^2$ is greater when $T_e/T_i >> 1$ (brought on by an increase in the ion acoustic resonance). These are the "ion lines" of an ISR spectrum [*Sheffield* (1975), Chapter 7]. In most of the work done with ISRs, the ion line is used.

In the case of $T_e/T_i \approx 1$ at low frequencies, the so-called Salpeter approximation can be used, which is simply $\frac{x_e}{x_i} = \left(\frac{m_e T_i}{m_i T_e}\right)^{1/2} << 1$. In this scenario, the spectrum can be broken into two components:

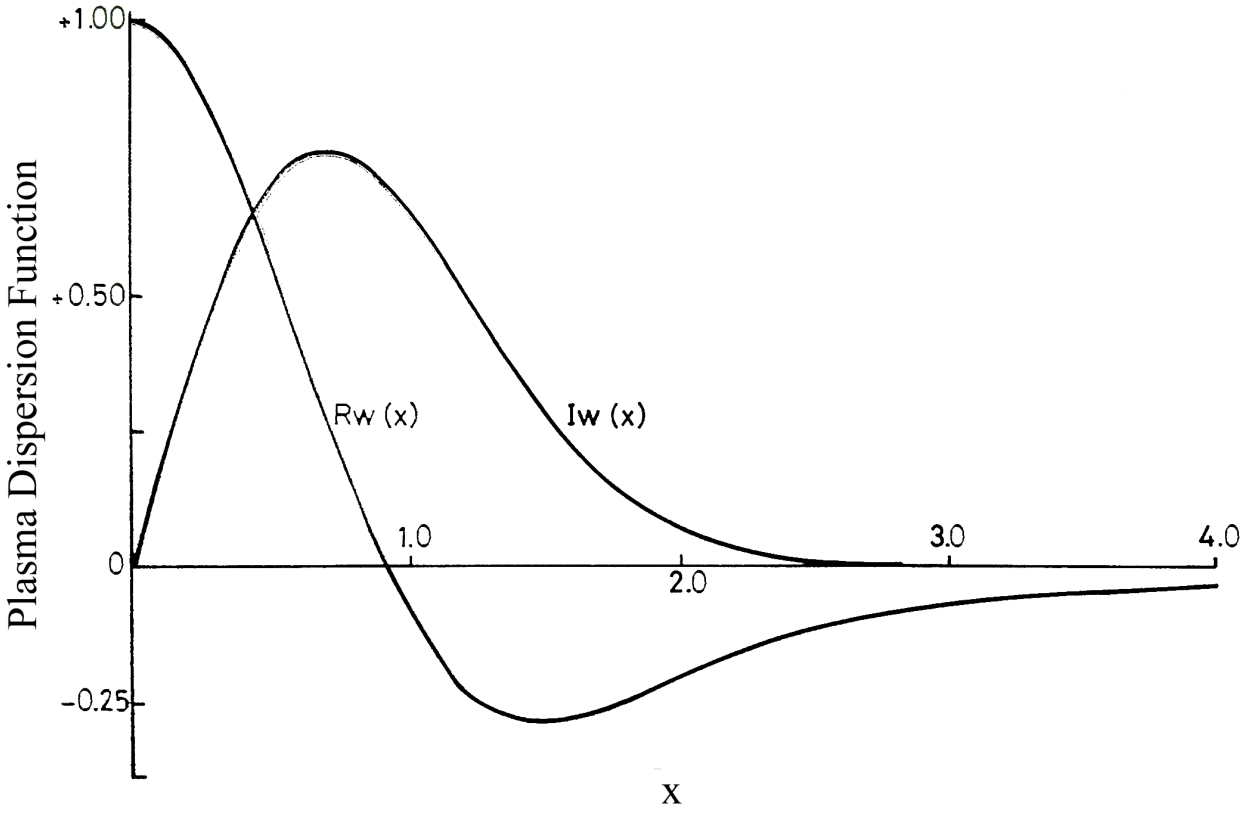

Figure 2.1: Real and imaginary components of the plasma dispersion function [*Sheffield* (1975), Chapter 7].

$$S(\mathbf{k},\omega) = S_e(\mathbf{k},\omega) + S_i(\mathbf{k},\omega) \tag{2.11}$$

The $S_e(\mathbf{k},\omega)$ term comes from the A_e term of equation 2.5, the ion acoustic resonance being weak because of the low frequency, as well as $\mathrm{R}w(x_i) \approx 0$ and $\mathrm{I}w(x_i) \approx 0$. This makes:

$$S_e(\mathbf{k},\omega) \approx \frac{2\pi^{1/2}\exp(-x_e^2)}{ka[(1+\alpha^2\mathrm{R}w(x_e))^+(\alpha^2\mathrm{I}w(x_e))^2]} \tag{2.12}$$

In addition $S_i(\mathbf{k},\omega)$ comes from A_i and the Salpeter approximation, bringing $\mathrm{R}w(x_e) \approx 1$ and $\mathrm{I}w(x_e) \approx 0$:

$$S_i(\mathbf{k},\omega) \approx \frac{2\pi^{1/2}\alpha^4\exp(-x_i^2)}{kb[1+\alpha^2+\alpha^2(T_e/T_i)\mathrm{R}w(x_i)]^2+[\alpha^2(T_e/T_i)\mathrm{I}w(x_i)]^2} \tag{2.13}$$

When equation 2.11 is plotted, the spectrum shown in Figure 2.2 is obtained. The feature seen in Figure 2.2 is the ion line, existing between electron lines (*Sedgemore-Schulthess and St.-Maurice*, 1982). The peaks in the ion line directly relate to the ratio between electron temperature and ion temperature, which relate to the inference of Landau damping. As the electron temperature increases, larger peaks will be seen in Figure 2.2 and the trough becomes deeper (*Ichimaru*, 1973). In some instances, the electron temperature can become so much greater than the ion temperature that two well-developed, almost separate, peaks will occur (*Wickwar et al.*, 1981). Conversely, if the electron temperature is equal to the ion temperature, as expected at lower altitudes due to strong collisional coupling, there would only be one large hump instead of two peaks and a trough. The vertical distance from the tip of the peak to the bottom of the trough in Figure 2.2 relates to the temperature ratio between ions and electrons, T_e/T_i. The ion acoustic speed is roughly half the distance between the two peaks. The shift in the frequency from the signal to the echo reflects the Doppler shift, which correlates to the ion velocity. Lastly, the integrated spectral power is approximately equal to $n_e/(1+T_e/T_i)$ if 2.11 is used, so that the electron density can be extracted, given that the ratio T_e/T_i can be determined from the spectral shape. In the same light, these parameters affect the shape of the autocorrelation function.

Of course there is more to analyzing the various plasma parameters than just fitting them to a function. Other factors affecting the spectral shape and the autocorrelation function

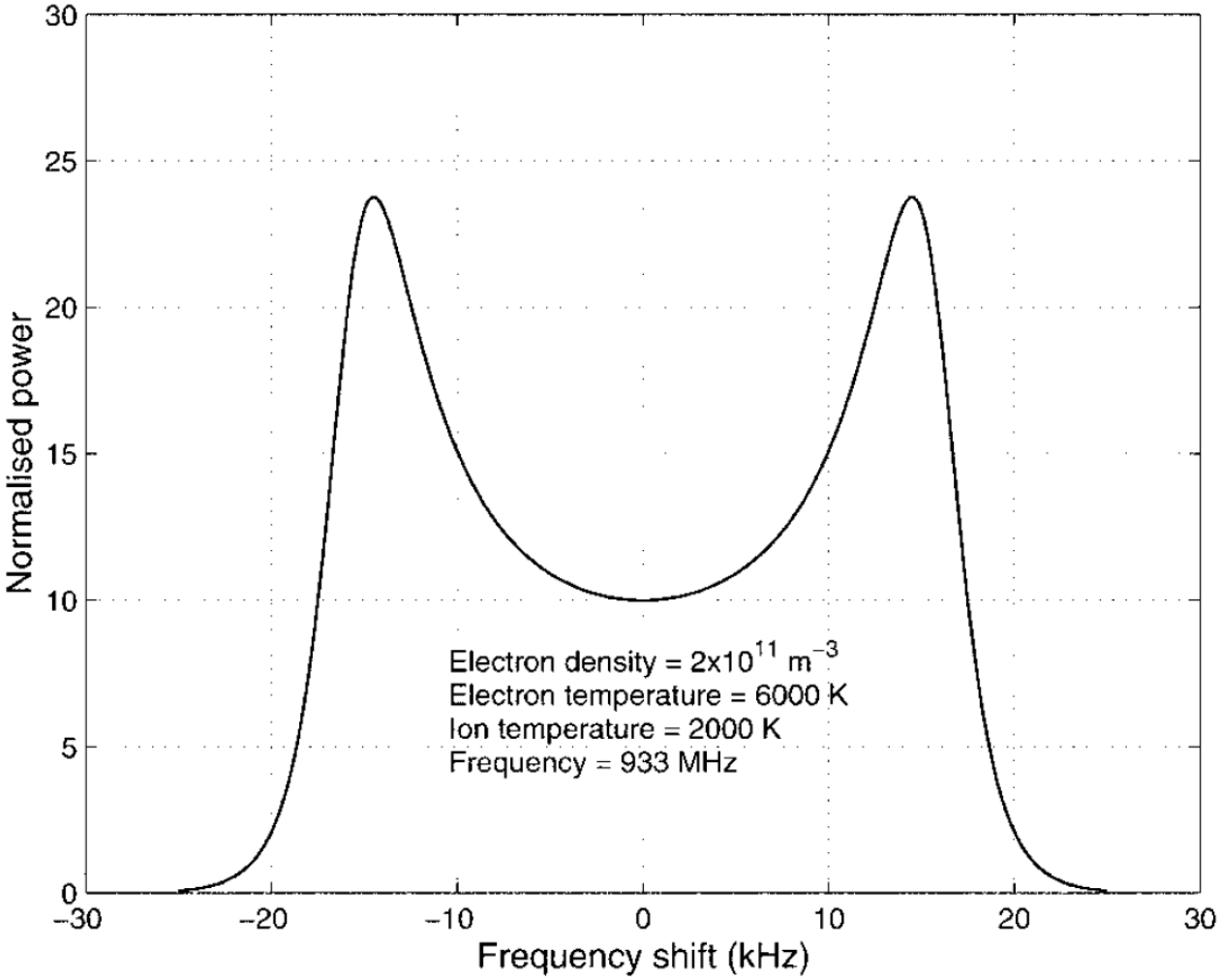

Figure 2.2: An example of the "ion line" in a backscatter spectrum received by an ISR (*Sedgemore-Schulthess and St.-Maurice*, 1982).

must be considered. Two of these worth mentioning briefly are noise and pulse coding. Noise is simply an unwanted addition to the signal received, which can arise from such processes as thermal noise. This generally grows with altitude or with distance traveled, lowering the signal to noise ratio at higher ranges. The bandwidth of the pulse also affects the noise, and as the bandwidth increases, so will the noise. This means that if the pulse width is reduced to improve the range resolution, more noise will be present (*Semeter*, 2012). The effects of noise are reduced through the use of a matched filter, which will increase the signal to noise ratio of a given signal.

Pulse coding is something different. When a radar sends out signals into the ionosphere, it does not send a continuous stream of waves, but rather a packet of waves, referred to as a pulse (see Figure 2.3). The size and frequency of the pulses (not the frequency of the waves) is determined by parameters such as power and desired range. An important factor in pulse coding is ambiguity, a distortion in the returned pulse introduced by the receiver matched filter (*Woodward*, 1975). More precisely, it is the absolute value of the output envelope of a matched filter when the input is a Doppler shifted echo of the original signal (*Heinselman*, 2012). An example is seen in Figure 2.4, which shows the ambiguity related to sensing a hard target with an uncoded pulse. Focusing on Figure 2.4, the Doppler domain is rather narrow, and the range domain is more spread out. This means that when there is a Doppler-shifted, point target return at 0 kHz there will be a central peak and little ambiguity in the Doppler shift. However, the range will have a larger ambiguity. If, for example, the Doppler shift is 50kHz, Figure 2.4 does not show a clear peak in the ambiguity function, meaning there will be more ambiguity in its location and velocity. However, sending out different pulses can result in different ambiguity functions (*Heinselman*, 2012).

With the above in mind, one is presented with the problem of trying to reconstruct the parameters that created the backscatter spectrum. By fitting equation 2.5 (which closely resembles the limit given by equation 2.11) to the data, plasma properties are extracted from the spectrum featured in Figure 2.2. This can be done by using a chi squared function:

$$\chi^2 = \sum_{j=1}^{n} \frac{[y(x_j) - model(x_j; \mathbf{p})]^2}{\sigma_j^2} \tag{2.14}$$

where y is the data, $\mathbf{p}$ is the parameter vector, x_j is the independent variable and σ_j is the

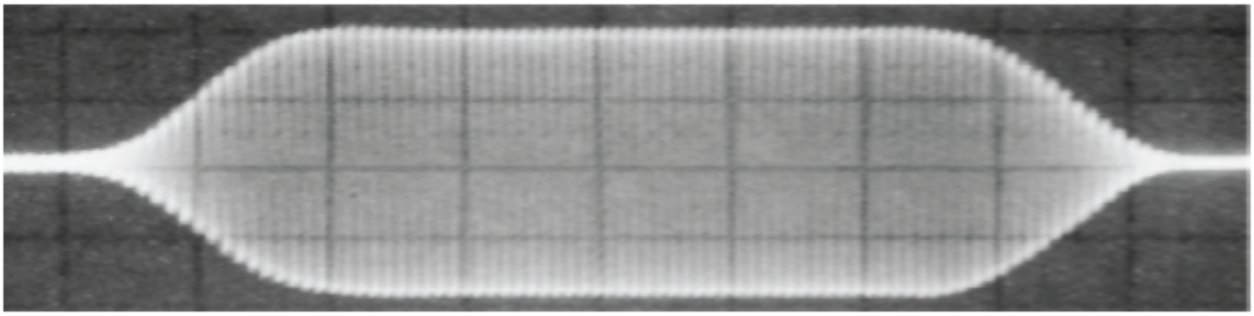

Figure 2.3: A single pulse sent out from a radar containing waves. (*Semeter*, 2012).

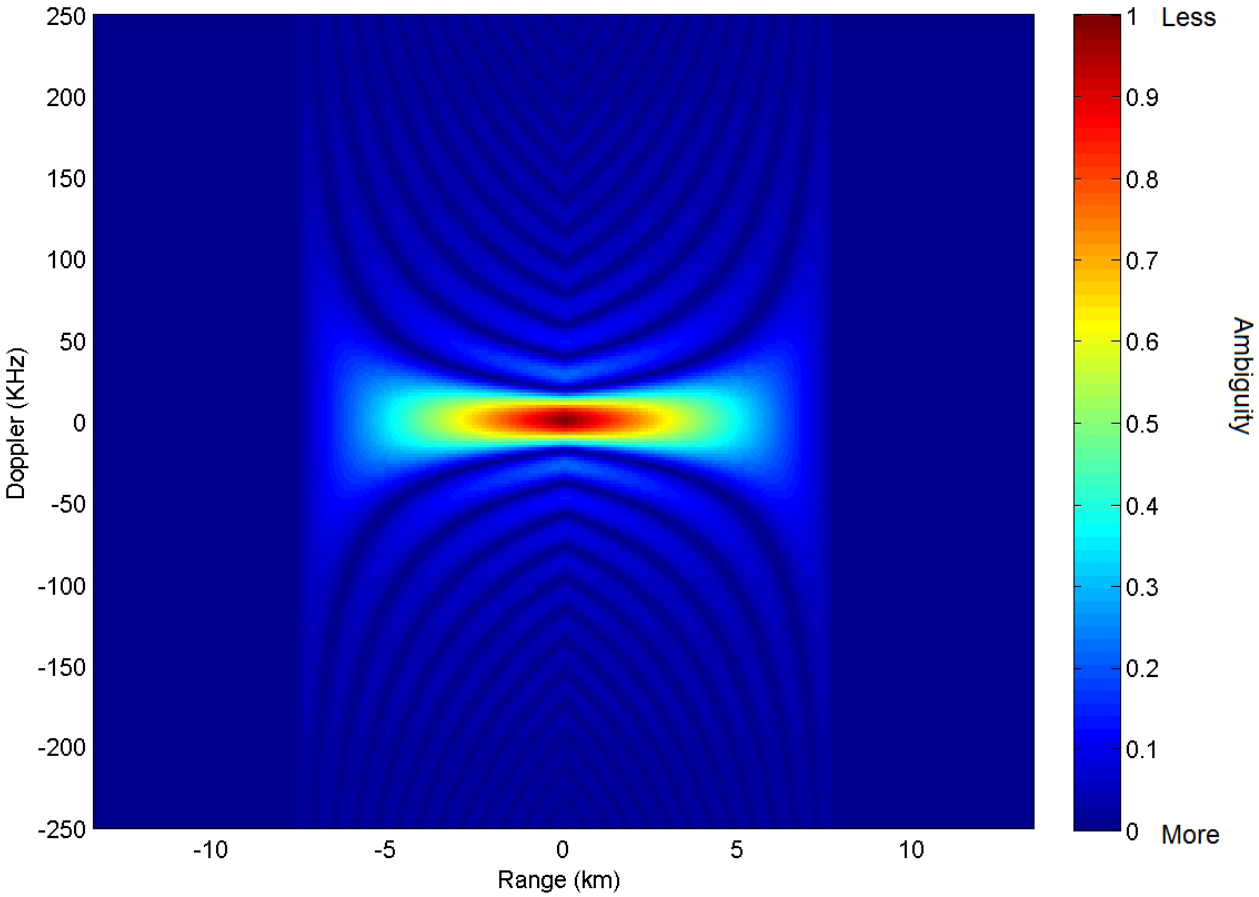

Figure 2.4: Ambiguity as a function of frequency and range for a 52μs uncoded pulse (*Heinselman*, 2012).

uncertainty. By minimizing χ, the model comes closer to the data (*Erickson*, 2012). A way to make the extraction easier is to constrain parameters by assuming an ion composition, or even using other instruments to approximate parameters.

2.1.2 PFISR and its characteristics

The data used for this research was collected from PFISR, located at the Poker Flat Research Range in Fairbanks, Alaska. Poker Flat is located at 64° N, an interesting geographic latitude at which to study the auroral oval since it happens to approximately match the geomagnetic latitude. This can be seen in Figure 2.5, where the offset is plotted between the geographic latitudes, which centre around the Earth's rotation, and the geomagnetic latitudes, which are centred on the geomagnetic poles (the Earth's magnetic poles, approximating the Earth to be a simple offset dipole magnet). Fairbanks illustrates how the geographic and geomagnetic happen to roughly match (Fairbanks is indicated on Figure 2.5 with a red dot). This is an important distinction to make at high latitudes (both geographic and geomagnetic) because the geographic and geomagnetic latitudes overlap. Being that there is an offset between the geomagnetic and geographic poles, regions of the Earth will move through different portions of the ionospheric convection pattern. As the Earth rotates, PFISR will view plasma in the corotation region, the auroral region, and the boundary between the two areas.

PFISR was the first "face" of the Advanced Modular Incoherent Scatter Radar (AMISR), the other two being in Resolute Bay, Nunavut (the Resolute Bay Incoherent Scatter Radars, RISR-N and RISR-C). It is one of only 12 ISRs worldwide, and is one of the few ISRs to make use of a phased array design. By using phased array antennas the signals of individual elements can be used to modify the radiation pattern, allowing for examination of a variety of directions all at once. The main advantage to a phased array design is that it does not need to be physically steered in different directions. This, in turn, means that the operator can get pulse-to-pulse beam positioning so the radar can sample spatially with superior flexibility. Spatial and temporal uncertainties are reduced, and there is no need to determine the integration ahead of time. In addition, in-beam imaging is possible (*Heinselman*, 2012). Additional specifications are listed in Table 2.1.

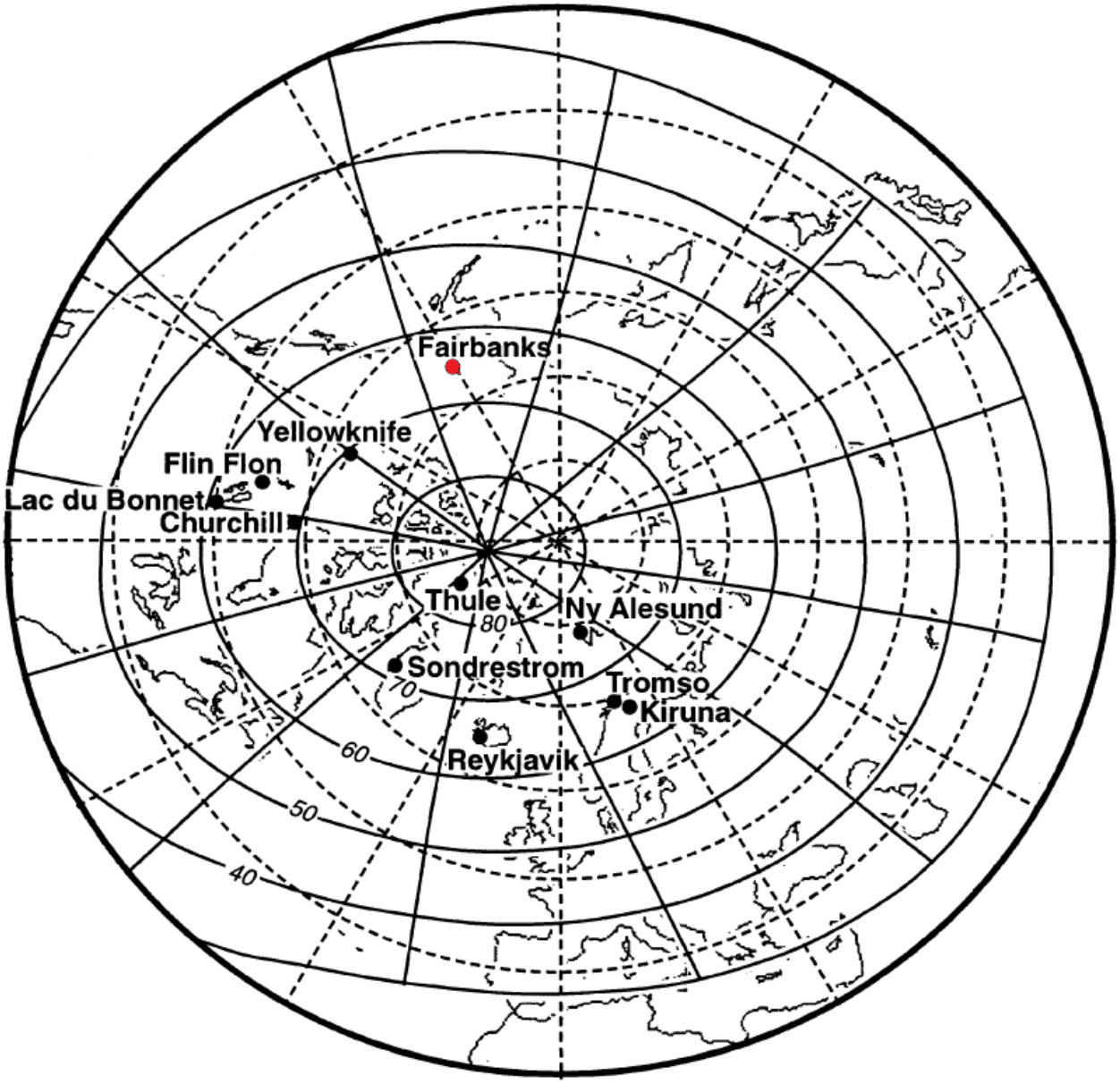

Figure 2.5: Geomagnetic coordinates (solid lines) and geographic coordinates (dashed lines). The red dot indicates Fairbanks, Alaska, the approximate location of PFISR (*Aarons and Lin*, 1999).

Table 2.1: Additional specification for AMISR/PFISR (*Heinselman*, 2012).

Year Deployed	2006
Geomagnetic Dip angle	77° 32'
Invariant Latitude	66° 7' N
Local Time	UT - 9
Magnetic Local Time	UT - 11:20
Peak Power	2 MW
Max Radio Frequency Duty	10%
Pulse Length	1 μsec - 2 msec
Transmission Frequency	430-450 MHz
Antenna Gain	Roughly 43 Decibels relative to an isotropic antenna
Antenna Aperture	Roughly 715 m^2
Beam Width	Roughly 1.1°
System Temperature	Roughly 120 K
Steering	Pulse to pulse over roughly ± 25°
Max Power Consumption	Roughly 700 KW
Max Operations	Continuous, depending on power
Data Volume	Roughly 6 TB/year at Poker Flat
Environment	-40°C to 35°C
Min Measurable n_e	Roughly 1×10^9 m^{-3}
Plasma Parameters	n_e, T_e, T_i, V_i, ν_{in}, composition
Derived Parameters	E, J, $\mathbf{V}_n$, Pedersen and Hall conductivity (σ_P, σ_H)

The data used for this research was taken from the IPY data sets collected during 2007 (*Sojka et al.*, 2009) and can be extracted from the Madrigal database, an online geospace database. A low duty, low power cycle was used in order to obtain continuous measurements. This resulted in long integration times in the original Madrigal data set (15 minutes), but shorter integrations could be done on demand. The data were routinely taken along the magnetic field lines between $-148°$ and $-147°$ longitude.

The PFISR data provided ion and electron temperatures, the electron density and the mean line-of-sight ion velocity as functions of the range and Universal Time (UT). Within these parameters, long (480 μs) and Alternating Code (AC) pulse measurements were taken. The differences between these pulses is the volume of integration and the resulting noise level, which resulted in long pulse measurements producing a 35 km resolution between 99 km and 663 km altitudes and AC pulse measurements producing results roughly every 4.39 km between 82 km and 346 km altitudes. The AC codes are necessary for altitudes like the E-region, where parameters can change on scales of a few kilometers. Given the altitude being examined in the present work, only the long pulse measurements were used.

2.1.3 Coherent Scatter Radars: SuperDARN

Though the majority of this research is based on PFISR data, SuperDARN, a network of coherent radars, is also used in this work. A system of over 30 radar stations, SuperDARN is a continually operating network of radars located in both the northern and southern hemispheres. These High Frequency (HF) radars operate at lower power, examining plasma in the ionosphere at mid- and high-latitudes (*Greenwald et al.*, 1995). These radars send out radio waves and receive backscatter echoes from irregularities in the E and F-regions of the ionosphere (*Greenwald et al.*, 1995). These backscatter echoes relay information regarding the line of sight velocity of plasma, the power received and the spectral width.

These radars operate at HF (10-20 MHz) in order to bend rays. SuperDARN uses refraction in order to scatter off of irregularities that are aligned with the magnetic field, with the wavevector, $\mathbf{k}$, perpendicular to the magnetic field. The typical resolution is 45 km and the

field of view is 2.5° in angle.

The SuperDARN radars have overlapping fields of view (common-volume areas). The SuperDARN network has the ability to map the direction and velocity of plasma irregularities over large regions, giving SuperDARN the ability to render ion convection maps of the ionosphere. This is done through an assimilation model wherein the drift and the convection pattern are described with up to typically 8 spherical harmonics. These harmonics are found by solving for the distribution of electrostatic potential from the measurements (in regions where there is no coverage or no data, statistical models constrain the solutions) (*Ruohoniemi and Baker*, 1998). Then the data is constrained to $\mathbf{E} \times \mathbf{B}$ drift, which is the drift created in the the high-latitude ionosphere from magnetospheric electric fields. Lastly, by minimizing the differences between the observations and the model, a convection map of the ionosphere is created. An example of one of these maps is given in Figure 2.6. Maps of these sorts were used in the study at hand.

2.2 Other Instrumentation

Satellites, rockets, balloons and chemical releases (in conjunction with other instruments (*Haerendel*, 1967)) provide in-situ information about electric fields (*Maynard and Heppner*, 1970; *Mozer and Bruston*, 1967; *Mozer and Serlin*, 1967). The Defense Meteorological Satellite Program (DMSP), for example, measures the electric field of the ionosphere using drift meters (*Holt*, 1992). The direction of the arriving charged particle beam in relation to the collector's normal is found through the use of a segmented collectors and gridded collimator, allowing the drift velocity to be determined. Figure 2.7 shows the cross-section of the gridded collimator and collectors. Figure 2.8 shows the collector configuration and the square entrance aperture, providing the angle of arrival of the plasma, vertical and horizontal ion velocities, and the currents to the collector segments (proportional to the collector area illuminated).

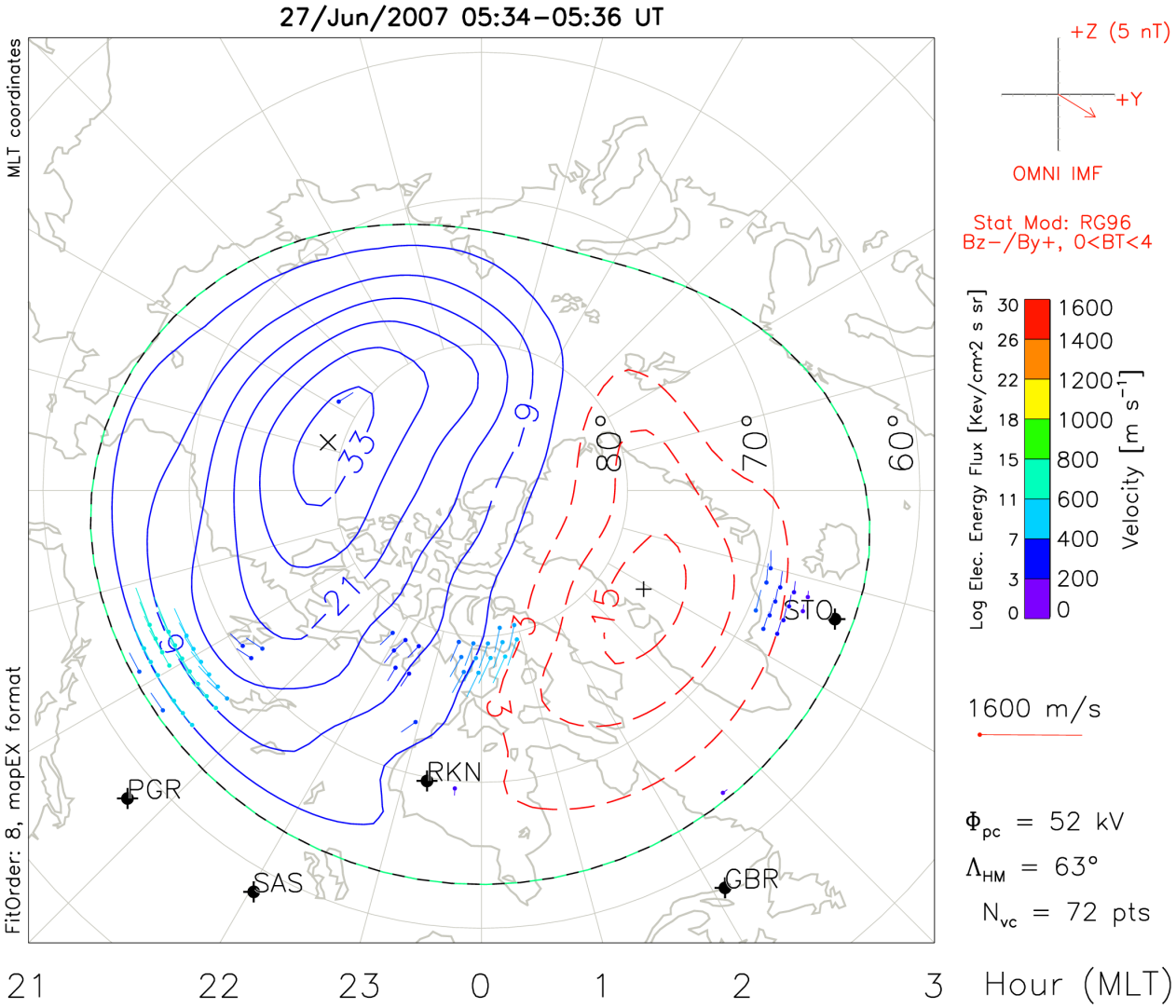

Figure 2.6: A SuperDARN convection map.

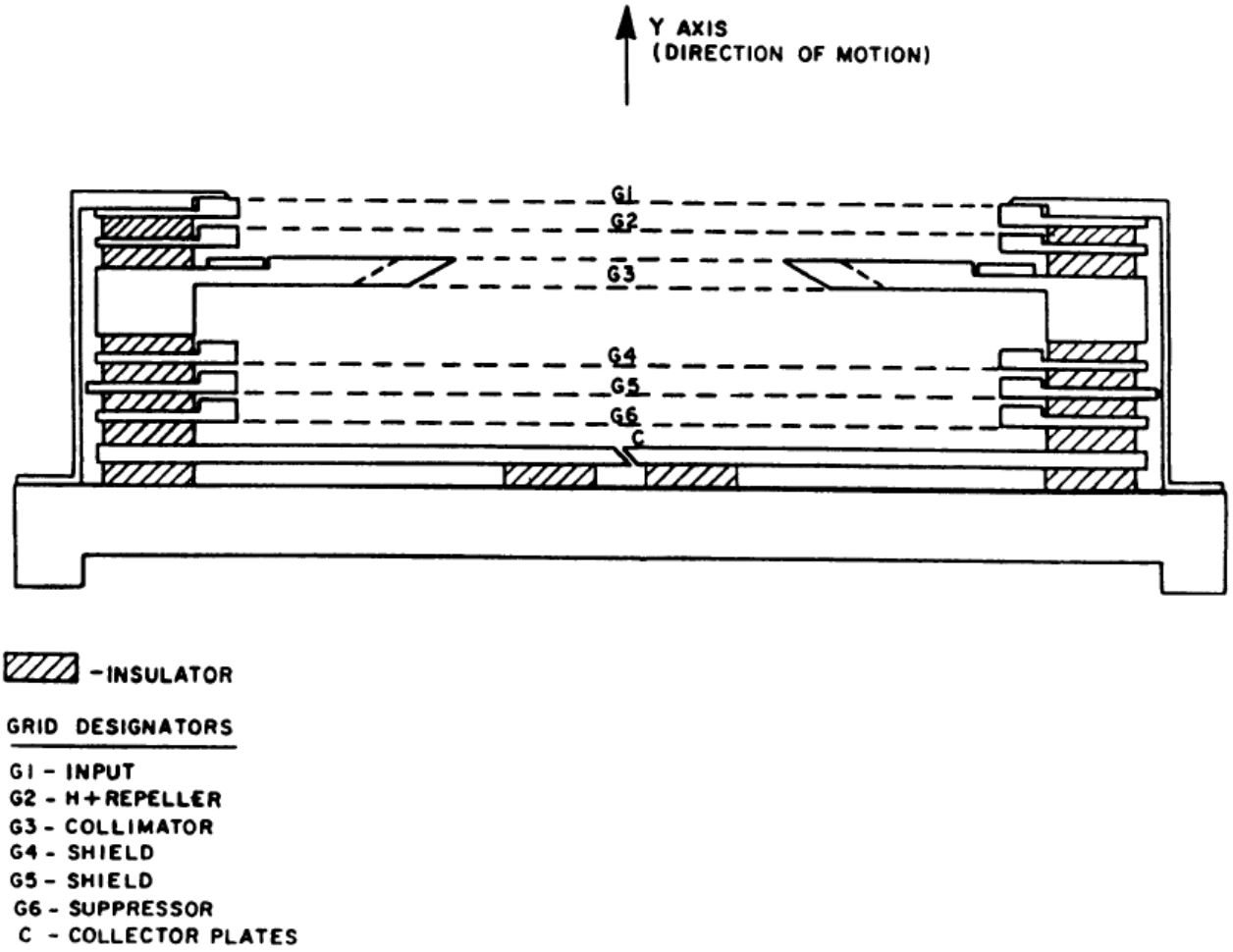

Figure 2.7: Diagram of the drift sensor cross section featuring the gridded collimator and collectors. The spacecraft has the x-axis pointing toward the center of the earth and the z-axis is perpendicular to the orbit plane (*Holt*, 1992).

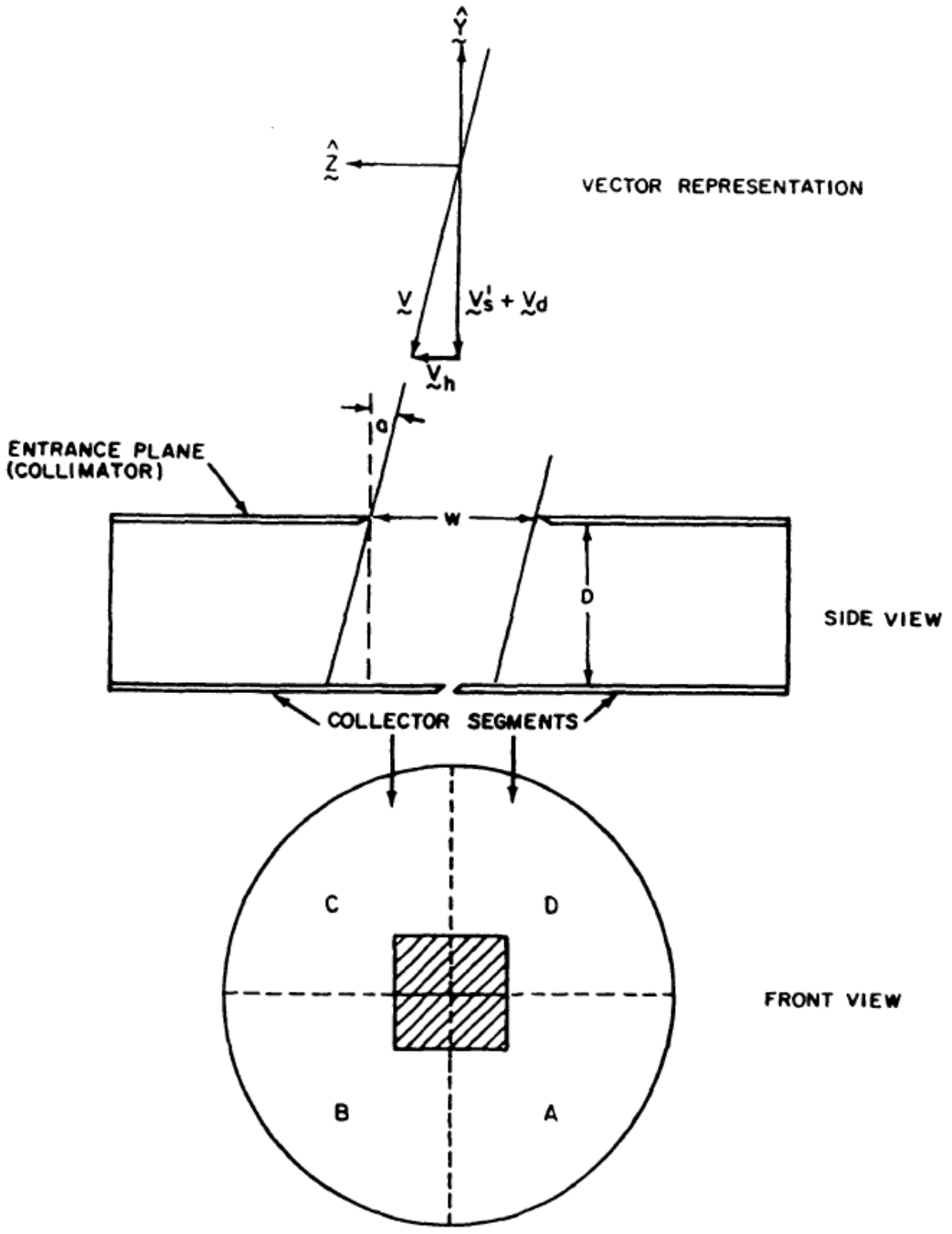

Figure 2.8: Diagram of the collector configuration and the square entrance aperture. The spacecraft has the x-axis pointing toward the center of the earth and the z-axis is perpendicular to the orbit plane (*Holt*, 1992).

Chapter 3

Data and Analysis

For this thesis, PFISR data from the IPY dataset were taken and analyzed. This research has focused on specific reoccurring dusk enhancements in the ion temperature in simultaneity with steep decreases in electron density. In the following sections these features are presented and their context identified.

3.1 Data Overview

3.1.1 PFISR Data

The data of most interest to this work come from long pulse measurements obtained by PFISR during the period of 27/June/2007 to 5/July/2007. The measurements were obtained by looking along the magnetic field direction at a reduced power so that a 15-minute integration time was routinely used to extract plasma parameters from the spectral observations (see Chapter 2 for more information). Plasma (or electron) number densities, ion velocities, and ion and electron temperatures were recorded as functions of altitude and UT. Daily Range-Time-Intensity (RTI) plots of the kind shown in Figure 3.1 (27/June/2007) were made of the parameters as a function of altitude and UT (refer to Table 2.1 for conversions to magnetic coordinates). Though more altitude bins are available, we focus here on 200 km to 400 km altitude bins because of the simpler physics taking place there and also because the data have a high signal to noise ratio (good quality data). These plots serve to highlight the different processes affecting each plasma parameter in the F-region relative to time, altitude and other controlling factors.

The ion temperature (T_i) during a day ranges from approximately 700 K to 1300 K and

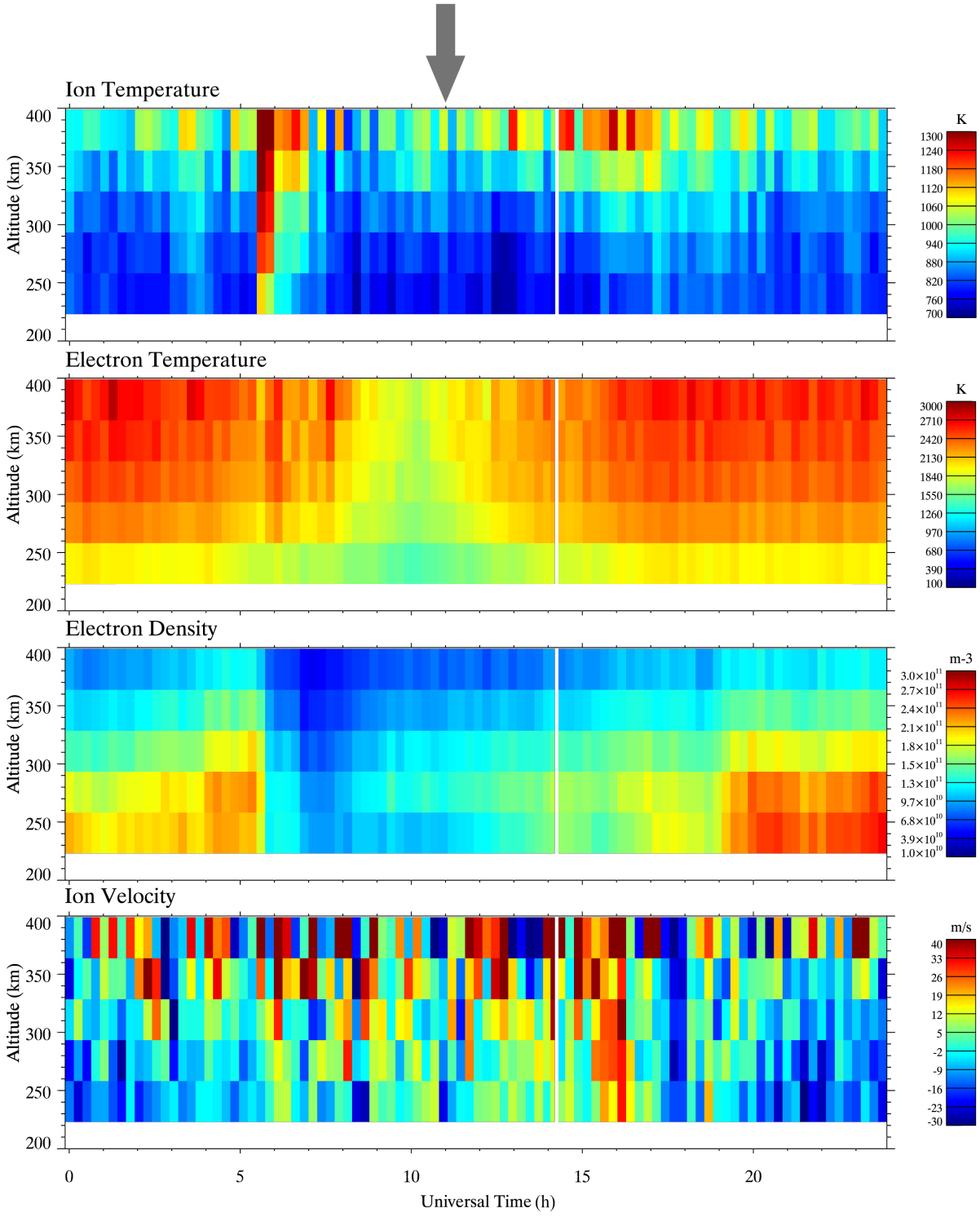

Figure 3.1: RTI plots of parameters with 15-minute integration bins on 27/June/2007. (Top Panel) T_i. (Second Panel from the Top) T_e. (Third Panel from the Top) n_e. (Bottom Panel) $\mathbf{V}_i$, positive values are away from the radar. The arrow at the top indicates the approximate location of local midnight in Magnetic Local Time (MLT) coordinates (11:20 UT).

increases with height, as seen in Figure 3.1 (top panel). Around 6 UT and 17 UT, two different regions of T_i increases occur. This first enhancement is seen as a steep increase, changing the temperature from roughly 800 K to 1100 K around 250 km and approximately 1000 K to 1300 K near 400 km, with a sharp transition within one 15-minute time interval. The second T_i increase is considerably more gradual and less intense, occurring over a much broader time interval and increasing by roughly 200 K below 300 km and about 500 K near 400 km. Because the first enhancement is so steep, we refer to it and any similar T_i enhancement as a "spike event". Given the steep and quick appearance of these spike events, it is easy for one to dismiss them as artifacts. However, the T_i spike events are seen in surrounding time and altitude bins, showing the spike is not isolated. As well, these spikes in T_i occur on multiple days at different times in the evening through a range of altitudes. This gives validity to the dataset[1].

The electron temperature (T_e) on 27/June/2007 ranges from roughly 1300 K to 2700 K, as seen in Figure 3.1 (second panel from the top). The temperature is reasonably consistent throughout the day with temperatures near 1900 K below 250 km and 2500 K near 400 km. A notable feature is the nighttime reduction, occurring for roughly six hours starting around 8 UT, and centred at 10 UT, which is close to 11 pm local time. In this region, the temperature reaches 1300 K below 250 km and 1700 K around 400 km.

Figure 3.1 (third panel from the top) shows the electron density (n_e) on 27/June/2007. The density is typically greatest around 250 km where it is roughly 2.8×10^{11} m^{-3}. The density is lower at higher altitudes, where it reaches 6×10^{10} m^{-3} at 400 km. A very clear sudden depletion occurs at roughly 6 UT and the depletion continues until approximately local midnight, extending from 250 km to 400 km. Near the beginning of the initial depletion (6 UT) at 250 km, the density changes by roughly a factor of two from about 2.2×10^{11} m^{-3} to 1.2×10^{11} m^{-3} over less than 30 minutes. The relative depletion is similar near 400 km, going from roughly 1.2×10^{11} m^{-3} to 8×10^{10} m^{-3} during the same time interval. This steep decrease in n_e will be referred to as a "wall event", as will any other equally steep decrease in n_e.

It is of interest to note that auroral events were found by looking at the bulk of the

[1]The calculated errors associated with these points are discussed in 3.2.1

n_e RTI plots, particularly in the AC pulse measurements. Auroral events are important for this work because they signify a storm. Figure 3.2 shows vertically averaged[2] AC pulse measurements of n_e on a day with auroral activity (top panel) and a day with no significant auroral activity (bottom panel). During auroral events the n_e surges to large irregular values and T_i fluctuates rapidly (Figure A.13), hiding other enhancements. These events do not always take place on a daily basis but when they appear they show up between 4 UT and 17 UT. Beyond events like this and the n_e wall events, n_e followed a predictable daily cycle.

The ion velocity ($\mathbf{V}_i$) along the magnetic field is also displayed in Figure 3.1 (bottom panel). Its value ranges from roughly -30 m/s to 40 m/s. A general increase in $\mathbf{V}_i$ is seen with altitude over the 250 km to 400 km span. However, this parameter is more challenging to interpret and difficult to analyze because it is subject to large uncertainties, as shown by the error bars reported from the analysis of the data. While useful information can still be extracted from the parameter, we will not focus on its behavior in the present thesis.

For reasons that will become clearer in what follows, the dataset was reanalyzed for us by SRI International, using a 5-minute integration time. The 5-minute dataset had data gaps not seen in the 15-minute data because the 15-minute dataset included different PFISR experiments which could not be provided with a smaller integration time. As well, these gaps did not matter for our purposes. It is important, however, to keep both integration bin sizes in mind throughout this work, simply because the 5-minute integrations have more details, feature higher and lower values, but also have typically larger error bars.

In Figure 3.3, an RTI plot of Figure 3.1 is recreated with 5-minute integration bins. Though both figures have the same features, some important differences are worthy of mention. In particular, the structure of the T_i enhancement around 6 UT is affected by the shorter integration time through a more gradual decrease, as can be seen in Figure 3.3 (top panel) after the spike event. This is discussed further in Chapter 4.

The slight T_e enhancement near 6 UT is made more visible in Figure 3.3 (second panel from the top). This enhancement takes place at the lower altitudes, where the temperature increases from about 1900 K to 2100 K around 250 km. In this plot, enhancements like these happen several times at this altitude.

[2]Averaged to reduce the noise introduced through a large bandwidth, see 2.1.1

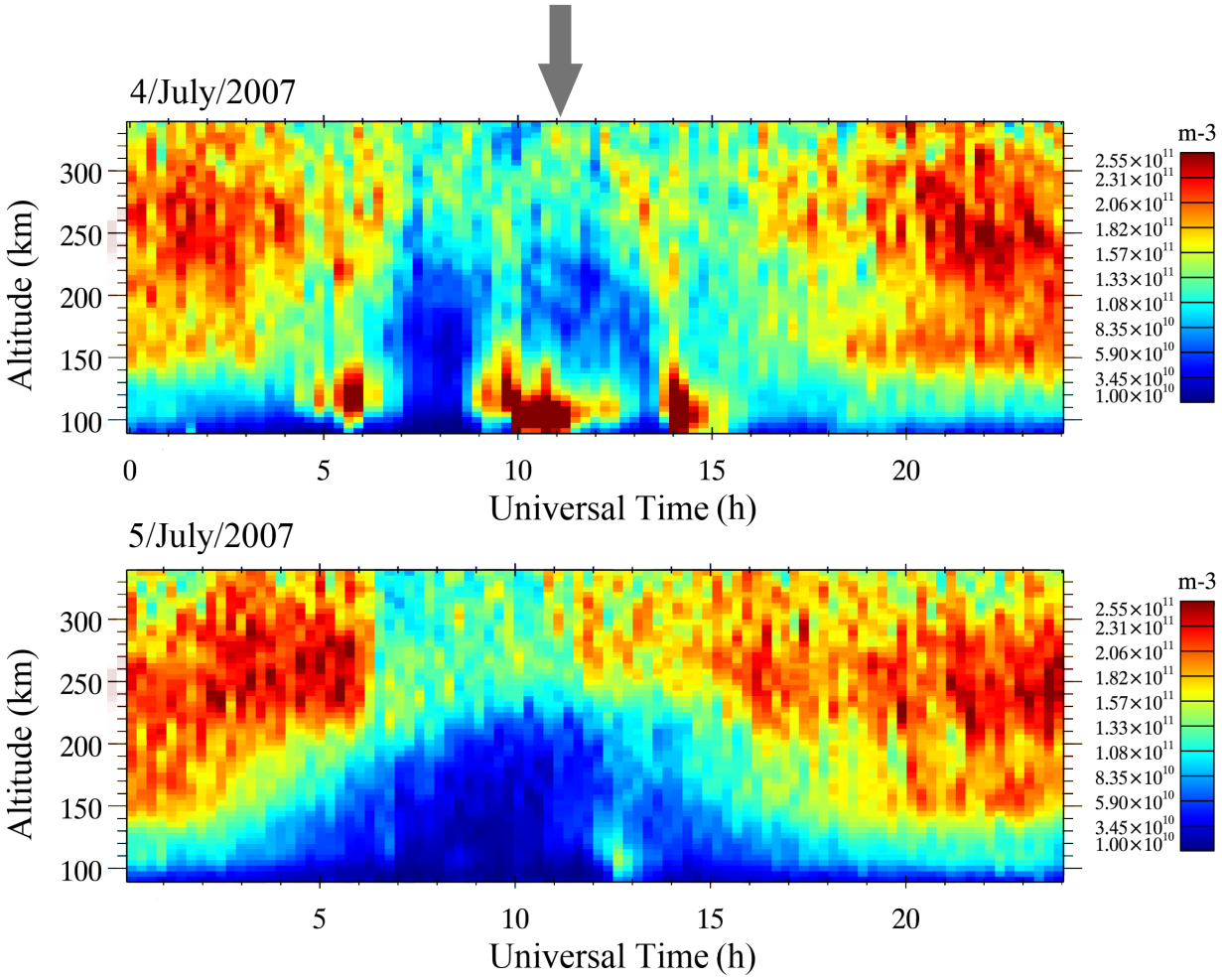

Figure 3.2: RTI plots of n_e with 15-minute integration bins and AC pulse measurements. (Top Panel) 4/July/2007, significant auroral activity. (Bottom Panel) 5/July/2007, low/insignificant auroral activity. The arrow at the top indicates the approximate location of local midnight in Magnetic Local Time (MLT) coordinates (11:20 UT).

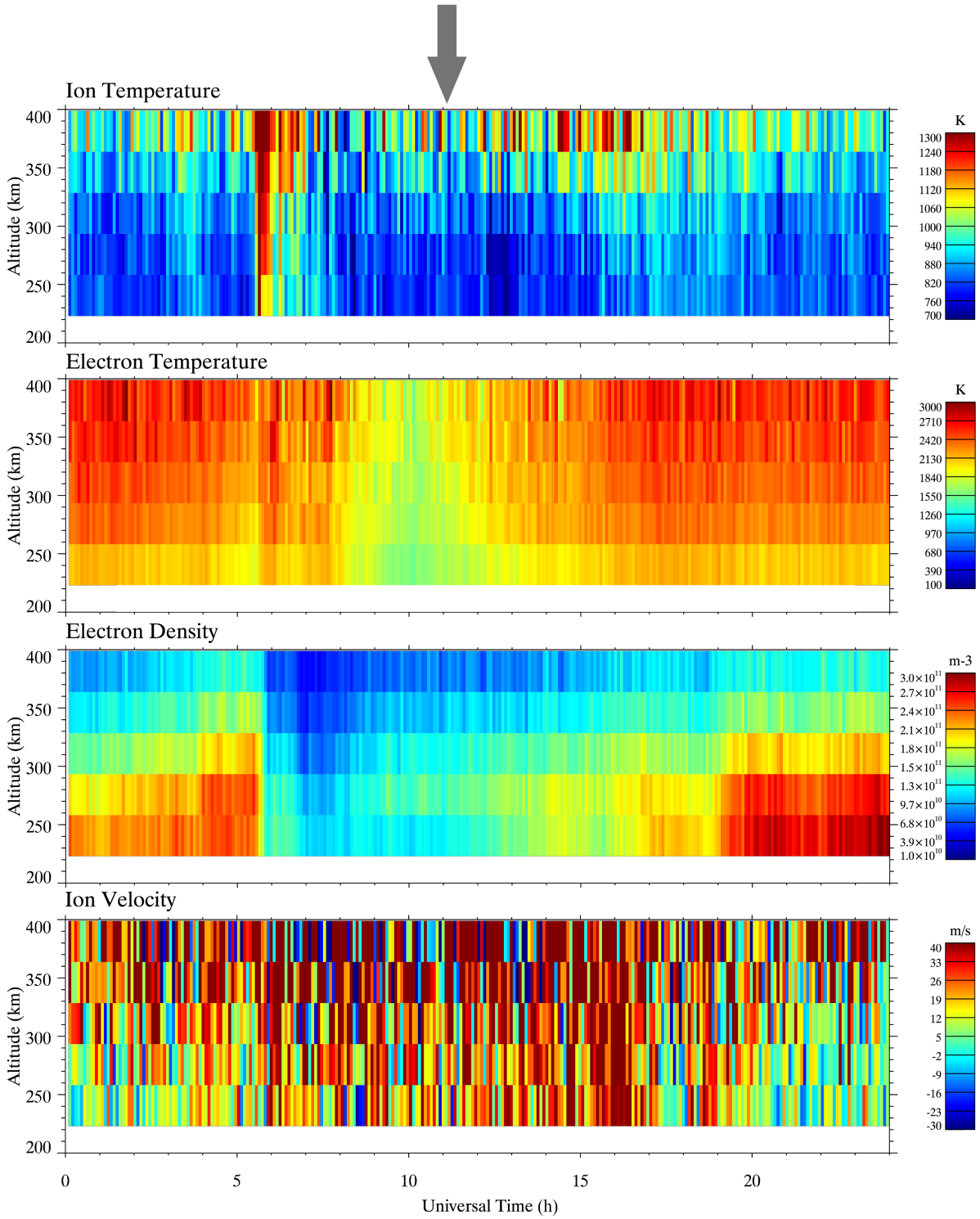

Figure 3.3: Same as Figure 3.1 but with a 5-minute resolution.

To summarize, a steep T_i enhancement appears for 5 to 10 minutes between 200 km and 400 km during the evening. At very near the same time, but not exactly, there is a steep decrease in n_e, while T_e and $\mathbf{V}_i$ remain relatively unaffected. Figure 3.1 and 3.3 only show 27/June/2007, but on every quiet (low geomagnetic activity) evening from 27/June/2007 to 5/July/2007 (every day except 3/July and 4/July) similar T_i enhancements and n_e decreases are seen. It is important to note that these spike events would only be found on quiet days because auroral events and storms would produce erratic variations in T_i and hide the single T_i spike event. As well, these storm events would mask the n_e wall event through auroral ionization.

By examining a year of data from PFISR and isolating steep n_e wall events (of which there were 177), twenty-five T_i spike events were found within 1.5 hours of n_e wall events (all of which are listed in Table 3.1). These T_i spike events are the focus of the present research[3]. Referring to equation 1.14, these T_i enhancements could be the result of a change in T_e, the neutral temperature (T_n), the neutral mass (m_n), the ion-neutral relative drift ($|\mathbf{V}_i - \mathbf{V}_n|$), or conduction of heat from above.

3.1.2 SuperDARN Convection Data

Information about the location of PFISR at the time of the T_i spike events was obtained from convection plots inferred from SuperDARN HF radar data (*Ruohoniemi and Baker*, 1998). By examining these plots, it was found that the T_i spike events were generally seen when PFISR was on or near the evening edge of sunward convection (particularly 28/June/2007, according to modeled convection lines). This involved looking at a full day of convection plots on days with T_i enhancements, as well as the specific times of spikes. Figure 3.4, for example, shows two convection plots taken at the time of a T_i enhancement (27/June/2007 and 28/June/2007).

The important conclusion that can be drawn from examining the SuperDARN convection plots is that at the time of the T_i spike events, these maps mostly indicate that PFISR is in

[3]For other RTI plots between 27/June/2007-5/July/2007, see Appendix A.

Table 3.1: T_i spike events located within 1.5 hours after an n_e wall event from 1/March/2007 to 29/February/2008.

Year	Month	Day	Within ± 1h?	Within ± 30min?	Spike time (UT)	Kp Index
2007	3	26	Yes	No	6.3	1.3
2007	3	27	No	No	6.3	2.7
2007	4	19	No	No	7.1	1.3
2007	5	1	Yes	Yes	4.8	2.7
2007	5	3	Yes	Yes	6.8	1.3
2007	5	19	No	No	6.4	3
2007	5	27	Yes	Yes	5.4	2
2007	6	8	Yes	Yes	4.4	2
2007	6	15	Yes	Yes	5.8	2.7
2007	6	21	Yes	Yes	6.4	1.7
2007	6	27	Yes	Yes	5.6	1.7
2007	6	29	No	No	9.9	1
2007	6	30	Yes	No	4.4	1.7
2007	7	1	Yes	Yes	7.9	1
2007	7	5	Yes	Yes	6.3	1.7
2007	8	1	Yes	Yes	5.5	2.7
2007	8	2	Yes	Yes	5.7	1
2007	8	3	Yes	Yes	5.7	1.3
2007	8	6	Yes	No	8.9	1.7
2007	9	2	Yes	Yes	3.7	4.7
2007	9	8	No	No	7.3	2
2007	10	26	Yes	No	4.0	2.7
2007	11	23	Yes	Yes	7.1	3
2007	12	18	Yes	Yes	5.6	3.7
2008	1	6	Yes	Yes	3.4	3.7

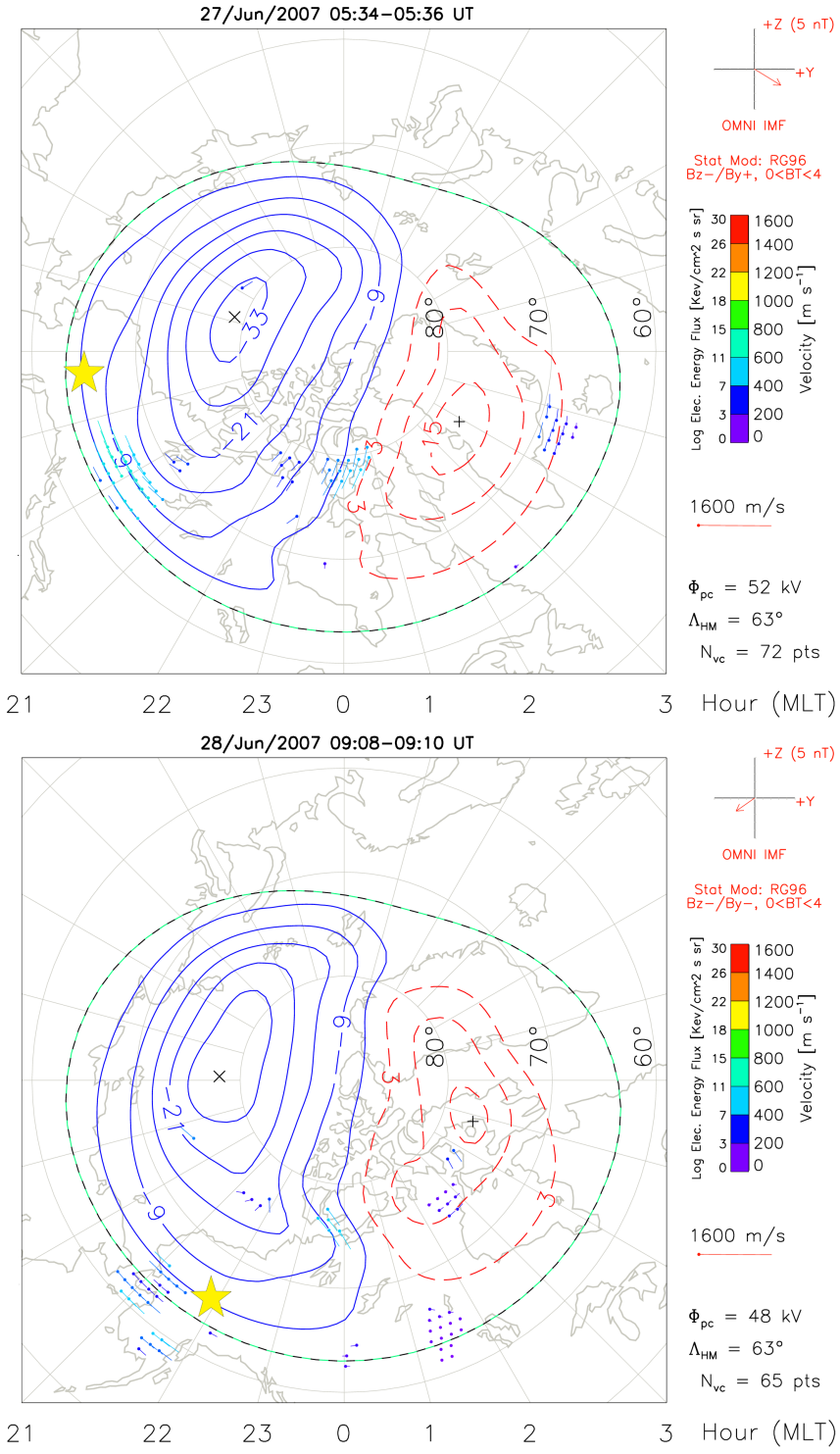

Figure 3.4: SuperDARN potential maps at the time of a T_i enhancement. The gold star indicates PFISRs location, while the red and blue circles relate to potential (Left Panel) 27/June/2007 (Right Panel) 28/June/2007.

the evening sector near the inferred equatorward edge of the sunward ion convection pattern. As well, these plots place ensuing data points in the ion convection pattern. This information means that a mechanism associated with the dusk-side convection pattern is responsible for the T_i spike events.

3.2 T_i Enhancements and Decreases in n_e

The clearest correlation seen in the raw data is between the T_i enhancements and the steep n_e depletions. That being the case, it is beneficial to examine the PFISR dataset more carefully to infer why these n_e wall events are occurring in the same region as the T_i spike events.

3.2.1 T_i and n_e at 275 km

The correlations between T_i (Figure 3.5, top panel) and n_e (Figure 3.5, bottom panel) were examined as functions of UT for several days at 275 km, a central F-region altitude with a high signal to noise ratio. These plots describe daily T_i spike events (enhancements ranging from roughly 150 K to 400 K above the background) occurring in the evening between 27/June/2007 and 5/July/2007. Except for 4/July, these were geomagnetically quiet days with a K_p index below 2 (spike events are indicated with dashed lines). A simultaneous plot of the n_e at the same altitude (Figure 3.5, bottom panel) shows that during the quiet days T_i enhancements were accompanied by steep decreases in n_e (depletions by factors of two or more, n_e wall events). As argued below, these n_e wall events indicate that the radar started observing plasma that had emerged from the night-side.

Beyond exploring the relationship between T_i and n_e, Figure 3.5 also gives insight into the calculated errors associated with these parameters. The red lines seen in these plots are the calculated errors for T_i and n_e multiplied by 10 in order to see finer structures. Given that the error is always much smaller than the parameter, these plots create a strong argument for validity of the data and reinforce that these T_i spike events are not artifacts.

The T_i and n_e data were reanalyzed with a 5-minute integration period and the plots in Figure 3.5 were recreated in Figure 3.6. As compared to the 15-minute integration period, the 5-minute integration period shows higher T_i spikes (ranges from 250 K to 800 K above the

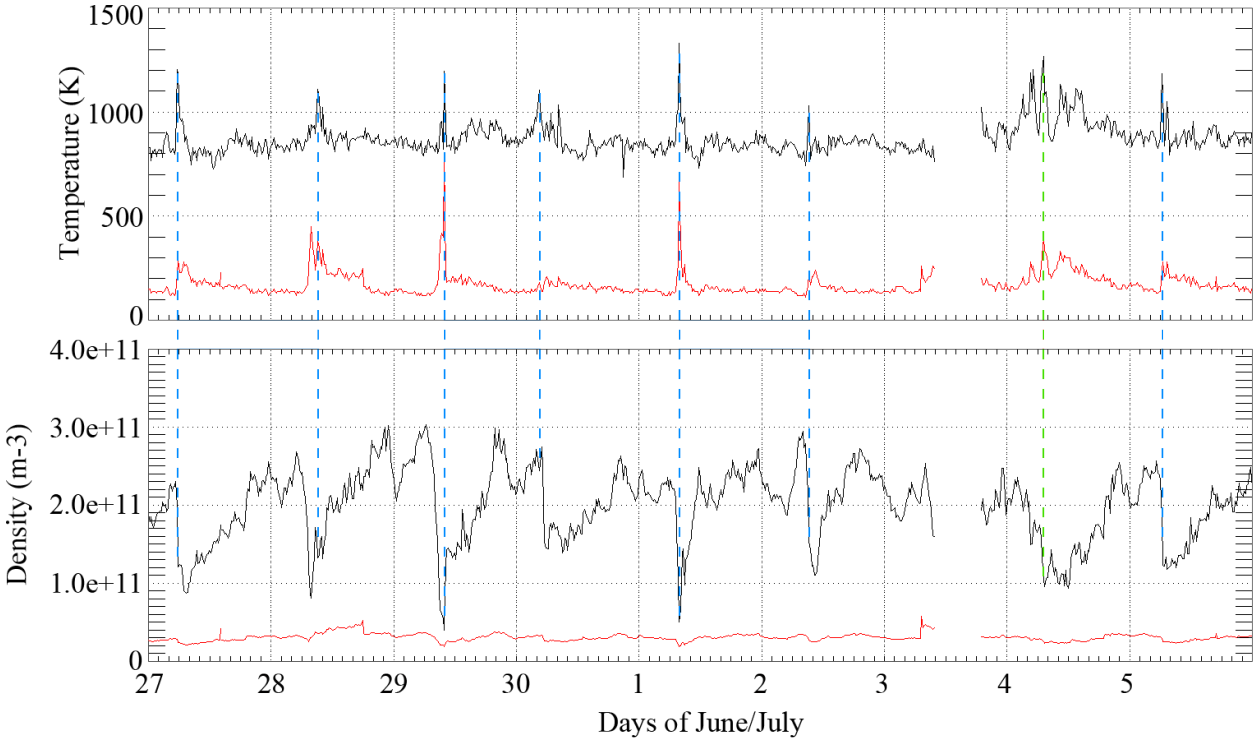

Figure 3.5: 15-minute integration data from PFISR. (Top Panel) T_i at 275 km from 27/June/2007 to 5/July/2007 as a function of UT. (Bottom Panel) Corresponding n_e at 275 km. The red lines indicate the parameter error multiplied by 10. Dashed lines indicate the time of the T_i enhancement (the green line was on a day of high geomagnetic activity, so declaring a spike event would be misleading).

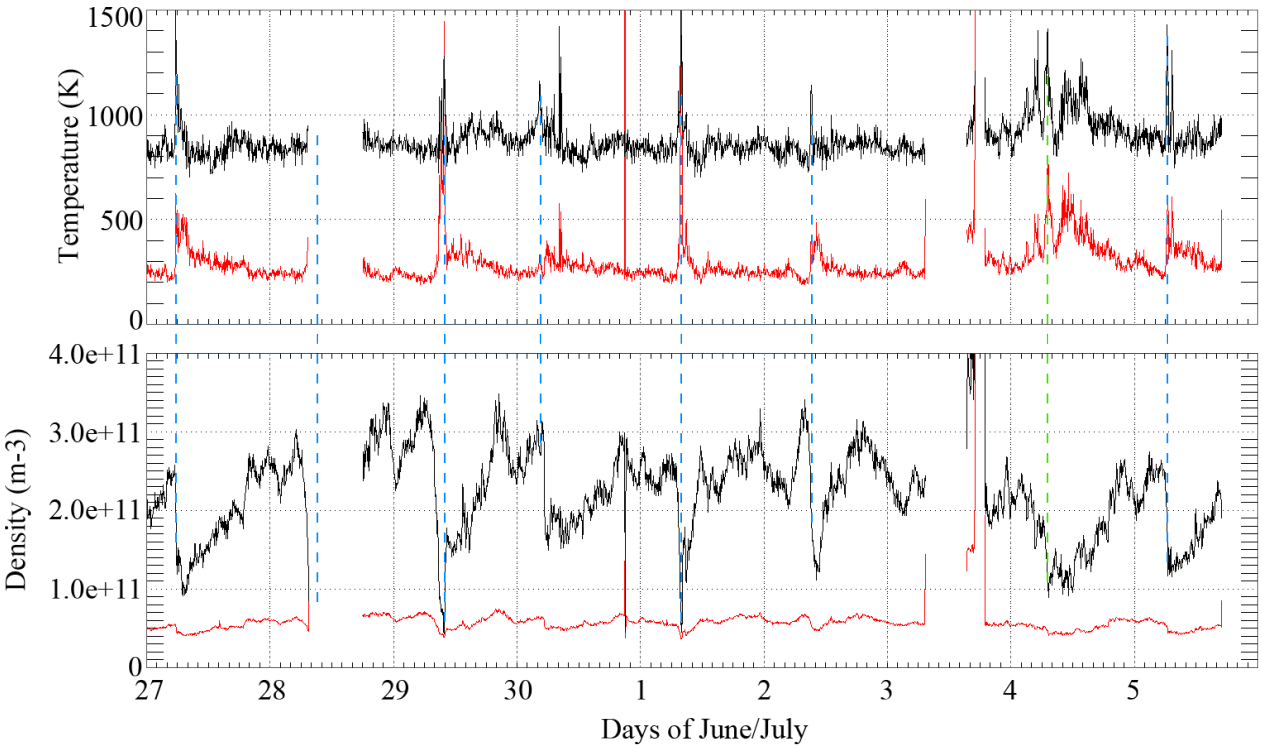

Figure 3.6: Same as Figure 3.5, but with 5-minute integration bins. Note that the dashed lines indicate the enhancements found with the 15-minute integrations.

background, with T_i being roughly 200 K greater than the 15-minute integration T_i during the spike event), similar n_e wall events, and otherwise noisier data in general, as expected from a shorter integration time.

The 5-minute integration period plots show sub-structures in the T_i spike events and n_e wall events that could not be seen in the 15-minute integration period plots. The results showed that in spite of added noise, the T_i peaks had a tendency to rise at a faster rate, were showing added structure, and had sharper peaks (by up to 150K) than seen through the 15-minute integration time used to produce Figure 3.5. The 30 to 45 minute event duration was not affected. As well, the correlation between the T_i spike events and n_e wall events remains clear. Lastly, the error lines continue to show that these spikes in T_i are not artifacts.

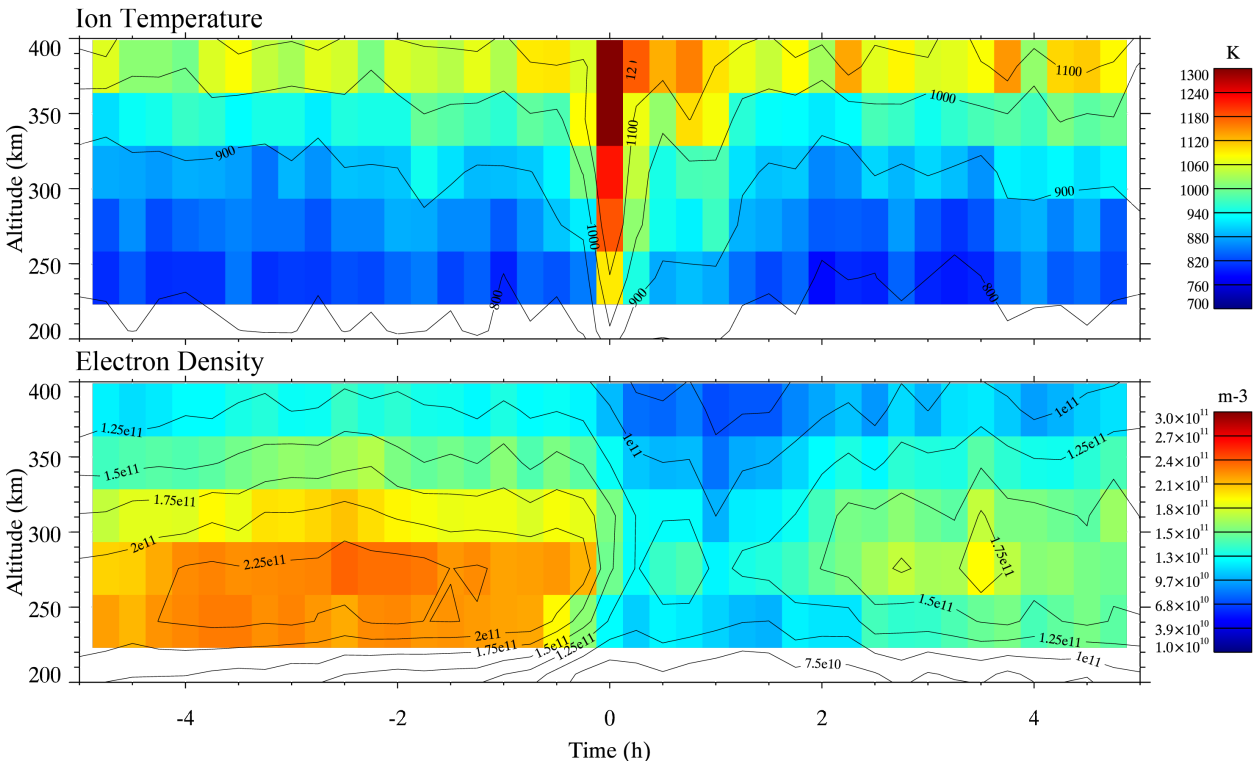

Figure 3.7: Epoch studies of 15-minute integration bin data with the T_i spike events at time zero. Period covered: 27/June/2007 to 5/July/2007 (seven spikes). (Top Panel) T_i. (Bottom Panel) n_e.

3.2.2 T_i Enhancements and Steep Decreases in n_e in the Context of Epoch Studies

An epoch study of the various plasma parameters of interest proved to be quite beneficial in order to highlight the general trends of other parameters and calculations before, after and during a T_i enhancement. To this end, a series of epoch studies were performed.

T_i and n_e Epoch Studies for Spike Events from 27/June/2007 to 5/July/2007 (15-Minute Integration Bins)

An epoch study of 15-minute integration period data was performed by using the T_i spike events for $t = 0$ (referred to as time zero) for quiet days between 27/June/2007 and 5/July/2007, inclusively (Figure 3.7, top panel). Time zero was picked at the T_i maximum and a median value for each time and altitude bin was recorded.

The T_i epoch study shows enhancements from 800 K to 1100 K near 250 km, and 1000 K to 1300 K at higher altitudes. We note first that the T_i enhancements increase more rapidly than they decrease. In fact, there appears to be a double structure of the T_i parameter within two hours after time zero, followed by other structures (emphasized by the contour lines). This suggests that on average, or at least on a few occasions, the mechanism causing these enhancements turned off or weakened after an initial peak in the spike event, only to then increase and then disappear. The T_i epoch study also shows an increase in T_i with altitude within the enhancement, changing from roughly 1100 K at 250 km to 1300 K at 400 km.

With all the T_i spike event times aligned, median values of the n_e were also found (Figure 3.7, bottom panel), showing steep decreases from roughly 2.0×10^{11} m^{-3} to 8.0×10^{10} m^{-3} near 250 km and 1.0×10^{11} m^{-3} to 4.0×10^{10} m^{-3} higher up (n_e wall event). The epoch study also shows that the n_e wall event began, on average, slightly before the enhancement in T_i.

T_i and n_e Epoch Studies for Spike Events from 27/June/2007 to 5/July/2007 (5-Minute Integration Bins)

To have a closer look at the data near $t = 0$, our epoch study was repeated using data based on 5-minute integration bins, available for only 27/June/2007 to 5/July/2007 (seen in Figure 3.8). The most important result from this study was that the 5-minute integration periods show larger spike temperatures and a more rapid evolution around $t = 0$ than the 15-minute bins, for T_i and n_e. The rest of the data was noisy, as expected from the larger uncertainties and/or variations associated with a smaller integration time.

In the 5-minute T_i epoch study, the temperature enhancements were more clearly defined while the gradual decrease was considerably steeper. In fact, instead of a gradual decrease, there are two defined spikes with some slight enhancements occurring around them, the first one occurring at time zero, and the second, much smaller, spike occurring roughly 50 minutes after the spike. At 250 km, the first spike is well defined and is an enhancement above the background of about 500 K (going from roughly 800 K to 1300 K), while the second is less defined and is roughly 200 K above the background (approximately 800 K to 1000 K). At higher altitudes, the first spike is about 500 K above the background (going from roughly 1000 K to 1500 K), the second is less defined and is roughly 200 K above the background

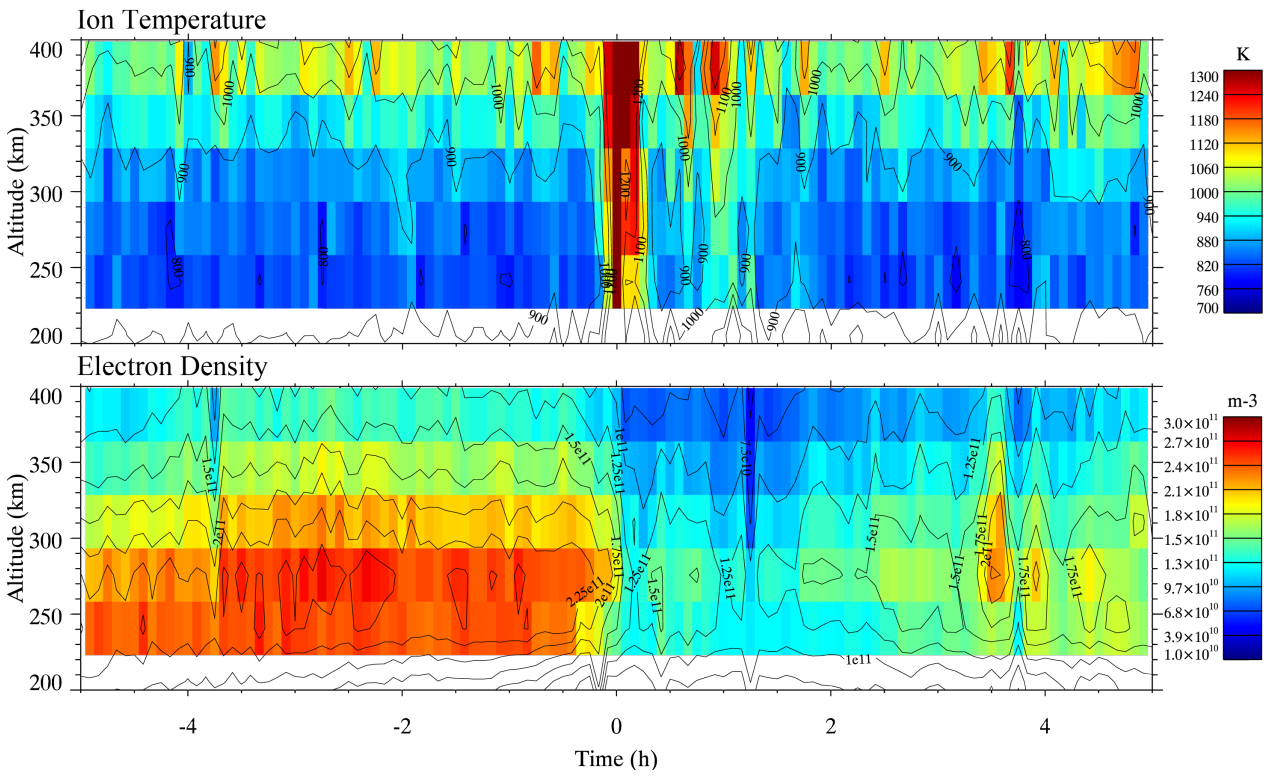

Figure 3.8: Same as Figure 3.7, but with 5-minute integration bins and not including 28/June/2007 (missing data) and 30/July/2007 (spike time is questionable).

(approximately 1000 K to 1200 K). Clearly, the first is the initial spike associated with the 15-minute integration, the spike event, while the second spike and the enhancements seen around it are the result of other spikes, resolvable with the 5-minute data. In short, the spike seen in the 15-minute integration appears to be multiple spikes in the 5-minute integration data, but there is no way to tell if a shorter integration time would have revealed even more.

The 5-minute epoch study for the n_e shows a decrease in density going from roughly 2.6×10^{11} m^{-3} to 1.3×10^{11} m^{-3} near 250 km, and 1.0×10^{11} m^{-3} to 7.0×10^{10} m^{-3} higher up. It is also interesting to note that for the higher resolution, the n_e wall event takes place a little earlier when compared to the 15-minute integration bin epoch study.

T_i and n_e Epoch Studies for Spike Events from 1/March/2007 to 29/February/2008 (15-Minute Integration Bins)

By gathering a larger sample of spike events, features introduced by seasonal bias and anomalies are reduced. For this reason, our epoch study was repeated for the twenty-five T_i enhancements found within 1.5 hours of an n_e wall event.

In the epoch study of twenty-five T_i enhancements (Figure 3.9, top panel), the spike event appears slightly thicker than in the study with only 7 spikes. However, T_i is still enhanced more rapidly than it decreases and we also see roughly the same enhancements in T_i, increasing by roughly 300 K above the background near 250 km (approximately 800 K to 1100 K) and 400 K higher up (1000 K to 1400 K). As seen before, T_i increases with altitude within the enhancement (roughly 400 K), as well, a double hump appears again, along with tailing structures.

In the epoch study of n_e that uses twenty-five T_i spike events (Figure 3.9, bottom panel), a decrease of about a factor of two is seen, just like before. Similar decreases are also seen. Near 250 km the density changed from roughly 1.4×10^{11} m^{-3} to 6.0×10^{10} m^{-3}, while higher up the density was changed from roughly 1.2×10^{11} m^{-3} to 5.5×10^{10} m^{-3}. Once again, n_e depletes slightly ahead of the T_i spike events

It is important to note that even though the time from 27/June/2007 to 5/July/2007 is the focus here (because that was the only time period where 5-minute integration bins were readily available), the same general trends can be seen in the 15-minute integration bin epoch

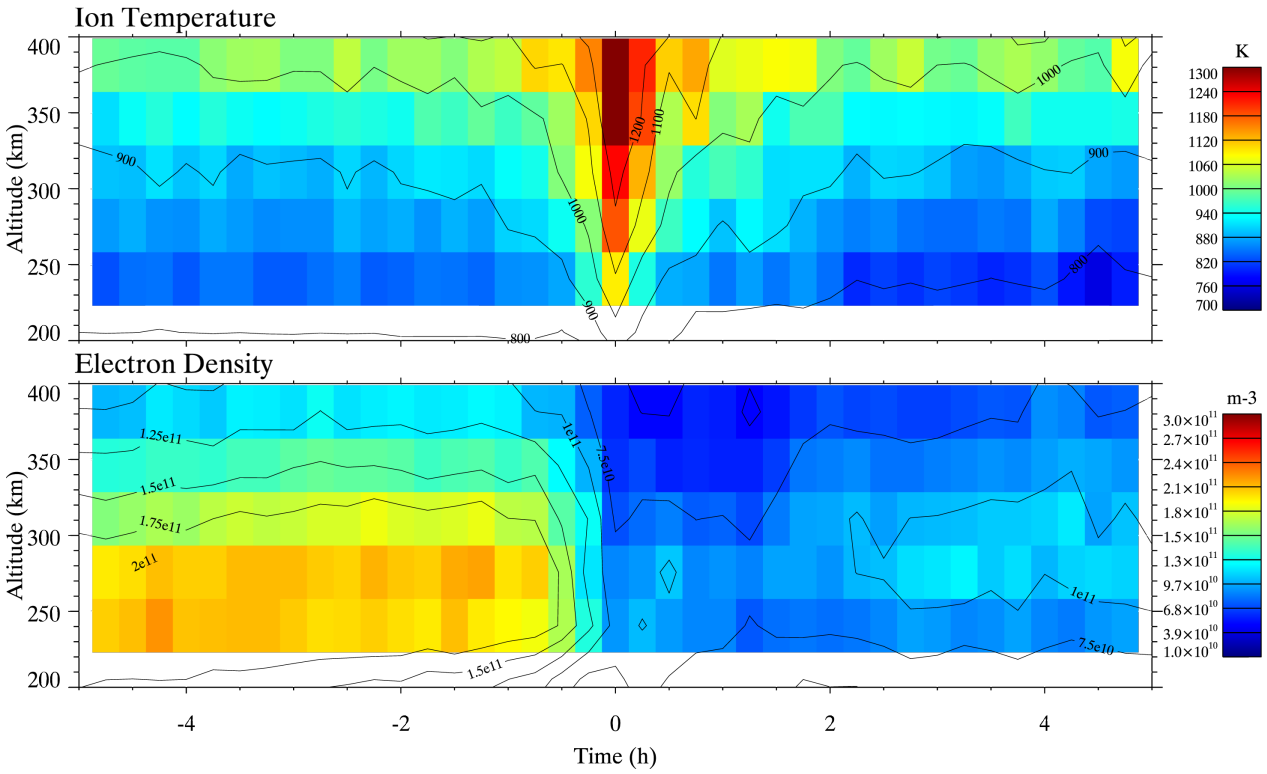

Figure 3.9: Epoch studies of 15-minute integration bin data with all twenty-five T_i spike events within 1.5 hours of an n_e wall event at time zero. Period covered: 1/March/2007 to 29/February/2008. (Top Panel) T_i. (Bottom Panel) n_e.

studies when all twenty-five spike events within 1.5 hours of an n_e wall event are used. This study reaffirmed such things as: the intensity of the T_i enhancement, the quick increase and slower decline in T_i, the temperature increase with altitude seen within the T_i spike event, the double hump in T_i, the span of the n_e wall event, and the intensity of the decrease in n_e.

Since more events were present in this epoch study, it was beneficial to examine the 25% and 75% envelopes to estimate the deviations from the median epoch study. This entailed taking values that fell in a given time and altitude bin, and finding the percentiles rather than a median. A study like this is less useful when performed with just the spike events occurring between 27/June/2007 to 5/July/2007 because there are not as many values falling into given time-altitude bins. For this reason, only the epoch studies involving twenty-five events feature envelope calculations.

In the 25% epoch study of T_i (Figure 3.10, top panel) we see the spike with minor features afterwards, while the 75% epoch study (Figure 3.10, bottom panel) contains more features around $t = 0$, obscuring the spike event slightly. In the 25% epoch study of n_e (Figure 3.11, top panel) the wall event occurs earlier than in the median epoch study, while the n_e wall event for the 75% epoch study (Figure 3.11, bottom panel) occurs at the same time as the median epoch study wall event. This earlier wall event may be the result of examining lower densities and could be related to a bias towards winter conditions, which have naturally smaller plasma densities than other points in the year.

3.2.3 The Significance of the Steep n_e Wall Event

Unless there is evidence of auroral precipitation, photoionization is responsible for the plasma (n_e) density. The absence of photionization creates a plasma depletion on a time scale associated with recombination chemistry. However, it is important to recall that ion production increases as the solar zenith angle decreases. During summer at dusk, there is therefore some photo-production left.

One way to understand the significance of the n_e wall event is to consider it in terms of the convection pattern and the position of PFISR at the time of the wall event, the evening sector. The plasma observed before the T_i spikes and the n_e wall events was moving in the corotation region of the F-region ionosphere, a region of antisunward motion. As the plasma

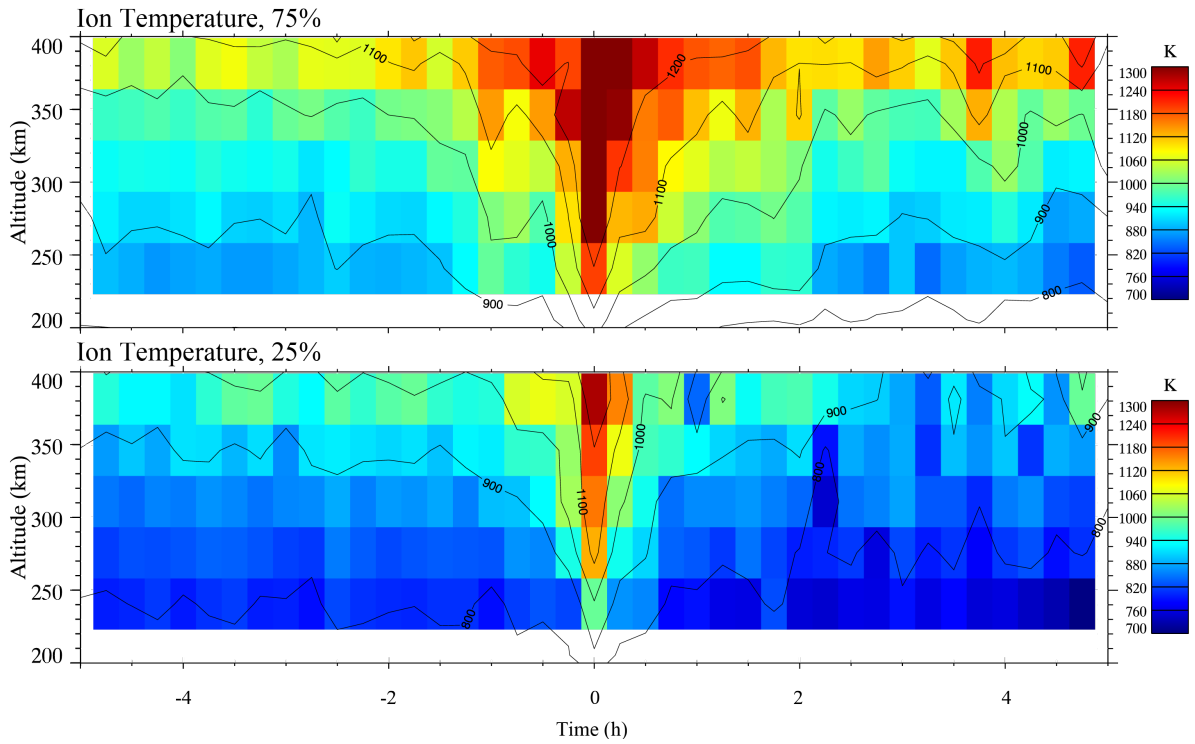

Figure 3.10: Epoch studies of 15-minute integration bin data with all twenty-five T_i spike events within 1.5 hours of an n_e wall event at time zero. Period covered: 1/March/2007 to 29/February/2008. (Top Panel) 75 percentile of T_i. (Bottom Panel) 25 percentile of T_i.

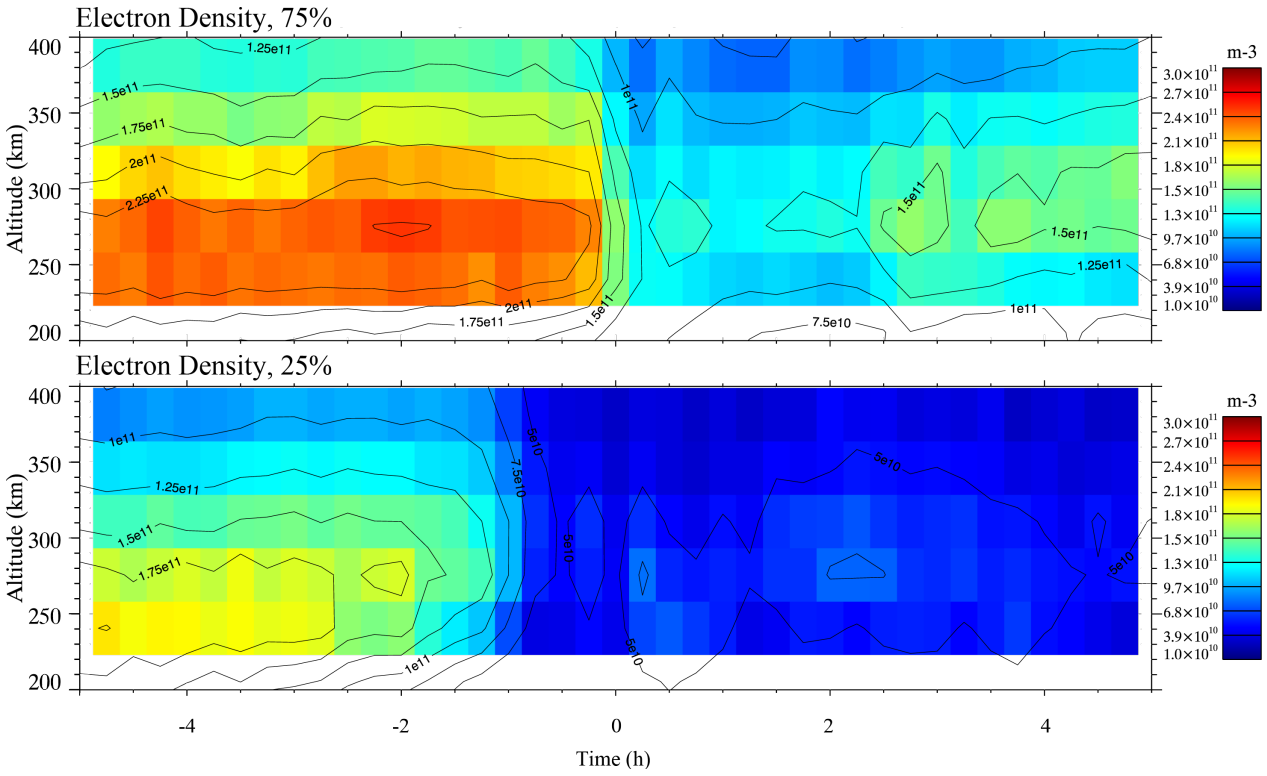

Figure 3.11: Epoch studies of 15-minute integration bin data with all twenty-five T_i spike events within 1.5 hours of an n_e wall event at time zero. Period covered: 1/March/2007 to 29/February/2008. (Top Panel) 75 percentile of n_e. (Bottom Panel) 25 percentile of n_e.

moved along in the region it would move to higher solar zenith angles and, therefore, regions with a smaller photoionization rate. However, plasma that was observed by PFISR after the time of the n_e wall event was nightside plasma moving sunward, as indicated by the decrease in plasma density.

There are two ways that plasma could move to regions of large solar zenith angles (nighttime conditions). The first calls for plasma to be convected over the polar cap and then be moved into low latitude regions with no sunlight. Afterwards the plasma would move towards regions of lower solar zenith angles and into the dusk sector. The other possibility is that the convection pattern grew, forcing plasma that was corotating at high solar zenith angles to get caught in a region of sunward convection. This possibility calls for sunward convection to take place before the F-region plasma density drop.

Regardless of how n_e became depleted, it is clear that PFISR observed corotating plasma, then a depleted plasma. This means that the n_e wall is a signature of the boundary between these two plasmas of different history, as well as an indicator of the high latitude convection boundary (the plasmapause). It is therefore important to include this n_e wall event into the definition of what makes an increase in T_i a "spike" because, not only does this decrease accompany the largest T_i spikes occurring from 27/June/2007 to 5/July/2007, it ensures that we are consistently examining the same type of event.

3.3 Model Studies of Plasma Convection, n_e, and Neutral Winds

In order to put the observations into context, we examined results from the Coupled Thermosphere Ionosphere Plasmasphere electrodynamics (CTIPe) (*Fuller-Rowell et al.*, 2008) model showing plasma density and convection (Figure 3.12, left panel) and neutral flow and temperature (Figure 3.12, right panel) at 300 km for a $K_p \approx 3$ (higher than our subset of days) during equinox conditions. The CTIPe model indicates that a plasma density depletion is present in the region where sunward convection of nightside plasma picks up on the evening side, starting at the boundary of sunward convection. This feature is consistent with the n_e parameter and location identified by SuperDARN, and shows that the T_i enhancement and

sudden decrease in n_e can go hand-in-hand with the evening sunward convection boundary.

Turning to the neutral model, Figure 3.12 shows that even though neutrals are generally accelerated by ions through ion drag (momentum transfer collisions between ions and neutral particles), there are still differences in their motions. These differences come from several sources (*Killeen et al.*, 1984). For example, a sunward pressure gradient brought on by solar radiation heating the sub-solar point more than other regions, brings air expansion and increases the atmospheric pressure, forcing neutral gases antisunward (*King and Kohl*, 1965). As well, the Coriolis force creates a general clockwise rotation of neutral winds (*Fuller-Rowell et al.*, 1984, 2008). The result of these mechanisms is a strong clockwise vortex of neutrals in the dusk sector by contrast with a motion that remains far more antisunward, without a vortex, in the morning sector. The result of these processes on the neutral wind is apparent in Figure 3.12.

In particular, Figure 3.12 illustrates that near the region where T_i is enhanced, the neutral flow reverses in the same way and direction as the plasma flow. A comparison of the plasma and neutral model, indicates that the evening side neutrals tend to undergo sunward acceleration poleward of the plasma reversal. This means that the plasma and neutral flows probably do not always move in the same direction just at the convection reversal. This means that there could be a narrow region in the evening sector where $|\mathbf{V}_i - \mathbf{V}_n|$ might peak. We note that this region is roughly the same as where the T_i enhancements and n_e wall events are observed.

It is also of note that according to the model calculations, in the region where T_i is enhanced, T_n is decreasing in relation to the rotation of the Earth. In other words, as the Earth rotates, PFISR would be in a region of high T_n in the afternoon and low T_n in the early morning (Figure 3.12, left panel). This is important to keep in mind since a T_n increase could enhance T_i through heat exchange. In other words, according to equation 1.14 we could have, in the absence of any other contribution from relative drifts:

$$\left(1 + \frac{m_i + m_n}{m_i}\frac{\nu_{ie}}{\nu_{in}}\right)(T_{i\text{final}} - T_{i\text{initial}}) \approx T_{n\text{final}} - T_{n\text{initial}} \tag{3.1}$$

This means that in order to create a T_i enhancement of 300 K at 250 km in the evening ($\nu_{in} \approx 0.4$ 1/s, $\nu_{ie} = 0.004$ 1/s) by T_n alone, a similar increase of 300 K in T_n would be

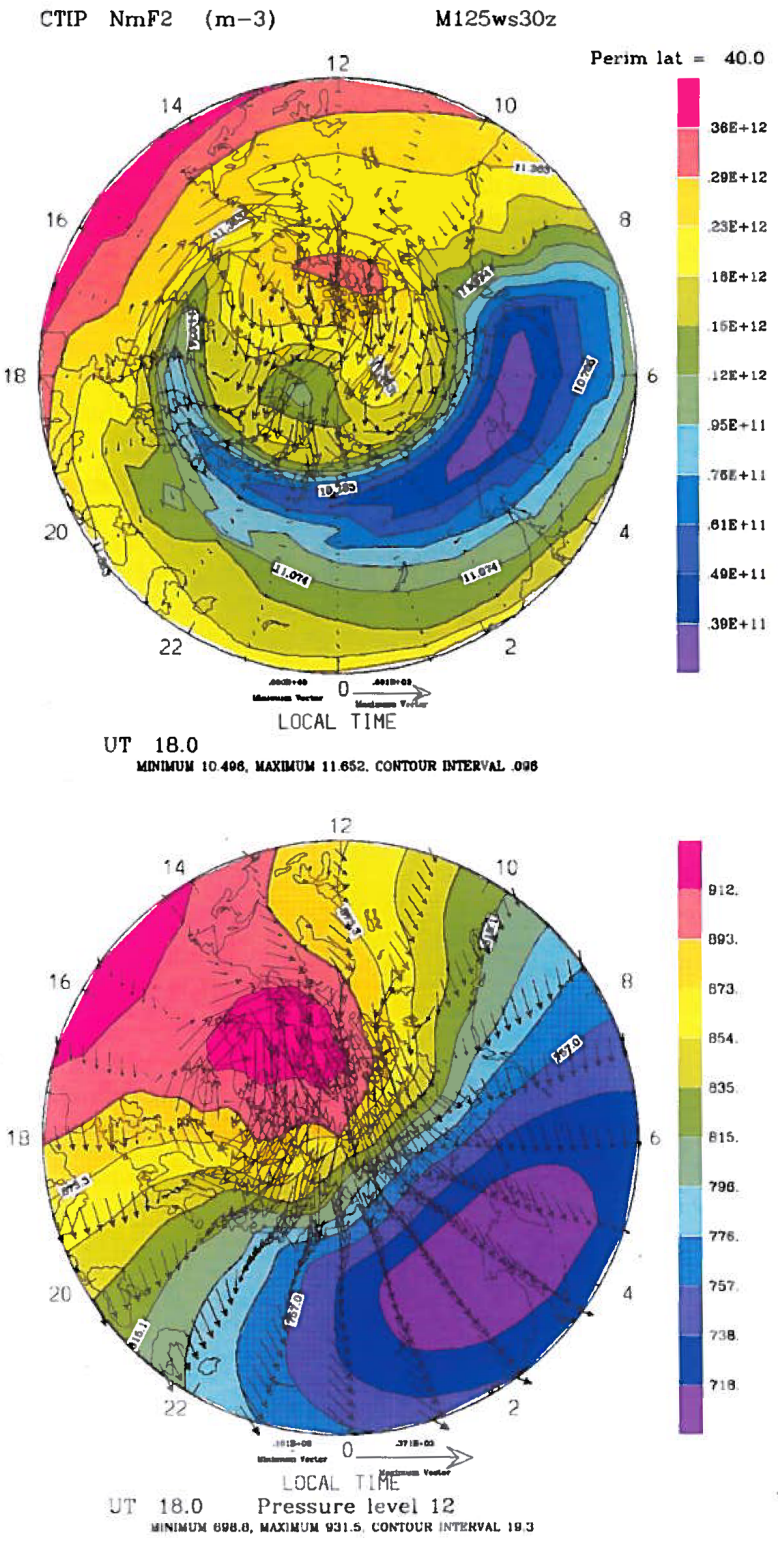

Figure 3.12: CTIPe model at 300 km altitude poleward of 40° latitude, during a $K_p \approx 3$ (*Fuller-Rowell et al.*, 2008). (Left Panel) Plasma convection is shown with arrows and plasma density is shown in colour. (Right Panel) Arrows show neutral wind and colour shows T_n.

needed. According to various models and observations, this spike is unlikely to happen, never mind on a daily basis. As well, referring back to Chapter 1, T_n is affected mostly by photoionization, a long term effect. It would not be the reason for a sudden T_n spike in the evening sector, especially a spike on the order of minutes. Even if small-scale structures and local neutral heating models were to be considered (*Chang and St.-Maurice*, 1991; *Fuller-Rowell*, 1984; *St-Maurice and Schunk*, 1981), there is no experimental evidence or theoretical reason for there to be such a T_n enhancement occurring on a small spatial scale at this time or in this region.

From Chapter 1 we know that m_n could also increase T_i, potentially on a shorter and more sudden time scale than T_n. For example, an ion upwelling driving a neutral density enhancement could also bring about a T_i increase (*Sadler et al.*, 2012). However, there is no evidence for a re-occurring sudden m_n increase in narrow sections of the F-region, especially regions of depleted plasma (*St-Maurice and Schunk*, 1981). Furthermore, this would require a Joule heating spike, which would mean an increase in $|\mathbf{V}_i - \mathbf{V}_n|$ to start with. As we are about to show, this latter contribution is a more direct and far more likely driver of a T_i enhancement.

3.4 Electron Temperature

In an earlier section, epoch studies of T_i and n_e were shown. The same analysis was performed on T_e (Figure 3.13) to find any possible relationship between T_i and T_e. Since time zero is always in the evening, dusk photoionization processes in the high latitude F-region become apparent in this epoch analysis. However, because there is no clear enhancement or depletion at time zero, T_e shows no correlation with the T_i spike event.

The analysis was repeated for the 5-minute integration bins. In this study there is a notable T_e spike and decrease region occurring for roughly one to two hours in the 5-minute integration bin epoch study (Figure 3.14). Right after time zero, the temperature jumps up by roughly 200 K near 200 km (from about 1700 K to 1900 K). This is an interesting result because it was not noticeable in the 15-minute integration period data. This enhancement, however, comes from one day creating a bias in the data (27/June/2007, Figure 3.3). So, in

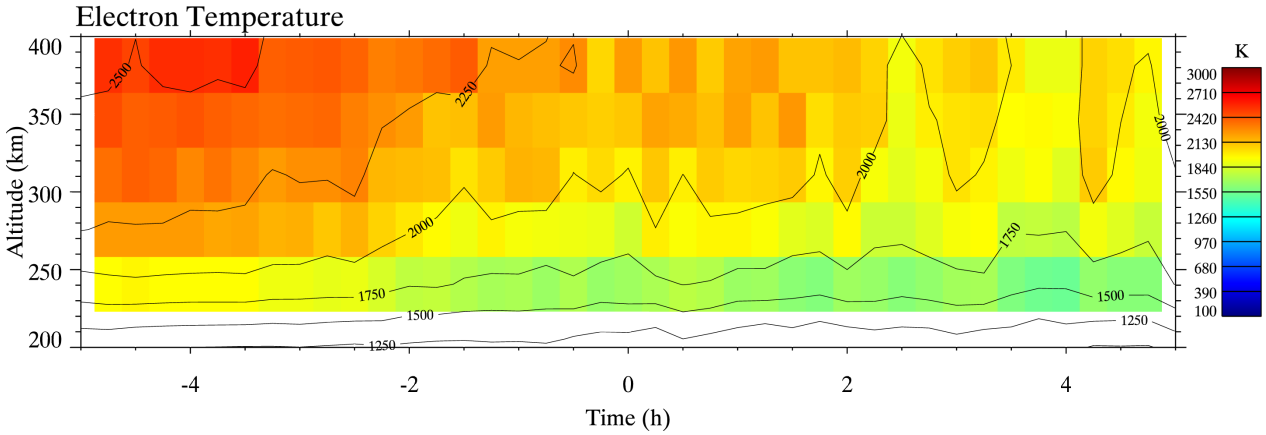

Figure 3.13: T_e epoch study of 15-minute integration bin data with the T_i spike events at time zero. Period covered: 27/June/2007 to 5/July/2007 (seven spikes).

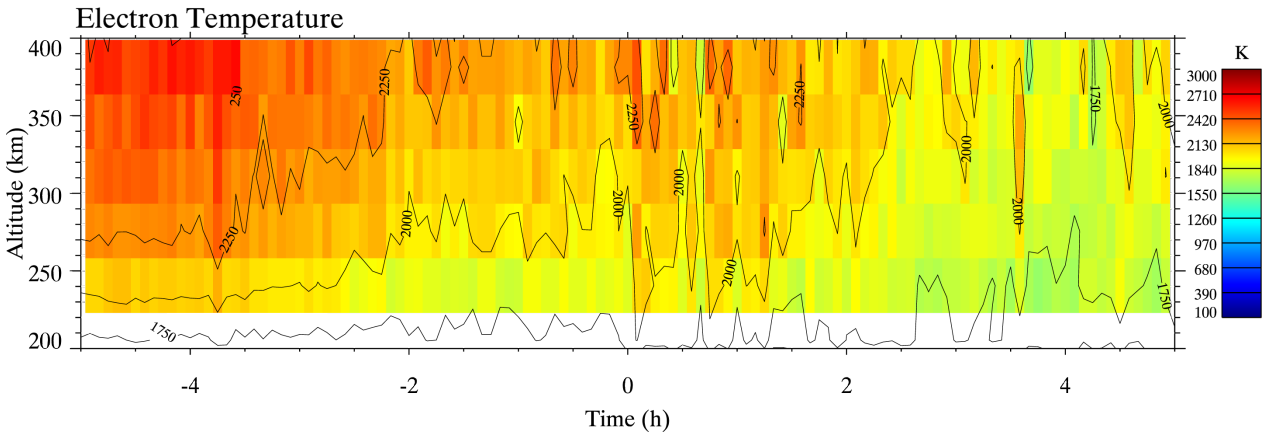

Figure 3.14: Same as Figure 3.13, but with 5-minute integration bins and not including 28/June/2007 (missing data) and 30/July/2007 (spike time is questionable).

relation to the T_i enhancement, T_e is not the cause of the spike event.

A final T_e epoch study was performed in which all twenty-five spike events within 1.5 hours of an n_e wall event were used (Figure 3.15). In this study, the only trends seen are those associated with photoionization, which were discussed earlier. The 25% and 75% epoch studies of T_e (Figure 3.16) also reveal photoionization trends and show no strong correlation with the T_i spike event.

The epochs studies of T_e prove that T_e is not responsible for the increase in T_i. If we had T_e as the cause of the T_i spike event, the resulting equation to find T_e would be:

$$\frac{\nu_{in} m_i \left(T_{i\text{final}} - T_{i\text{initial}}\right)}{\nu_{ie}(m_i + m_n)} \left(1 + \frac{m_i + m_n}{m_i} \frac{\nu_{ie}}{\nu_{in}}\right) \approx \left(T_{e\text{final}} - T_{e\text{initial}}\right) \tag{3.2}$$

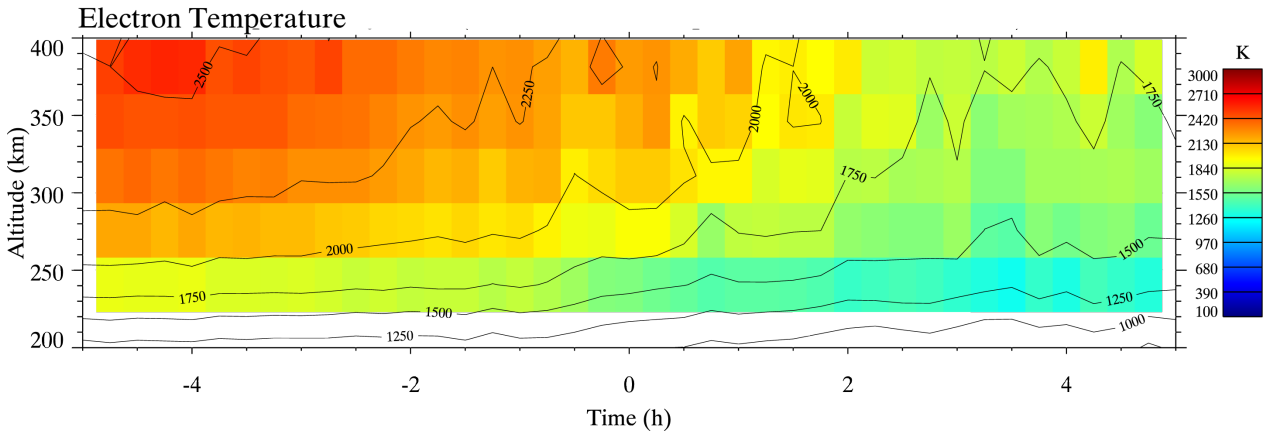

Figure 3.15: T_e epoch study of 15-minute integration bin data with all twenty-five T_i spike events within 1.5 hours of an n_e wall event at time zero. Period covered: 27/June/2007 to 5/July/2007 (seven spikes).

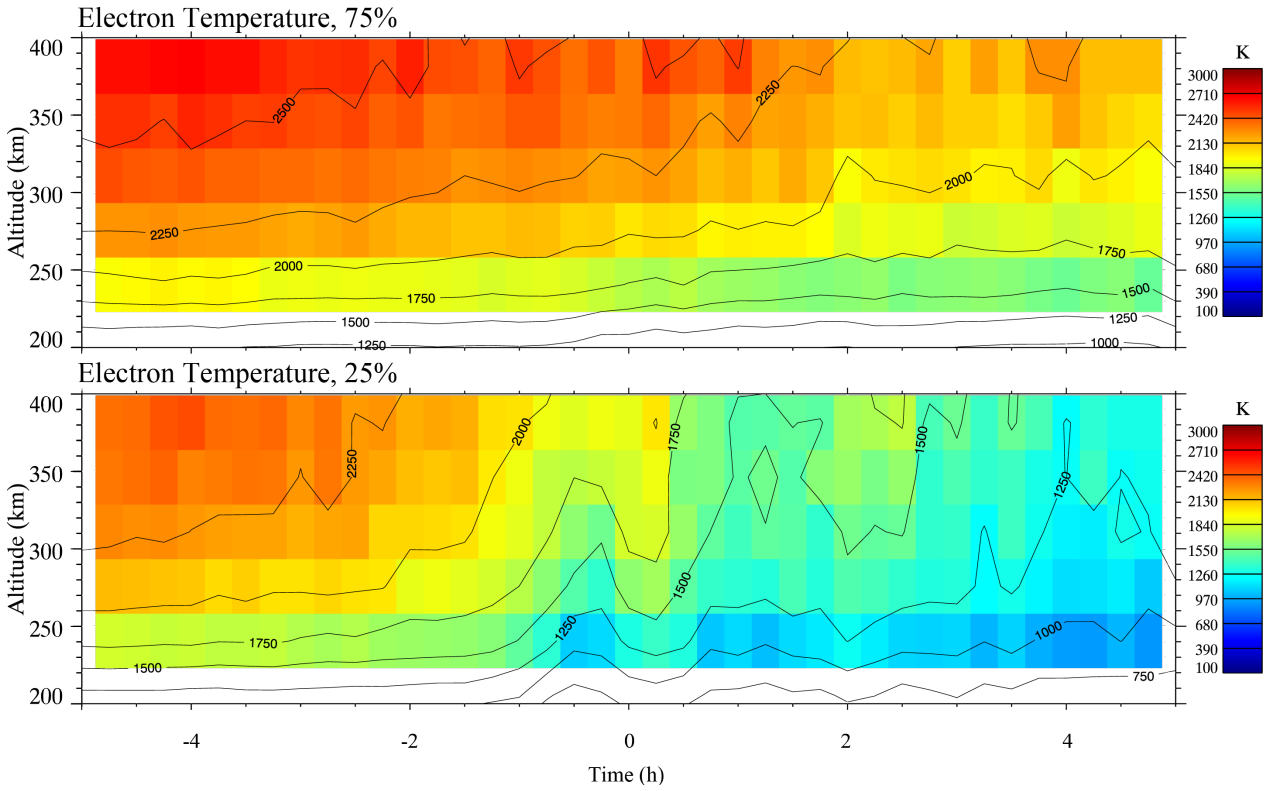

Figure 3.16: The percentiles of Figure 3.15. (Top Panel) 75 percentile of T_e. (Bottom Panel) 25 percentile of T_e.

From this it is found that to enhance the T_i by 300 K at 250 km in the evening, T_e would have to jump by roughly 1.3×10^4 K. The only T_e enhancement seen, the one from the 5-minute integration period epoch study, is only about 200 K and even that increase is associated to one single event.

3.5 Electric Field Origin of the T_i Spike Events

Given that the T_i enhancement is not due to T_n, m_n, or T_e, the only likely factor left is $|\mathbf{V}_i - \mathbf{V}_n|$. By re-arranging equation 1.14, $|\mathbf{V}_i - \mathbf{V}_n|$ could be inferred from the balance:

$$|\mathbf{V_i} - \mathbf{V}_n| \approx \sqrt{\frac{3k_b}{m_n}\left(T_i - \left[T_n + \frac{m_i + m_n}{m_i}\frac{\nu_{ie}}{\nu_{in}}\left(T_e - T_i\right)\right]\right)} \tag{3.3}$$

We sought to produce an epoch study of this particular parameter. However, for that, we needed to have an estimation for T_n. The T_n model given by the Mass Spectrometer and Incoherent Scatter radar (MSIS) 1990 model (referred to as the MSIS T_n (*Hedin*, 1992)) was examined for this purpose. For one thing, the MSIS1990 model also indicated, just like the CTIPe model, a gentle decrease in T_n above PFISR at dusk, hence furthering the conclusion that the T_i increase did not come from an increase in T_n.

From the Madrigal database, a T_i corrected for electron heat exchange (T_i^{corr}) was given. This can be written as[4]:

$$T_i^{corr} \approx T_i - \frac{m_i + m_n}{m_i}\frac{\nu_{ie}}{\nu_{in}}\left(T_e - T_i\right) \tag{3.4}$$

where $T_e \geq T_n$ and $T_i^{corr} \geq T_n$ is required (implied from equation 3.3). The expression for T_i^{corr} would agree with T_i if we assumed that $|\mathbf{V_i} - \mathbf{V}_n| = 0$. By plotting T_i, T_i^{corr} and T_n from MSIS over the period being examined (Figure 3.17, top panel is T_i, bottom panel contains T_i^{corr} and T_n) the relationship between these parameters is seen. Being that T_i^{corr} is spiky, it can be concluded again that T_e is not responsible for the T_i spike events. The problem presented in Figure 3.17, was that there were instances where T_i^{corr} was less than the T_n. Either the inferred T_n had to be decreased by some correction factor or T_i^{corr} had to

[4]It is important to note that this equation would also consider enhancements in T_e, further ensuring that the T_i spike events are not related to an enhancement in T_e

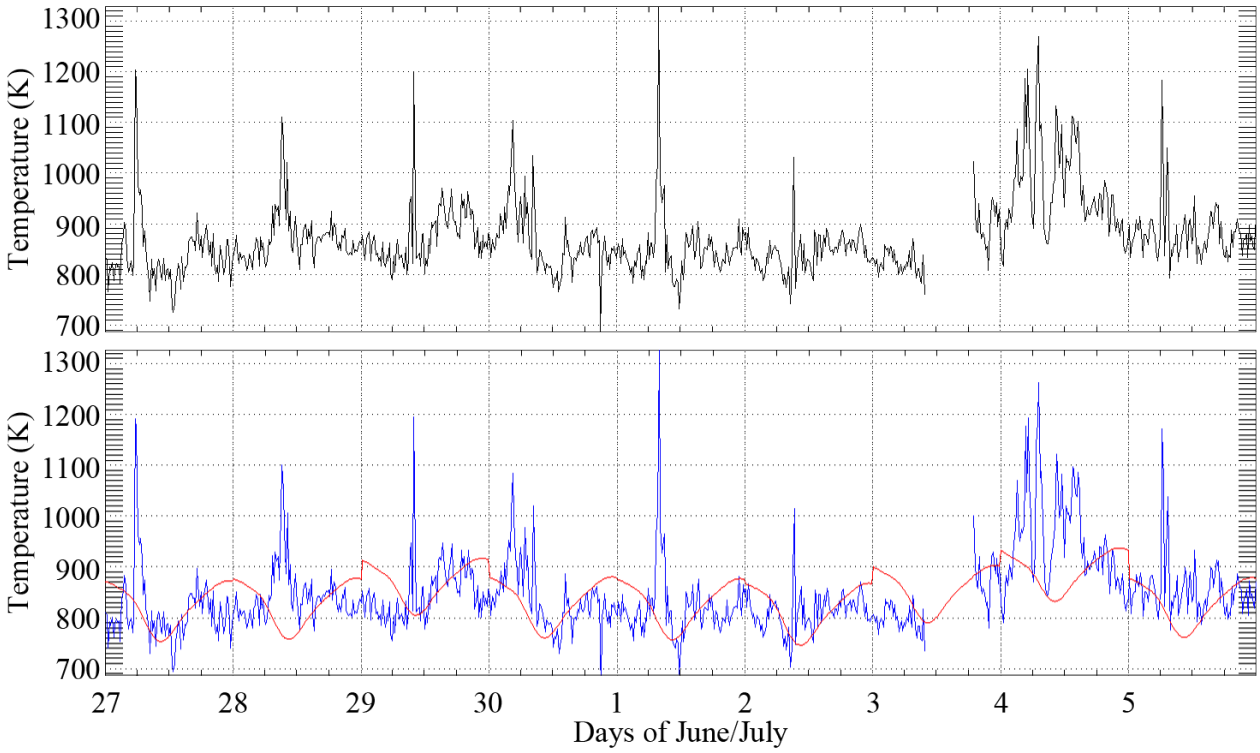

Figure 3.17: (Top Panel) T_i at 275.75 km from 27/June/2007 to 5/July/2007. (Bottom Panel) T_i^{corr} and T_n at 275.75 km from 27/June/2007 to 5/July/2007. Blue is T_i^{corr}. Red is the MSIS T_n.

be raised by a similar correction factor. To this end, a scatter plot of the MSIS T_n versus T_i^{corr} at the same time was created and examined (Figure 3.18). A 45° line was placed on this plot to indicate data points where the MSIS T_n was greater than T_i^{corr}. By subtracting 100 K from all the MSIS temperatures, the bulk of the data points were brought below the 45° line, meaning that all T_n were less than T_i^{corr}. This process gave a correction factor to the MSIS temperatures, which were then used in finding an inferred $|\mathbf{V}_i - \mathbf{V}_n|$ by subtracting 100 K from them.

The epoch study of the inferred $|\mathbf{V}_i - \mathbf{V}_n|$ shows a steep increase in the drift, followed by a brief decrease and increase, then a gradual decrease (Figure 3.19). The $|\mathbf{V}_i - \mathbf{V}_n|$ enhancement is from roughly 400 m/s to 700 m/s, near 250 km, and 600 m/s to 800 m/s higher up. It is interesting to note here that the decrease in this figure is more gradual than that seen by the equivalent epoch study of T_i.

In the 5-minute $|\mathbf{V}_i - \mathbf{V}_n|$ epoch study (Figure 3.20), the decrease is a little patchy and is less gradual than was seen in the 15-minute integration bins. The $|\mathbf{V}_i - \mathbf{V}_n|$ spike is

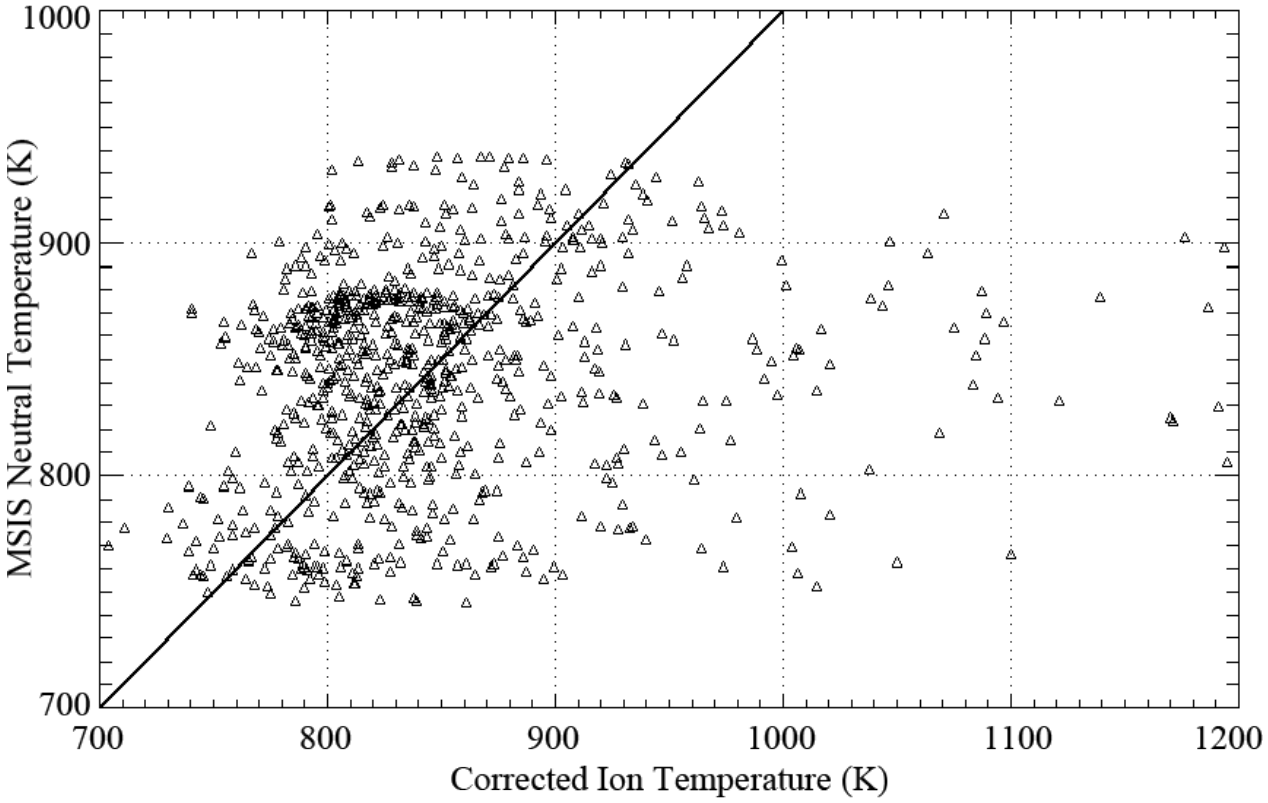

Figure 3.18: MSIS T_n versus T_i^{corr} for the same time. A 45° line is used as a guide to see how many instances there are where T_n is greater than T_i^{corr}.

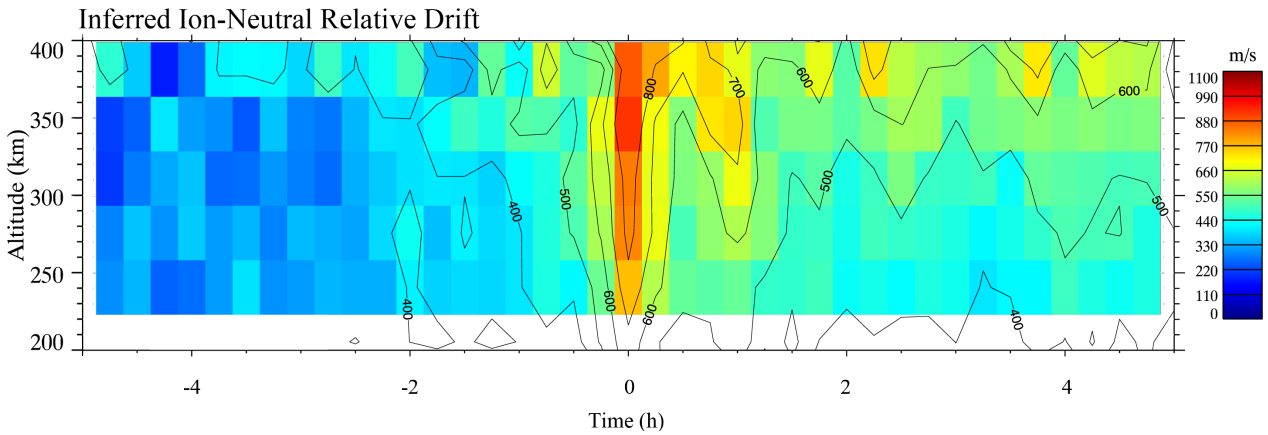

Figure 3.19: Inferred $|\mathbf{V}_i - \mathbf{V}_n|$ (subtracting 100 K from the MSIS T_n) epoch study of 15-minute integration bin data with all twenty-five T_i spike events within 1.5 hours of an n_e wall event at time zero. Period covered: 27/June/2007 to 5/July/2007 (seven spikes).

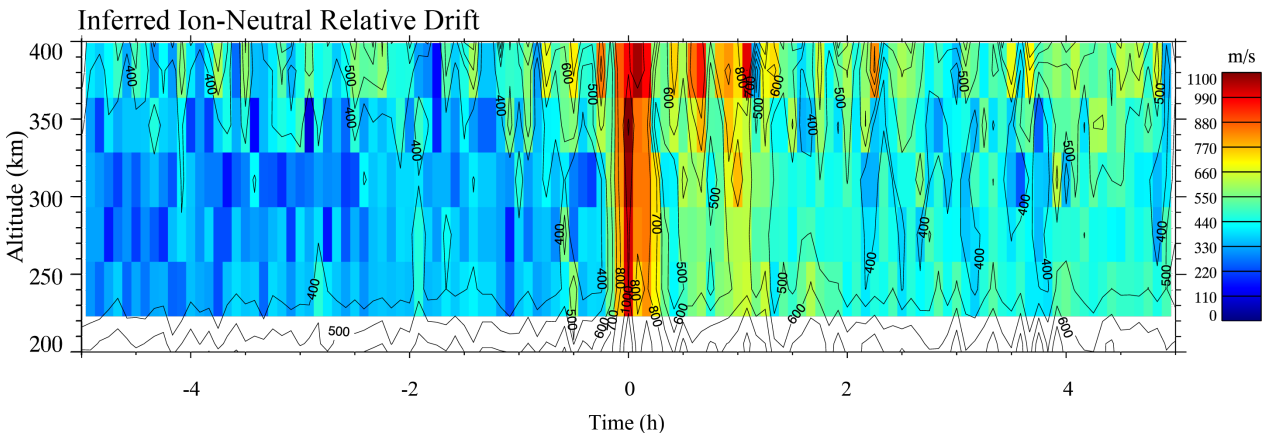

Figure 3.20: Same as Figure 3.19, but with 5-minute integration bins and not including 28/June/2007 (missing data) and 30/July/2007 (spike time is questionable).

sharper, and there is a slightly more enhanced section of the decrease region around time one, suggesting a second $|\mathbf{V}_i - \mathbf{V}_n|$ spike. This second spike in $|\mathbf{V}_i - \mathbf{V}_n|$ is associated with the second, less defined, T_i enhancement. The first spike is roughly 600 m/s above the background at 250 km (400 m/s to 1000 m/s), while the following enhancement is 100 m/s above the background (400 m/s to 500 m/s). Higher up, the first spike is roughly 400 m/s above the background (500 m/s to 900 m/s), while the following drift enhancement is 100 m/s above the background (500 m/s to 600 m/s).

A final $|\mathbf{V}_i - \mathbf{V}_n|$ epoch study was performed in which 15-minute integration bin data of all twenty-five T_i spike events within 1.5 hours of an n_e wall event were used (Figure 3.21). The same general trends are seen that were seen in the 15-minute integration bin epoch that only used seven spike events. A few differences are present, however. The steep increase is more gradual than in the other $|\mathbf{V}_i - \mathbf{V}_n|$ epoch studies. As well, the double hump is, instead, a gradual decline. The spike seen is roughly 200 m/s above the background at 250 km (500 m/s to 700 m/s), while higher up the enhancement is approximately 400 m/s above the background (600 m/s to 1000 m/s). In the 25% epoch study of $|\mathbf{V}_i - \mathbf{V}_n|$ (Figure 3.21, top panel) we see a spike in $|\mathbf{V}_i - \mathbf{V}_n|$ with minor features near-by. The 75% epoch study (Figure 3.21, bottom panel) contains an increase in the features around $t = 0$, obscuring the $|\mathbf{V}_i - \mathbf{V}_n|$ spike.

Given the evidence for these T_i enhancements to be related to increases in $|\mathbf{V}_i - \mathbf{V}_n|$, the T_i spike events had to be either due to an increase in the ion flow, the neutral wind or both.

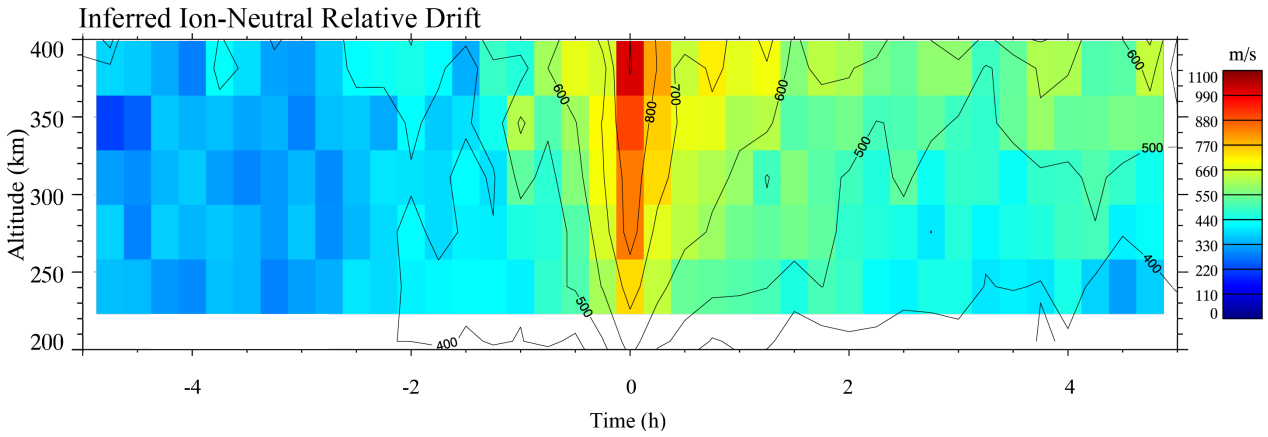

Figure 3.21: Inferred $|\mathbf{V}_i - \mathbf{V}_n|$ (subtracting 100 K from the MSIS T_n) epoch study of 15-minute integration bin data with all twenty-five T_i spike events within 1.5 hours of an n_e wall event at time zero. Period covered: 1/March/2007 to 29/February/2008.

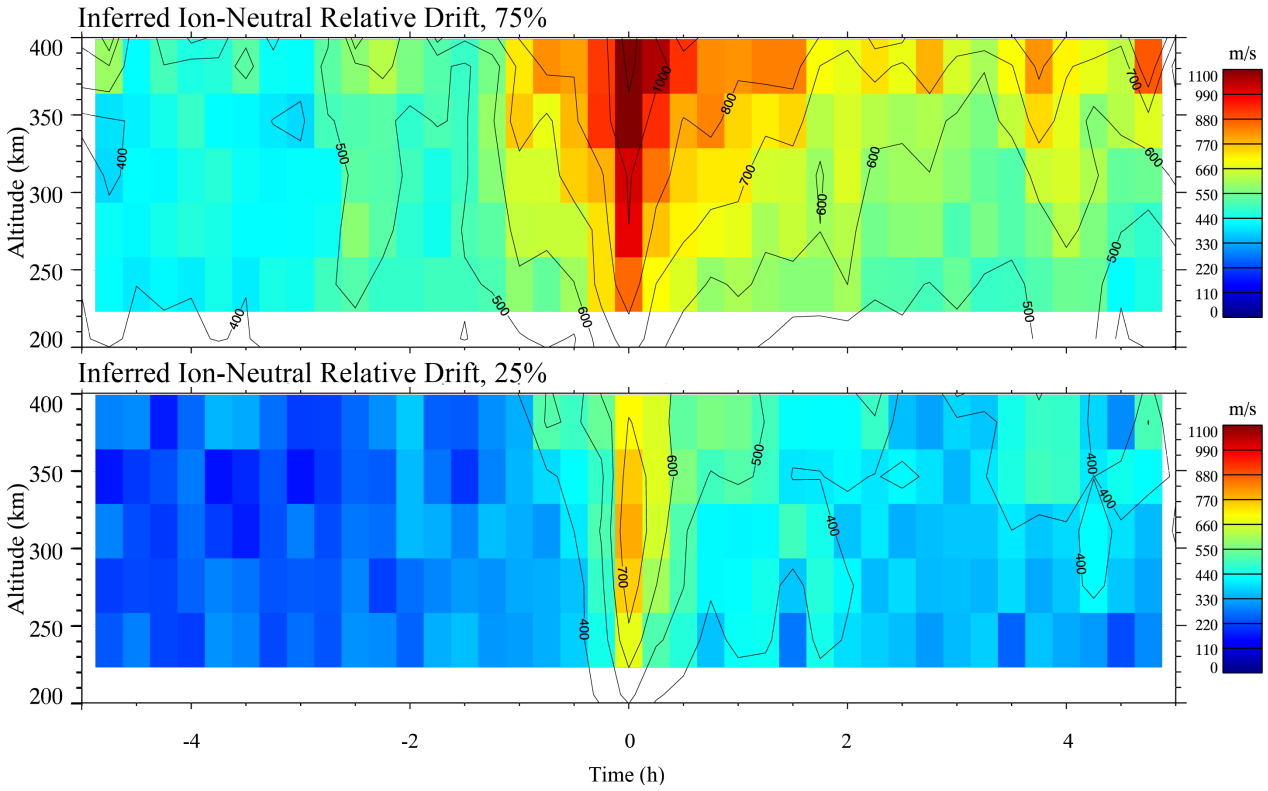

Figure 3.22: The percentiles of Figure 3.21. (Top Panel) 75 percentile of $|\mathbf{V}_i - \mathbf{V}_n|$. (Bottom Panel) 25 percentile of $|\mathbf{V}_i - \mathbf{V}_n|$.

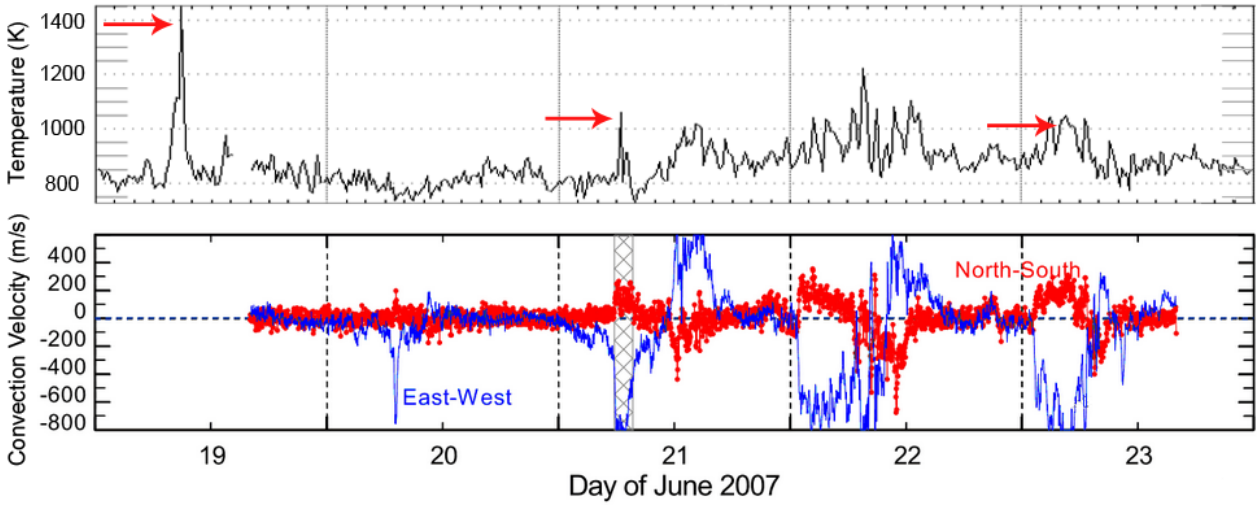

Figure 3.23: (Top Panel) T_i at 275 km. Arrows indicate spike events. (Bottom Panel) Convection velocities from *Richards et al.* (2013), which infer the electric field. Blue represents the east-west convection velocities. Red represents the north-south convection velocities. The hatched area shows the region where T_i and the northward convection velocity increase.

Because the spike events could be as short as 5 minutes there is a strong case to be made for them to be related to electric fields and therefore $\mathbf{V}_i$.

There were a few occasions for which the electric field could be derived through higher resolution campaigns that ran multiple beams examining more poleward regions. However, the only reliable electric field determination that could be done through this technique was 2 degrees of latitude to the north and beyond. While there were only a few observations associated with the times at which T_i spike events were obtained, for every T_i spike event observed, there was a corresponding northward electric field spike to the north of PFISR. One example of this is seen in Figure 3.23 for the 21/June/2007 spike event. Here, at the same time as a T_i spike event, there was an increase in the electric field, as can be inferred through the convection drift magnitudes. This shows that at least some of the T_i spike events are related to large scale changes in the electric field. It is interesting to point out, however, that not all electric field spikes to the north of the radar were associated with a T_i spike event. An explanation for this could simply be that the radar was sometimes equatorward of the convection region. However, this will be discussed in terms of the AE index in the next Chapter.

At this point it is concluded that the T_i spike events are related to an increase in $|\mathbf{V}_i - \mathbf{V}_n|$ that was roughly 1000 m/s. The most likely reason for an increase of this nature is an increase in the electric field leading to an enhancement in the associated $\mathbf{E} \times \mathbf{B}$ drift in the sunward direction. Not only would an increase in the electric field increase T_i, it would do so on the time scales observed for the T_i enhancement. As well, it would allow the possibility for a double hump in T_i through a second spike in electric field. By the same token, T_e, $\mathbf{V}_n$, T_n and m_n do not appear to be likely candidates for significant changes on the temporal or spatial scales associated with the spike events. In the next Chapter we utilize these constraints and magnetic indices to infer possible causes for the T_i spike events.

Chapter 4

Geophysical Interpretation

It was concluded in Chapter 3 that the increases in T_i were due to enhancements in $|\mathbf{V}_i - \mathbf{V}_n|$, having discarded other possible sources for a T_i increase, including increases in T_e, T_n, and/or m_n. It was also concluded that the $|\mathbf{V}_i - \mathbf{V}_n|$ increase had to come from an electric field. Partly this was because the existence of multiple spikes in T_i spike events suggested that the frictional heating effect was turned on, then off then on again, inferring a quick change in $|\mathbf{V}_i - \mathbf{V}_n|$. Being that electric fields had to be involved, this also means that the T_i increase related more to a bulk change in $\mathbf{V}_i$ (specifically through $\mathbf{E} \times \mathbf{B}$) rather than $\mathbf{V}_n$, which should not change quickly in time or space. The present Chapter discusses geophysical evidence, as well as processes that appeared to be responsible for the T_i events.

4.1 Magnetic Indices

An analysis of magnetic indices was carried out using 5-minute resolution data from the World Data Center for Geomagnetism, Kyoto, operated by the Data Center for Geomagnetism and Space Magnetism Graduate School of Science, Kyoto University. Part of this investigation entailed an epoch study of magnetic indices, aligned with the T_i spike events at time zero. This is seen in Figure 4.1 for every day where the T_i spike and n_e wall events were within 1.5 hours of each other, for a total of twenty-five days.

Very near the time of the T_i spike event, the AL, AO and the SYM-H indices reached a minimum value, while the AU and AE indices reached a maximum. However, the T_i spike events do not appear to happen at the exact same time as the respective maximums and minimums. The closest timings are seen with the AL and AE indices, which reach minima (in the case of the AL index) or maxima (in the case of the AE index) within roughly 20-30

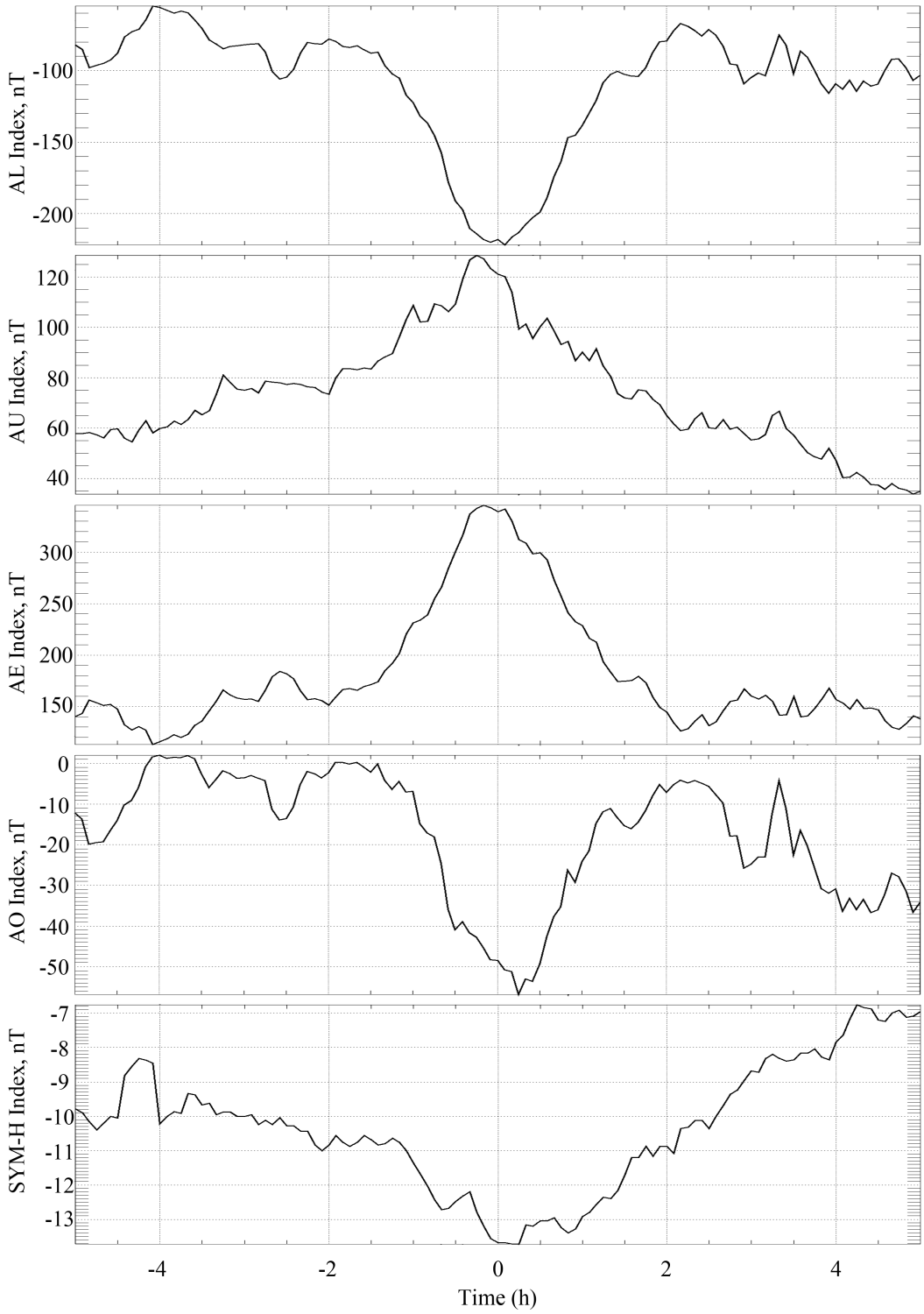

Figure 4.1: Epoch studies of magnetic indices with the T_i spike events at time zero. This only includes spike events that were within 1.5 hours of an n_e wall event. Period covered: 1/March/2007 to 29/February/2008. (Top Panel) AL index. (Second Panel from the Top) AU index. (Third Panel from the Top) AE index. (Fourth Panel from the Top) AO index. (Bottom Panel) SYM-H index.

minutes of the T_i enhancement. This offset may have been because of the radar's position in relation to the ionospheric convection pattern and plasmapause. Regardless, these plots show that the T_i spikes are linked to peaks in geomagnetic activity and therefore to a large scale electrodynamic process.

A different study of the relationship between the magnetic indices and the T_i spike events was carried out in which line plots of T_i, n_e and the magnetic indicies were plotted over time. Figure 4.2 portrays this with the AE index. This figure shows that every time there is a spike event, there is a strong peak in the AE index within 20 minutes of the T_i spike event. Since the AE index is used to measure the intensity of electric currents near the auroral zone and the T_i events had minimal precipitation (according to RTI plots of n_e), it is reasonable to suppose that an increase in the AE index would be associated with an increase in the overall electric field strength of the high latitude convection pattern (particularly near the plasmapause). This indicates that an intensification in the AE index was related to the T_i spike events through periods of enhancement in the global convection pattern, and likely linked to an expansion of the convection pattern to lower latitudes as well.

Two other important observations can be made from Figure 4.2. First, even though there is a maximum in the AE index whenever there is a T_i spike event, not every AE index maximum leads to a T_i spike, suggesting that the dusk plasmapause region favored the occurrence of T_i spike events. Second, the width of the T_i spike events and their corresponding AE increases are not the same. In some cases the AE index will be high for roughly one hour. This gives new meaning to the temporal size of the T_i spike events.

An investigation into the K_p index was done as well. However, this could not be done in the same manner as for the other indices because the K_p index is averaged over three hours. Instead, a histogram was created which marked the occurrences of K_p values at the time of the T_i spike events (Figure 4.3).

By looking at the K_p indices of all the T_i spike events within 1.5 hours of an n_e wall event, it is seen that these spike events have a median K_p value of 2 and are never less than 1. The size of these indicies lead us to believe that geomagnetic storms were not involved in these enhancements. This can be confirmed by referring back to Figure 4.1 were we see no indication of a strong decrease in the SYM-H index. As well, hourly information on the

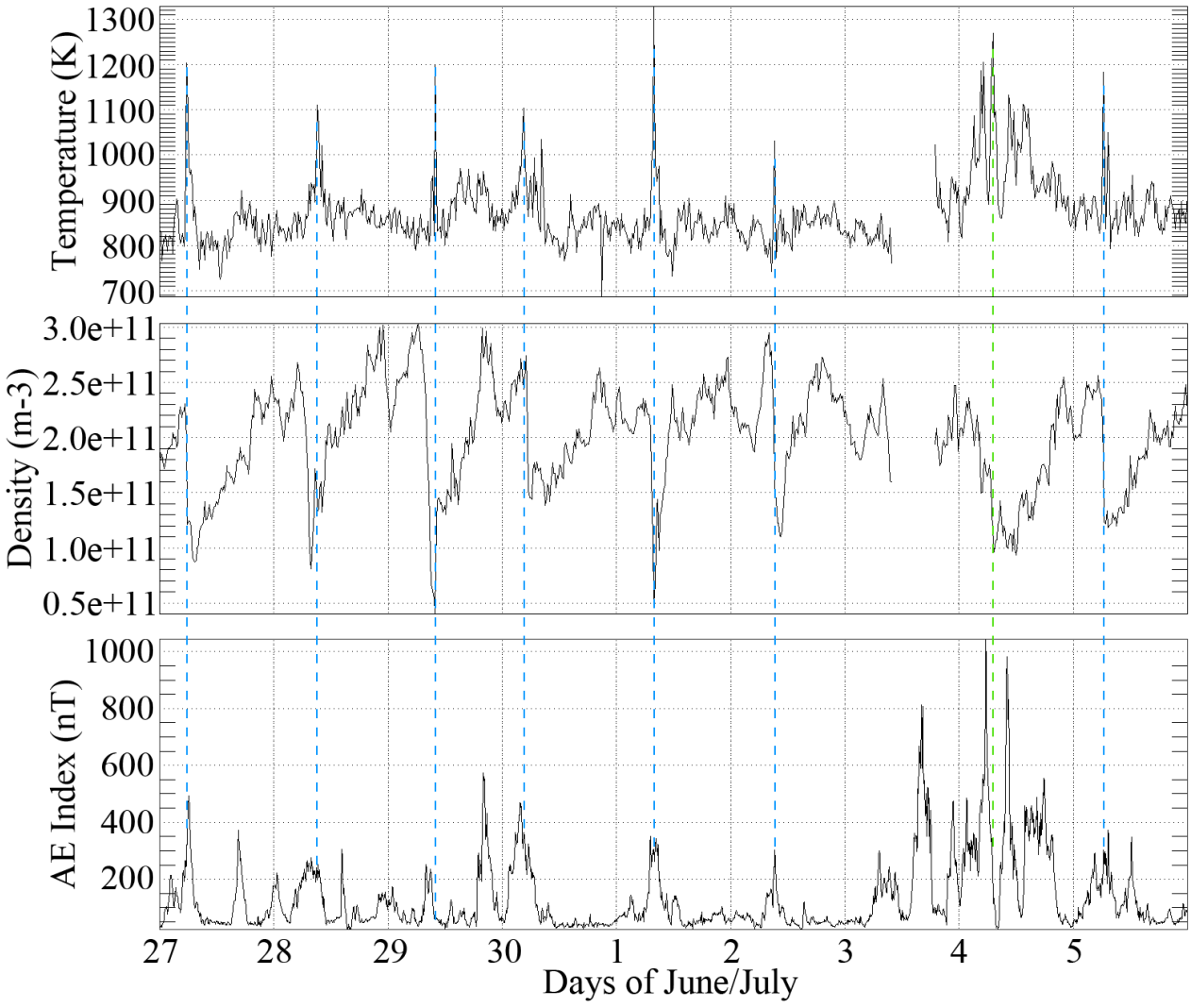

Figure 4.2: (Top Panel) T_i at 275 km from 27/June/2007 to 5/July/2007 as a function of UT. (Second Panel from the Top) n_e at 275 km. (Bottom Panel) AE index. Dashed lines indicate the time of the T_i enhancement (the green line was on a day of high geomagnetic activity, so declaring a spike event would be misleading).

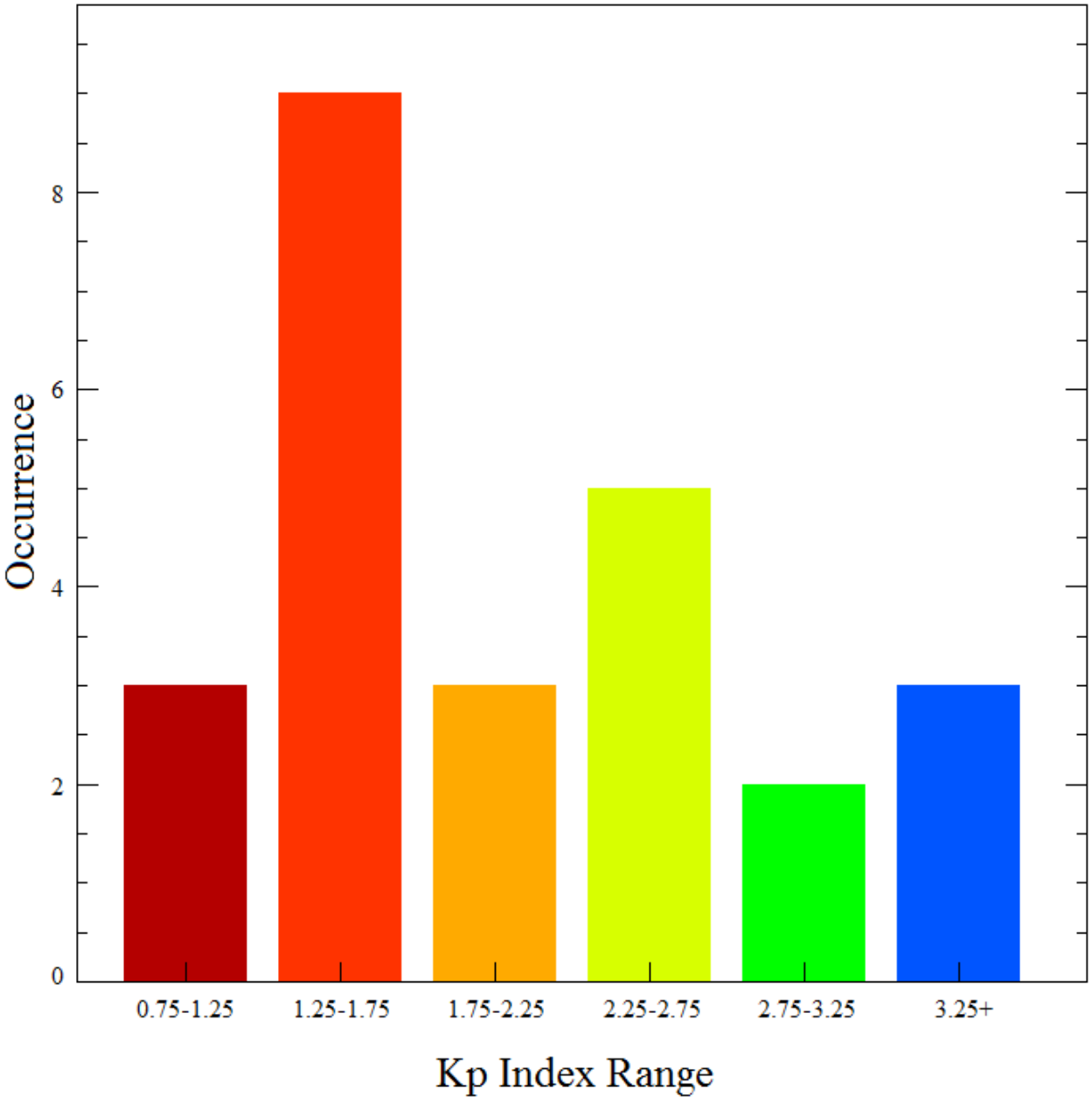

Figure 4.3: Histogram of the occurrence of certain K_p index ranges with spike events that were within 1.5 hours of an n_e wall event.

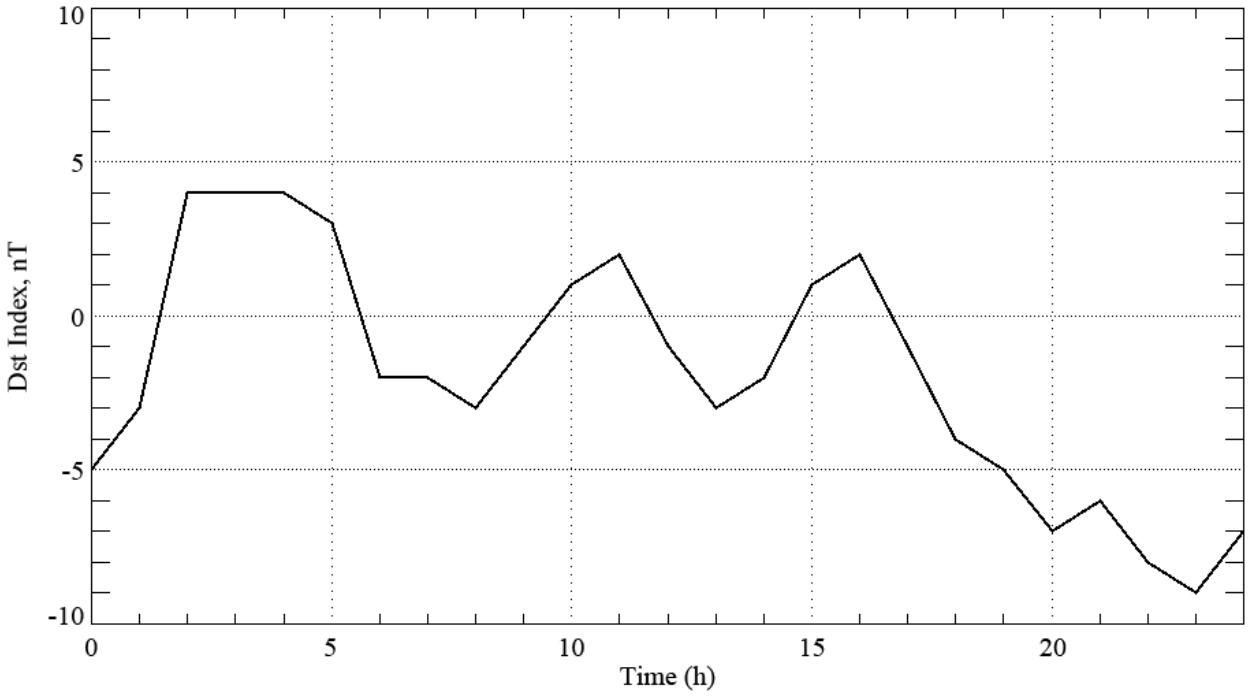

Figure 4.4: Hourly Dst information for a typical day with a T_i enhancement (June 27, 2007, where the spike event occurs at 5.602 UT).

Dst index show no strong depletion at the time of the T_i enhancement (Figure 4.4 shows the Dst indices for a typical day with a T_i enhancement). Although these T_i enhancements are clearly not related to geomagnetic storms they could still be substorm related events. In fact, this and the AE oscillations may explain why the K_p index is never less than 1 during T_i spike observations.

4.2 Possible Explanations for an Electric Field Increase

From the above information it can be concluded that a spike in T_i is, in fact, the result of a temporary increase in the electric field strength. However, two problems remain unsolved: why does PFISR only see the T_i enhancement in the dusk sector, and why are these T_i spike events so close to the night-side plasmapause? We can see two possible explanations: SAPS/SAIDs, and/or neutral wind shears.

4.2.1 The SAPS/SAIDs Possibility

Given that the T_i spike events are occurring in the subauroral region of the Earth, a possible explanation for the enhancements could be SAPS/SAIDs. As well, an important signature of a SAID is an increase in T_i because of the measured electric field (*Anderson et al.*, 1993). Figure 4.5 was created to emphasize the relationship between T_i and the inferred $|\mathbf{V}_i - \mathbf{V}_n|$. Here, values of T_i and $|\mathbf{V}_i - \mathbf{V}_n|$ at 275 km ($\nu_{in} \approx 0.4$ s^{-1} and $\nu_{ie} \approx 0.004$ s^{-1}) were taken from epoch studies that used all twenty-five spike events. Only values within 2 hours of time zero were taken in order to focus on the spike events. This being the case, the data points become more sparse as T_i and $|\mathbf{V}_i - \mathbf{V}_n|$ increase, in agreement with the observed steep increase and decrease in the spike events. The solid line represents $T_n = 600$ K and the dashed line represents $T_n = 800$ K (T_e is kept at 1500 K for the theoretical curves). We see that an increase in T_n moves the theoretical curve to higher T_i values. What is important to note from Figure 4.5 is that at the time of the enhancement $|\mathbf{V}_i - \mathbf{V}_n|$ changes from roughly 500 m/s to nearly 850 m/s while T_i changes from roughly 900 K to almost 1200 K. Given that the events are within the limitations and parameters of SAIDs, the T_i spike events could then possibly be signatures of SAID/SAPS events.

If the events were indeed SAPS/SAID, they had to be occurring in unison with a change in the ion convection pattern. This is because as PFISR rotates with the Earth, it will move nearly parallel to the plasma flow lines (equipotentials) inferred by SuperDARN (Figure 4.6). This means that if these were SAPS/SAID events, and the convection pattern was not changing, the T_i spike events should likely have spanned a longer time. Given the increase in the AE index at the time of the T_i enhancement, it is possible that there was indeed an increase in the convection pattern at the time of a SAPS/SAID event. To this end, an investigation into the AE index and the convection pattern around the time of the T_i spike event was performed.

In order to learn more about the convection pattern, the AE index data was compared to $\mathbf{V}_i$ data from DMSP (an example of a satellite pass of interest is seen in Figure 4.7). Being that DMSP satellites are able to render a two-dimensional ion velocity, DMSP data can be used to infer the size and strength of the convection pattern. SuperDARN is also

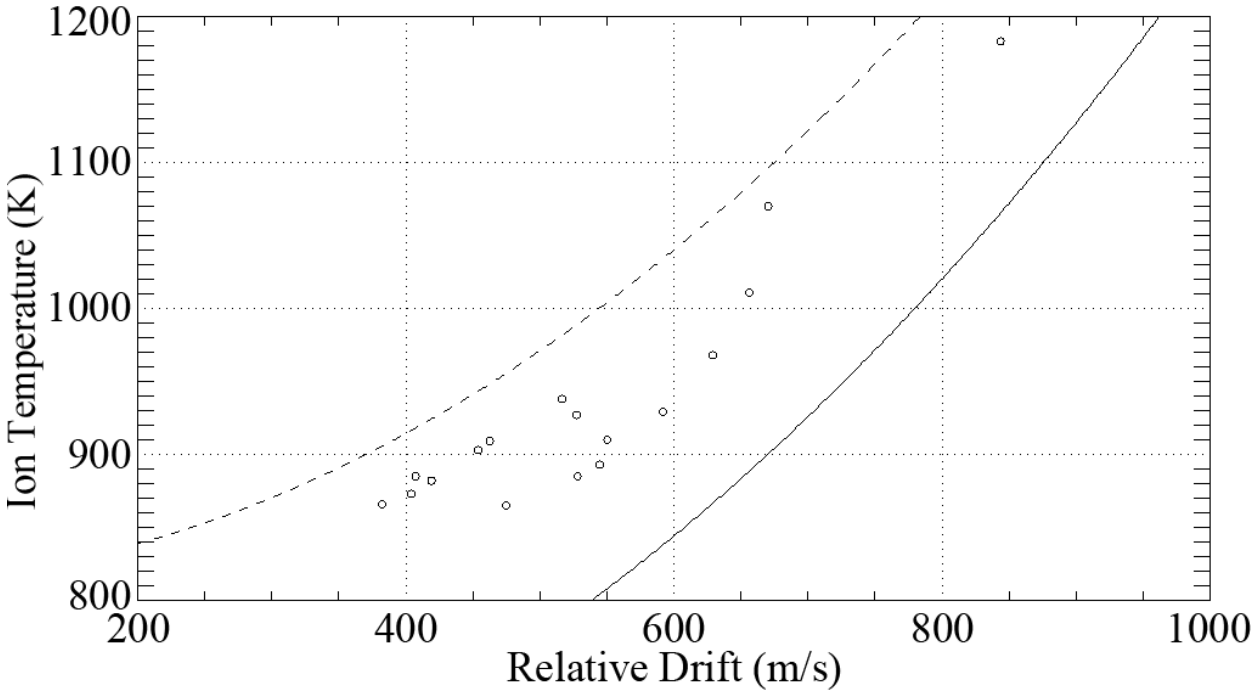

Figure 4.5: T_i versus $|\mathbf{V}_i - \mathbf{V}_n|$ at 275 km ($\nu_{in} \approx 0.4$ 1/s and $\nu_{ie} \approx 0.004$ 1/s) from epoch studies that used all twenty-five spike events. Only values within 2 hours of time zero were taken in order to focus on the spike events. The solid line represents the expected theoretical behavior for the F-region when $T_n = 600$ K, as does the dashed line for $T_n = 800$ K (T_e is kept at 1500 K).

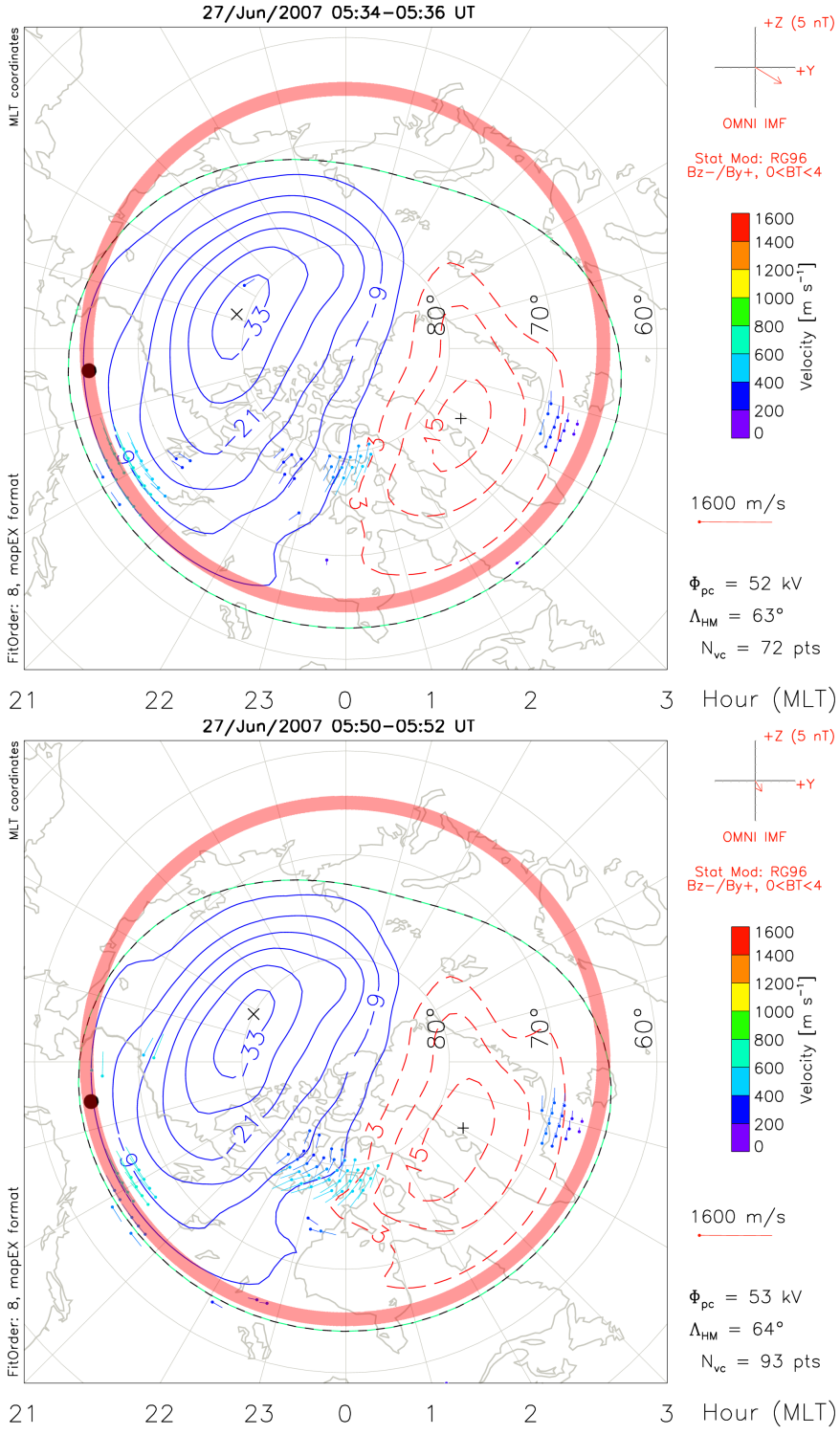

Figure 4.6: SuperDARN plasma convection maps. (Top Panel) Convection at a given time. (Bottom Panel) Convection 15 minutes afterwards. The red circle is the trajectory of PFISR and the dot on the circle is the approximate location of PFISR

a good indicator of the convection pattern, but DMSP will give high resolution cross-track measurements that do not rely on echo irregularities and ionospheric models. DMSP data from four satellites were retrieved for some of the dates containing T_i spikes and oscillations in the AE/AL indices. Due to depleted O^+ densities for the quiet conditions during 2007, the reliable data coverage was limited to the sunlit higher latitudes. As expected, for the orbits closest in time to the AE maxima, the high latitude convection was seen to be stronger than for the orbits before or after. However, for the summer data, the DMSP orbits were all distinctly sunward of the radar observations made when PFISR was in the dusk sector. For these locations at least, the convection was not structured and showed no sign of local enhancements near the plasmapause. This was expected, given the sunlit conditions. Taken together, the simultaneous intensification in the AE index, the handful of radar electric field observations, and the DMSP observations, were all consistent with the T_i spikes being associated with brief (1 to 2 hours) periods of enhancement in the global convection pattern. The spikes were observed right around the time when the AE index and the few recorded electric field measurements were reaching their peak (within 20 minutes of the recorded peaks in AE in particular).

It is interesting to note that the lower activity inferred from the K_p indices at the time of the T_i spike events could suggest a more intense and latitudinally narrow SAID event (*Smiddy et al.*, 1977; *Spiro et al.*, 1979; *Wang and Lühr*, 2011; *Wang et al.*, 2008). As well, the increase in the AE index could suggest an increased electric field near the plasmapause, explaining why the spike events are only near the equatorward edge of the sunward convection pattern and nowhere else in the rest of the convection region. Regardless, a problem with the SAPS/SAID interpretation is that these T_i events occurred throughout the year from 15 to 21 MLT, while typical SAIDs are seen in the winter around 21 MLT, away from sunlit conditions (*Wang et al.*, 2008). Being that SAPS/SAIDs, (SAIDs in particular) generally occur in months during or near the winter, the T_i enhancements may not have been related to SAPS/SAIDs.

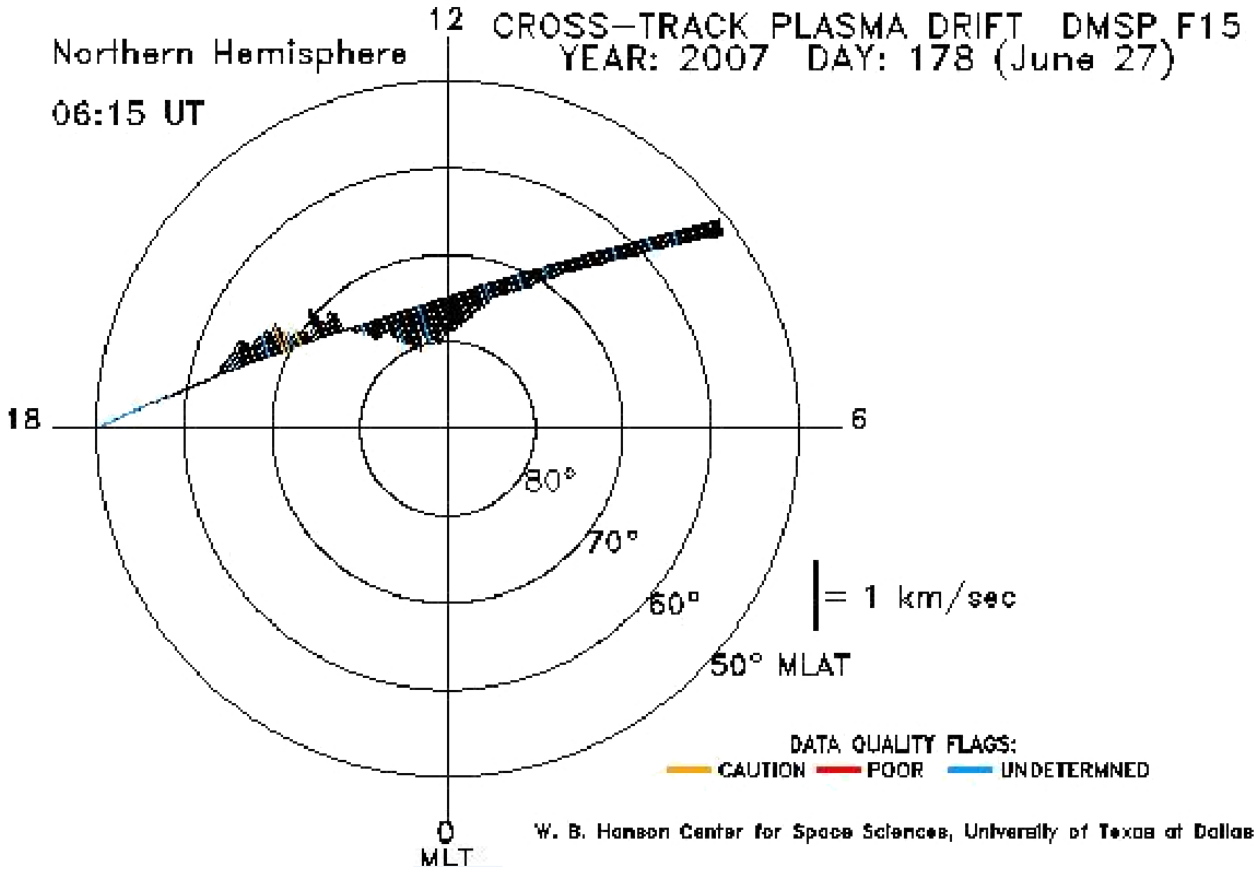

Figure 4.7: An example of a DMSP orbit over the Northern hemisphere.

4.2.2 The Neutral Wind Shear Hypothesis

Earlier it was found that in the region of the T_i enhancements, the neutral winds reverse northward of the ion flow (see Figure 3.12). This mechanism would increase $|\mathbf{V}_i - \mathbf{V}_n|$ and therefore T_i, but not on the 5 to 10 minute time scales seen in the epoch studies of PFISR data. This, though, does not mean that there is no involvement of neutral wind changes in the T_i spike events.

Equatorward of the plasmapause, roughly where the T_i enhancements are occurring, the neutral flow would be moving antisunward at a speed of roughly 300 m/s. When the AE index increases, convection would increase and the whole convection region would expand, moving the plasmapause equatorward. This would then result in ions moving sunward at roughly 500 m/s in a region where the neutrals are still flowing antisunward at about 300 m/s, creating strong frictional heating. This could bring $|\mathbf{V}_i - \mathbf{V}_n|$ to approximately 800m/s, which is what is needed, according to Figure 3.21. Then, poleward of this region and the plasmapause, ion drag would push the neutrals sunward with the ions, bringing $|\mathbf{V}_i - \mathbf{V}_n|$ to 200m/s. This would be seen by PFISR as a quick increase in T_i, followed by a more gradual decrease, essentially the structure seen in the T_i spike events. Referring to Figure 3.12, we see that the neutral winds in the dusk and dawn sectors move differently. This could explain why there is only a T_i enhancement in the evening sector.

Chapter 5

Conclusion and Future Work

By examining continuous data streams from PFISR during the IPY experiment, sudden T_i enhancements were discovered and concluded to be the aftermath of events increasing the electric field strength just poleward of the dusk plasmapause. Several possible reasons as to why there would be these enhancements in T_i where examined, including increases in T_e, T_n and/or m_n. However, by examining where the spike events happened and under what conditions they did happen, it was concluded that the T_i spike events were the result of quick increases in $|\mathbf{V}_i - \mathbf{V}_n|$ brought on by an electric field increase seen in the evening sector, just northward of the plasmapause.

It was concluded by investigating geophysical data and magnetic indices that the electric fields behind the spikes were localized in time, but would only be made manifest in the dusk sector on the equatorward edge of the high latitude convection region. Specifically, this conclusion came from the T_i spike events correlating with enhancements in the AE index. Furthermore, these AE index maxima would only translate into T_i enhancements when PFISR was examining plasma just poleward of the plasmapause, northward of the ion convection boundary. From this, two possible explanations for the events come to mind: SAPS/SAIDs, and/or a sudden change in the size of the ion convection pattern increasing the ion-neutral drag. The morphology of the events, if nothing else, favored the neutral wind interpretation.

Though it is clear that the T_i enhancements are the result of magnetic activity caused by an increase in the electric field near the plasmapause, the details of this process need elaboration. The location of these spike events, for example, requires further explanation. If these T_i spike events are indeed related to a neutral wind shear, then one way to do this may be to examine values for $\mathbf{V}_n$, which change in the CTIPe model from dusk to dawn. A different feature that requires more investigation is the AE index. This work has associated

the AE index maxima with substorms, but it would be important to verify what the AE index maxima truly indicate and if they are responsible for electric field enhancements.

A different issue that will require further investigation is the gentle increase in T_i with altitude seen in the RTI plots. From our epoch studies it can be seen, for example, that T_i, within the T_i enhancement, increases with altitude. It would be of interest to understand the origin of this increase. Some possibilities as to why this could be happening include temperature anisotropy (*McCrea et al.*, 1993), an increase in $T_{i||}$ from upwelling (*Loranc and St.-Maurice*, 1994), and conduction from above (*Schunk and Sojka*, 1982). Another possibility seen in Chapter 1 was an altitude variance of the $\mathbf{E} \times \mathbf{B}$ drift. As altitude increases, the ratio E/B increases, meaning that the drift produced by these perpendicular fields would increase with altitude. This would enhance $|V_i - V_n|$ at higher altitudes and therefore T_i.

A different possibility stems from PFISR making measurements along the magnetic field line. When PFISR reads in data that is along the geomagnetic field line, it is only approximately doing so. This is because the radar will perceive plasma along a straight line, instead of along the curved geomagnetic field line. So, an argument can be made that PFISR is actually perceiving slices of different latitudes at different altitudes. From this, if different latitudes were heated differently, a gradient in the temperature would appear, possibly like the one seen in the data. This stated, the enhancements appear to be on both sides of the T_i spike events, which does not agree with this explanation.

Bibliography

Aarons, J., and B. Lin, Development of high latitude phase fluctuations during the January 10, April 10–11, and May 15, 1997 magnetic storms, *Journal of Atmospheric and Solar-Terrestrial Physics*, *61*(3), 309–327, 1999.

Anderson, P. C., W. B. Hanson, R. A. Heelis, J. D. Craven, D. N. Baker, and L. A. Frank, A proposed production model of rapid subauroral ion drifts and their relationship to substorm evolution, *Journal of Geophysical Research*, *98*(A4), 6069–6078, 1993.

Anderson, P. C., D. L. Carpenter, K. Tsuruda, T. Mukai, and F. J. Rich, Multisatellite observations of rapid subauroral ion drifts (SAID), *Journal of Geophysical Research*, *106*(A12), 29585–29, 2001.

Arnoldy, R. L., Signature in the interplanetary medium for substorms, *Journal of Geophysical Research*, *76*(22), 5189–5201, 1971.

Baumjohann, W. and R. A. Treumann, *Basic Space Plasma Physics*, Imperial College Press, 1997.

Borovsky, J. E., and M. H. Denton, Differences between CME-driven storms and CIR-driven storms, *Journal of Geophysical Research*, *111*(A7), 2006.

Boudouridis, A., and L. R. Lyons, and E. Zesta, and J. M. Ruohoniemi, Dayside reconnection enhancement resulting from a solar wind dynamic pressure increase, *Journal of Geophysical Research*, *112*(A6), A06201, 2007.

Chang, C. A., and J.-P. St.-Maurice, Two-dimensional high-latitude thermospheric modeling: A comparison between moderate and extremely disturbed conditions, *Canadian Journal of Physics*, *112*(8-9), 1007–1031, 1991.

Chappell, C. R., K. K. Harris, and G. W. Sharp, *Particles and Fields in the Magnetosphere*, Springer, 1970.

Chen, F. F., *Introduction to Plasma Physics and Controlled Fusion*, Springer, 2006.

De Keyser, J., Formation and evolution of subauroral ion drifts in the course of a substorm, *Journal of Geophysical Research*, *104*(A6), 12339–12349, 1999.

De Keyser, J., Storm-Time Energetic Particle Penetration into the Inner Magnetosphere as the Electromotive Force in the Subauroral Ion Drift Current Circuit, *Magnetospheric Current Systems*, 261–265, 2000.

De Keyser, J., M. Roth, and J. Lemaire, The magnetospheric driver of subauroral ion drifts, *Geophysical research letters*, *25*(10), 1625–1628, 1998.

Erickson, P., ISR Practicalities: Data Reduction, URL: `http://www.haystack.mit.edu/cgi-bin/asg_science/science.cgi/2012_ISR_School`, 2012.

Evans, J. V., Ionospheric movements measured by incoherent scatter: A review, *Journal of Atmospheric and Terrestrial Physics*, *34*(2), 175–209, 1972.

Feldstein, Y. I., and G. V. Starkov, Dynamics of auroral belt and polar geomagnetic disturbances, *Planetary and Space Science*, *15*(2), 209–229, 1967.

Forbes, T. G., E. W. Hones, S. J. Bame, J. R. Asbridge, G. Paschmann, N. Sckopke, and C. T. Russel, Evidence for the tailward retreat of a magnetic neutral line in the magnetotail during substorm recovery, *Geophysical Research Letters*, *8*(3), 261–264, 1981.

Foster, J. C., and W. Burke, SAPS: A new categorization for sub-auroral electric fields, *Eos, Transactions, American Geophysical Union*, *83*(36), 393, 2002.

Foster, J. C., and H. B. Vo, Average characteristics and activity dependence of the subauroral polarization stream, *Journal of Geophysical Research*, *107*(A12), 1475, 2002.

Foster, J. C., D. H. Fairfield, K. W. Ogilvie, and T. J. Rosenburg, Relationship of interplanetary parameters and occurrence of magnetospheric substorms, *Journal of Geophysical Research*, *76*(28), 6971–6975, 1971.

Frank, L. A., J. A. Van Allen, and H. K. Hills, A study of charged particles in the earth's outer radiation zone with Explorer 14, *Journal of Geophysical Research*, *69*(11), 2171–2191, 1964.

Fried, B. D., and S. D. Conte, *The Plasma Dispersion Function*, New York: Academic Press, 1961.

Fuller-Rowell, T. J., A two-dimensional, high-resolution, nested-grid model of the thermosphere: 1. Neutral response to an electric field "spike", *Journal of Geophysical Research*, *89*, 2971, 1984.

Fuller-Rowell, T. J., D. Rees, S. Quegan, G. J. Bailey, and R. J. Moffett, The effect of realistic conductivities on the high-latitude neutral thermospheric circulation, *Planetary and Space Science*, *32*(4), 469–480, 1984.

Fuller-Rowell, T. J., A. D. Richmond, and N. Maruyama, Global modeling of storm-time thermospheric dynamics and electrodynamics, *Geophysical Monograph Series*, *181*, 187–200, 2008.

Fuller-Rowell, T. J., and D. Rees, A three-dimensional, time-dependent simulation of the global dynamical response of the thermosphere to a geomagnetic substorm, *Journal of Atmospheric and Terrestrial Physics*, *43*(7), 701, 1981.

Galperin, Y. I., V. N. Ponomarev, and A. G. Zosimova, Plasma convection in polar ionosphere, *Annales Geophysicae*, *30*(1), 1-7, 1974.

Gillies, D. M., K. A. McWilliams, J.-P. St.-Maurice, and S. E. Milan, Global-scale observations of ionospheric convection during geomagnetic storms, *Journal of Geophysical Research*, *116*(A12), doi: 10.1029/2011JA017086, 2011.

Gillies, D. M., J.-P. St.-Maurice, K. A. McWilliams, and S. E. Milan, Global-scale observations of ionospheric convection variation in response to sudden increases in the solar wind dynamic pressure, *Journal of Geophysical Research*, *117*(A4), doi: 10.1029/2011JA017255, 2012.

Goldstein, J., Plasmasphere response: Tutorial and review of recent imaging results, in *Solar Dynamics and Its Effects on the Heliosphere and Earth*, pp. 203-213, Springer, 2007.

Goldstein, J., B. R. Sandel, M. R. Hairston, and P. H. Reiff, Control of plasmaspheric dynamics by both convection and sub-auroral polarization stream, *Geophysical Research Letters*, *30*(24), 2003.

Gordon, W. E., Incoherent Scattering of Radio Waves by Free Electrons with Applications to Space Exploration by Radar, *Proceedings of the IRE*, *46*(11), 1824-1829, 1958.

Grebowsky, J. M., Model study of plasmapause motion, *Journal of Geophysical Research*, *75*(22), 4329–4333, 1970.

Greenwald, R. A., K. B. Baker, J. R. Dudeney, M. Pinnock, T. B. Jones, E. C. Thomas, J-P. Villain, J-C. Cerisier, C. Senior, C. Hanuise, and others, DARN/SuperDARN, *Space Science Reviews*, *71*(1-4), 761–796, 1995.

Haerendel, G., and R. Lüst, and E. Rieger, Motion of artificial ion clouds in the upper atmosphere, *Planetary and Space Science*, *15*(1), 1–18, 1967.

Hagfors, T., Plasma Fluctuations Excited by Charged Particle Motion and their Detection by Weak Scattering of Radio Waves, *Incoherent Scatter: Theory, Practice and Science*, 1995.

Harra, L. K. and Mason, K. O. *Space Science*. Imperial College Press, 2004.

Hedin, A. E., MSISE model (1990), *Planetary and Space Science*, *40*(4), 556, 1992.

Heelis, R. A., The effects of interplanetary magnetic field orientation on dayside high-latitude ionospheric convection, *Journal of Geophysical Research*, *89*(A5), 2873–2880, 1984.

Heelis, R. A., J. K. Lowell, and R. W. Spiro, A model of the high-latitude ionospheric convection pattern, *Journal of Geophysical Research*, *87*(A8), 6339–6345, 1982.

Heinselman, C., Data Analysis and Fitting 1, URL: `http://www.haystack.mit.edu/cgi-bin/asg_science/science.cgi/2012_ISR_School`, 2012.

Heinselman, C., Phased Array Radars, URL: http://www.haystack.mit.edu/cgi-bin/asg_science/science.cgi/2012_ISR_School, 2012.

Holt, B. J., Drift scintillation meter for the defense meteorological satellite program (Final Report, 12 Jan. 1988- 30 Sep. 1992), URL: http://oai.dtic.mil/oai/oai?verb=getRecord&metadataPrefix=html&identifier=ADA259993, 1992.

Hones Jr., and W. Edward, *Magnetic reconnection in space and laboratory plasmas*, American Geophysical Union, 1984.

Ichimaru, S., *Basic Principles of Plasma Physics*. W. A. Benjamin, Inc., Reading, Massachusetts, 1973.

Karlsson, T., G. T. Marklund, L. G. Blomberg, and A. Mälkki, Subauroral electric fields observed by the Freja satellite: A statistical study, *Journal of Geophysical Research*, *103*(A3), 4327–4341, 1998.

Kelley, M. C., *The Earth's Ionosphere: Plasma Physics & Electrodynamics*, Elsevier, 2009.

Killeen, T. L., P. B. Hays, G. R. Carignan, R. A. Heelis, W. B. Hanson, N. W. Spencer, and L. H. Brace, Ion-neutral coupling in the high-latitude F-region: Evaluation of ion heating terms from Dynamics Explorer 2, *Journal of Geophysical Research*, *89*(A9), 7495–7508, 1984.

King, J. W., and H. Kohl, Upper atmospheric winds and ionospheric drifts caused by neutral air pressure gradients, *Nature*, *206*, 699–701, 1965.

Lemaire, J. F., M. Roth, and J. De Keyser, High altitude electrostatic fields driving subauroral ion drifts, *COSPAR Colloquia Series*, *9*, 61–64, Elsevier, 1998.

Lemaire, J. F. and K. I. Gringauz, *The Earth's plasmasphere*, Cambridge, 2005.

Loranc, M. and J.-P. St.-Maurice, A Time-Dependent Gyro-Kinetic Model of Thermal Ion Upflows in the High-Latitude F-Region, *Journal of Geophysical Research*, *99*(A9), 17429-17451, 1994.

Maynard, N. C. and Heppner, J. P., *Variations in Electric Fields from Polar Orbiting Satellites*, Springer, 1970.

McCrea, I. W., M. Lester, T. R. Robinson, J-P. St-Maurice, N. M. Wade, and T. B. Jones, Derivation of the ion temperature partition coefficient β from the study of ion frictional heating events, *Journal of Geophysical Research*, *98*(A9), 15701–15715, 1993.

McPherron, R. L., Growth phase of magnetospheric substorms, *Journal of Geophysical Research*, *75*(28), 5592–5599, 1970.

McPherron, R. L., Magnetospheric substorms, *Reviews of Geophysics*, *17*(4), 657–681, 1979.

McPherron, R. L., *Introduction to Space Physics*, Cambridge University Press, 1995.

Mozer, F. S., and P. Bruston, Electric field measurements in the auroral ionosphere, *Journal of Geophysical Research*, *72*(3), 1109–1114, 1967.

Mozer, F. S., and R. Serlin, Magnetospheric electric field measurements with balloons, *Journal of Geophysical Research*, *74*(19), 4739–4754, 1969.

Nishida, A., and N. Nagayama, Synoptic survey for the neutral line in the magnetotail during the substorm expansion phase, *Journal of Geophysical Research*, *78*(19), 3782–3798, 1973.

Park, C. G., Downward mapping of high-latitude ionospheric electric fields to the ground, *Journal of Geophysical Research*, *81*(1), 168–174, 1976.

Perkins, F. W., and R. G. Roble, Ionospheric heating by radio waves: Predictions for Arecibo and the satellite power station, *Journal of Geophysical Research*, *83*(A4), 1611–1624, 1978.

Pudovkin, M. I., Electric fields and currents in the ionosphere, *Space Science Reviews*, *16*(5-6), 727–770, 1974.

Rees, M. H., *Physics and Chemistry of the Upper Atmosphere*, Cambridge University Press, 1989.

Reiff, P. H., Sunward convection in both polar caps, *Journal of Geophysical Research*, *87*(A8), 5976–5980, 1982.

Reiff, P. H., and J. L. Burch, IMF By-dependent plasma flow and Birkeland currents in the dayside magnetosphere: 2. A global model for northward and southward IMF, *Journal of Geophysical Research*, *90*(A2), 1595–1609, 1985.

Richards, P. G., M. J. Nicholls, J.-P. St. Maurice, and T. N. Woods, Investigation of pre-midnight ion temperature spikes and electron density depletions observed by the PFISR radar at Poker Flat, Alaska, manuscript in preparation, 2013.

Rishbeth, H., and W. B. Hanson, A comment on plasma pile-up in the F-region, *Journal of Atmospheric and Terrestrial Physics*, *36*(4), 703–706, 1974.

Ruohoniemi, J., and K. Baker, Large-scale imaging of high-latitude convection with Super Dual Auroral Radar Network HF radar observations, *Journal of Geophysical Research*, *103*(A9), 20,797, 1998.

Sadler, F. B., M. Lessard, E. Lund, A. Otto, and H. Lühr, Auroral precipitation/ion upwelling as a driver of neutral density enhancement in the cusp, *Journal of Atmospheric and Solar-Terrestrial Physics*, *87*, 82–90, 2012.

Schunk, R. W., Transport equations for aeronomy, *Planetary and Space Science*, *23*(3), 437–485, 1975.

Schunk, R. W., and A. F. Nagy, Electron temperatures in the F-region of the ionosphere: Theory and observations, *Reviews of Geophysics*, *16*(3), 355–399, 1978.

Schunk, R. W. and A. F. Nagy, *Ionospheres: Physics, Plasma Physics and Chemistry*, Cambridge, 2000.

Schunk, R. W., and J. J. Sojka, Ion temperature variations in the daytime high-latitude F-region, *Journal of Geophysical Research*, *87*(A7), 5169–5183, 1982.

Sedgemore-Schulthess, F. and J.-P. St.-Maurice, Naturally Enhanced Ion-Acoustic Spectra And Their Interpretation, *Surveys in Geophysics*, *22*(1), 55-92, 2001.

Semeter, J., Basic Radar Signal Processing, URL: `http://www.haystack.mit.edu/cgi-bin/asg_science/science.cgi/2012_ISR_School`, 2012.

Sheffield, J., *Plasma Scattering of Electromagnetic Radiations*, Academic Press, Inc., 1975.

Sheffield, J., Updating Plasma Scattering of Electromagnetic Radiation, *Journal of Physics: Conference Series*, *227*(1), 2010.

Shibata, K. C., S. Masuda, M. Shimojo, H. Hara, T. Yokoyama, S. Tsuneta, T. Kosugi, and Y. Ogawara, Hot-plasma ejections associated with compact-loop solar flares, *The Astrophysical Journal Letters*, *451*(2), 1995.

Shue, J.-H., J. K. Chao, H. C. Fu, C. T. Russell, P. Song, K. K. Khurana, and H. J. Singer, A new functional form to study the solar wind control of the magnetopause size and shape, *Journal of Geophysical Research*, *102*(A5), 9497–9511, 1997.

Smiddy, M., M. C. Kelley, W. Burke, F. Rich, R. Sagalyn, B. Shuman, R. Hays, S. Lai, Intense poleward-directed electric fields near the ionospheric projection of the plasmapause, *Geophysical Research Letters*, *4*(11), 543, 1977.

Sojka, J. J, M. J. Nicolls, C. J. Heinselman, and J. D. Kelley, The PFISR IPY observations of ionospheric climate and weather, *Journal of Atmospheric and Solar-Terrestrial Physics*, *71*(6), 771–785, 2009.

Spiro, R., R. Heelis, and W. Hanson, Rapid subauroral ion drifts observed by Atmosphere Explorer C, *Geophysical Research Letters*, *6*(8), 657, 1979.

St.-Maurice, J.-P., and W. Hanson, A statistical study of F-region ion temperatures at high latitudes based on Atmosphere Explorer C data, *Journal of Geophysical Research*, *89*(A2), 987, 1984.

St-Maurice, J.-P., and R. Schunk, Ion-neutral momentum coupling near discrete high-latitude ionospheric features, *Journal of Geophysical Research*, *86*(A13), 11, 299, 1981.

St.-Maurice, J.-P., and W. B. Hanson, Ion frictional heating at high latitudes and its possible use for an in situ determination of neutral thermospheric winds and temperatures, *Journal of Geophysical Research*, *87*(A9), 7580–7602, 1982.

Wang, H., and H. Lühr, The efficiency of mechanisms driving Subauroral Polarization Streams (SAPS), in *Annales Geophysicae*, *29*, 1277, 2011.

Wang, H., A. J. Ridley, H. Lühr, M. W. Liemohn, and S. Y. Ma, Statistical study of the subauroral polarization stream: Its dependence on the cross–polar cap potential and subauroral conductance, *Journal of Geophysical Research*, *113*(A12), 311, 2008.

Wickwar, V. B., C. Lathuillere, W. Kofman, and G. Lejeune, Elevated Electron Temperatures in the Auroral E Layer Measured With the Chatanika Radar, *Journal of Geophysical Research*, *86*(A6), 4721-4730, 1981.

Woodward, P. M., *Probability and Information Theory with Applications to Radar*, Artech House, 1980.

Yeh, H.-C., J. C. Foster, F. J. Rich, and W. Swider, Storm time electric field penetration observed at mid-latitude, *Journal of Geophysical Research*, *96*(A4), 5707–5721, 1991.

Zarka, P, *Encyclopedia of Astrobiology*, Springer, 2011.

Zell, H., Van Allen Probes: Mission Overview, URL: `http://www.nasa.gov/mission_pages/rbsp/mission/index.html#.UrFaa_RDvXQ`, 2013.

Zhang, J., I. G Richardson, D. F. Webb, N. Gopalswamy, E. Huttunen, J. C. Kasper, N. V. Nitta, W. Poomvises, B. J. Thompson, and C.-C. Wu, Solar and interplanetary sources of major geomagnetic storms (Dst $\leq$ -100 nT) during 1996–2005, *Journal of Geophysical Research*, *112*(A10), 2007.

Appendix A

Additional Data from 27/June to 5/July/2007

15- and 5-minute integration period RTI plots were completed for everyday from 27/June/2007 to 5/July/2007. This appendix contains the RTI plots and convection maps not featured in Chapter 3.

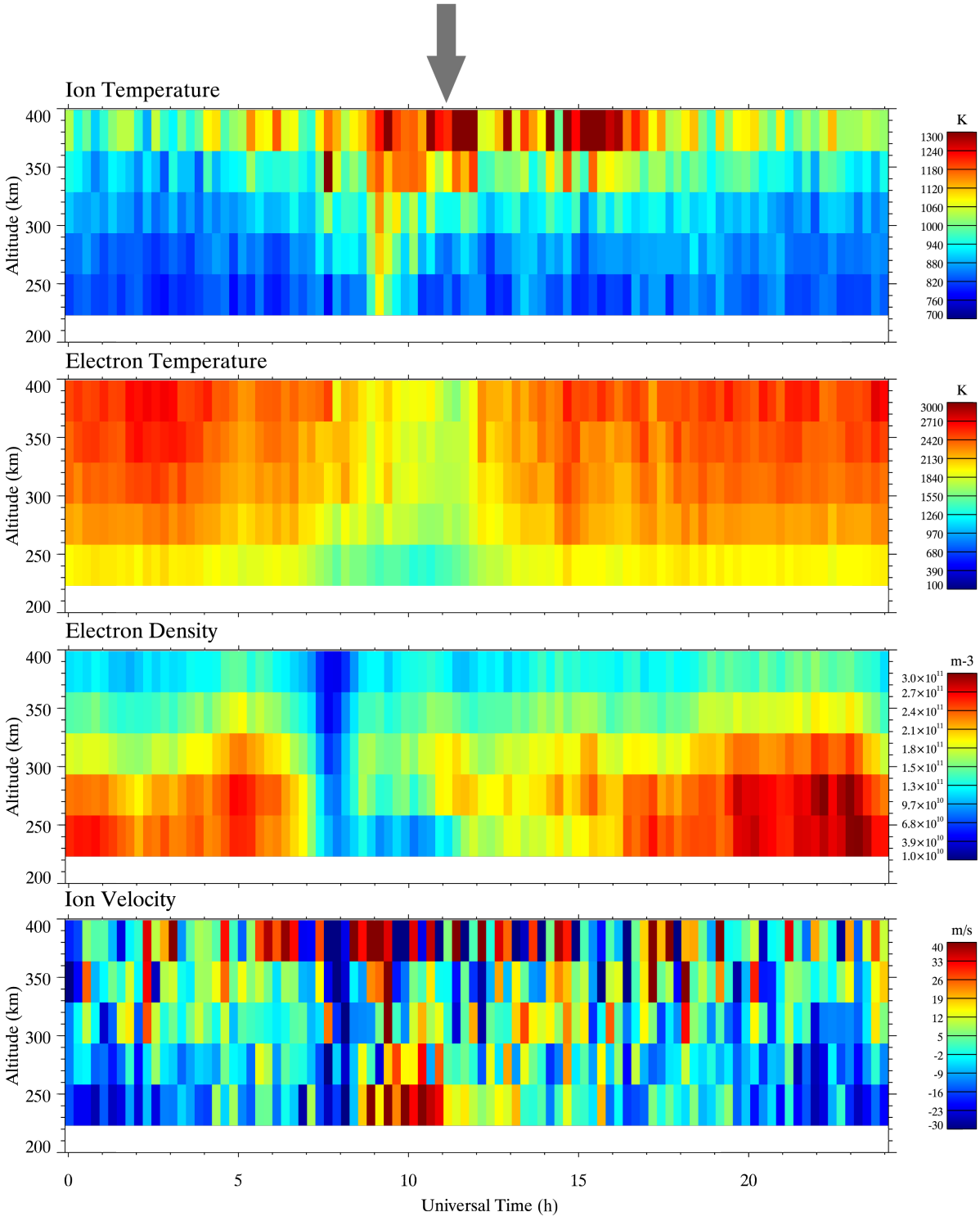

Figure A.1: RTI plots of parameters with 15-minute integration bins on 28/June/2007. (Top panel) T_i. (Second panel from the top) T_e. (Third panel from the top) n_e. (Bottom panel) V_i, positive values are away from the radar. The arrow at the top indicates the approximate location of local midnight in Magnetic Local Time (MLT) coordinates (11:20 UT).

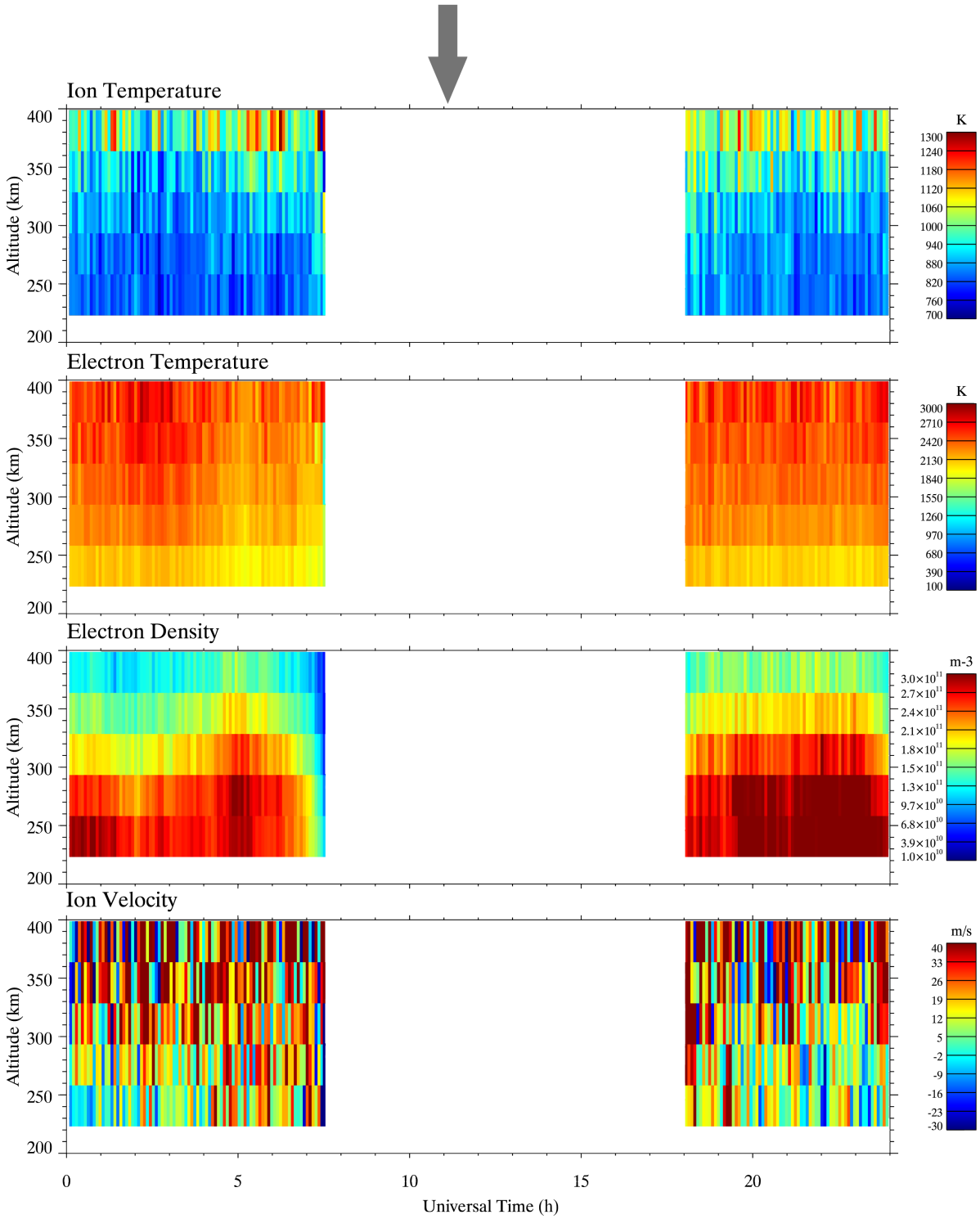

Figure A.2: Same as Figure A.1 but with a 5-minute resolution.

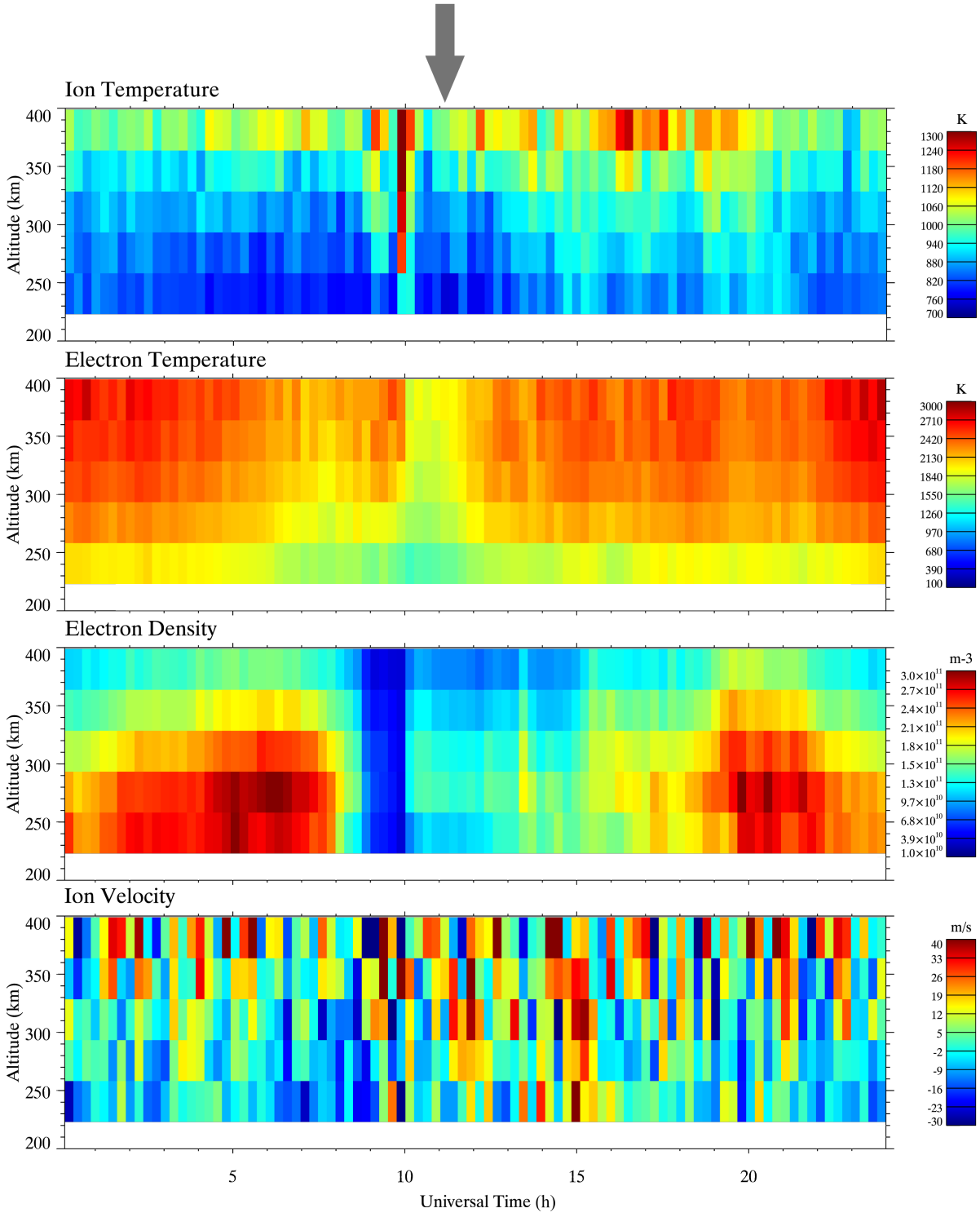

Figure A.3: RTI plots of parameters with 15-minute integration bins on 29/June/2007. (Top panel) T_i. (Second panel from the top) T_e. (Third panel from the top) n_e. (Bottom panel) V_i, positive values are away from the radar. The arrow at the top indicates the approximate location of local midnight in Magnetic Local Time (MLT) coordinates (11:20 UT).

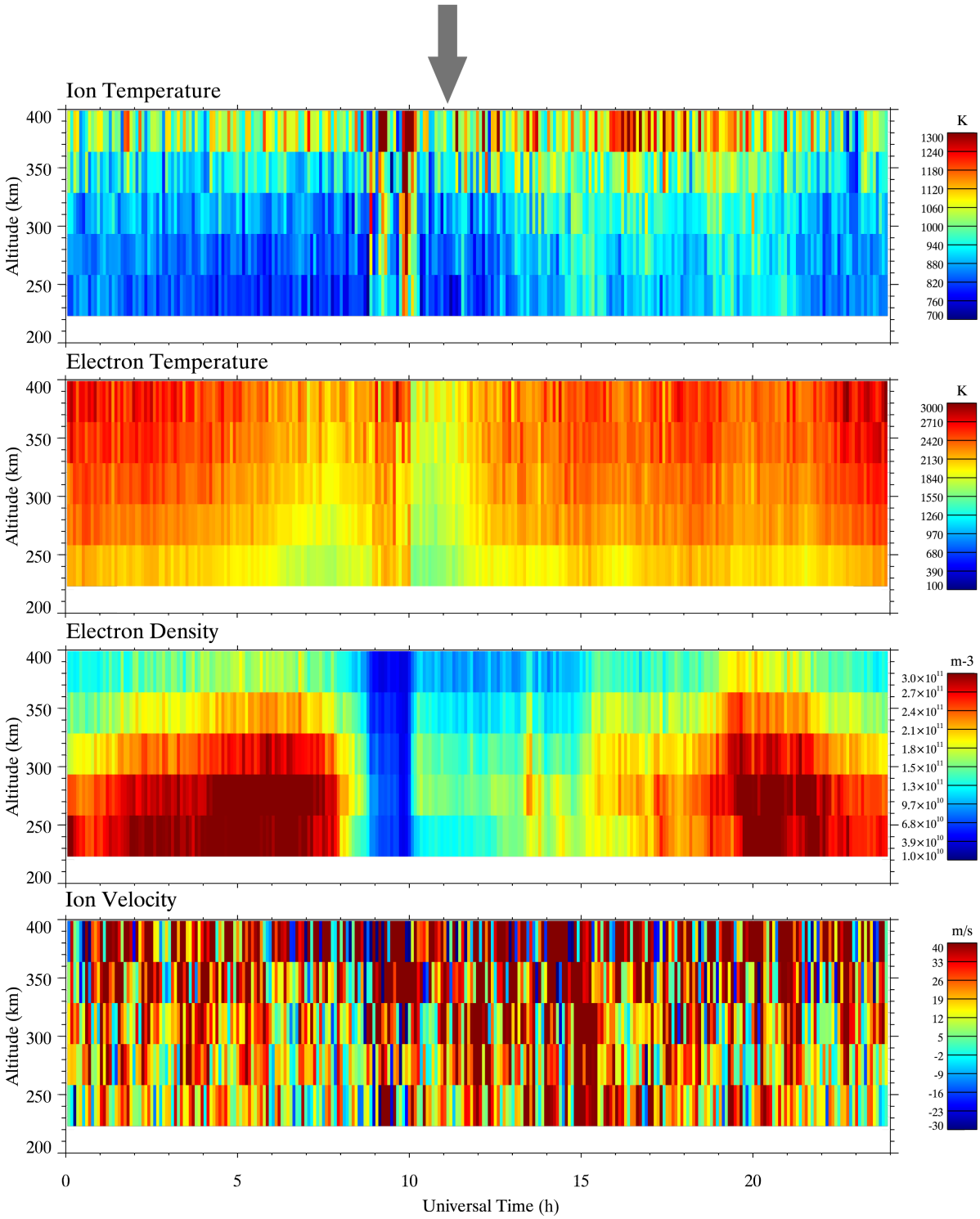

Figure A.4: Same as Figure A.3 but with a 5-minute resolution.

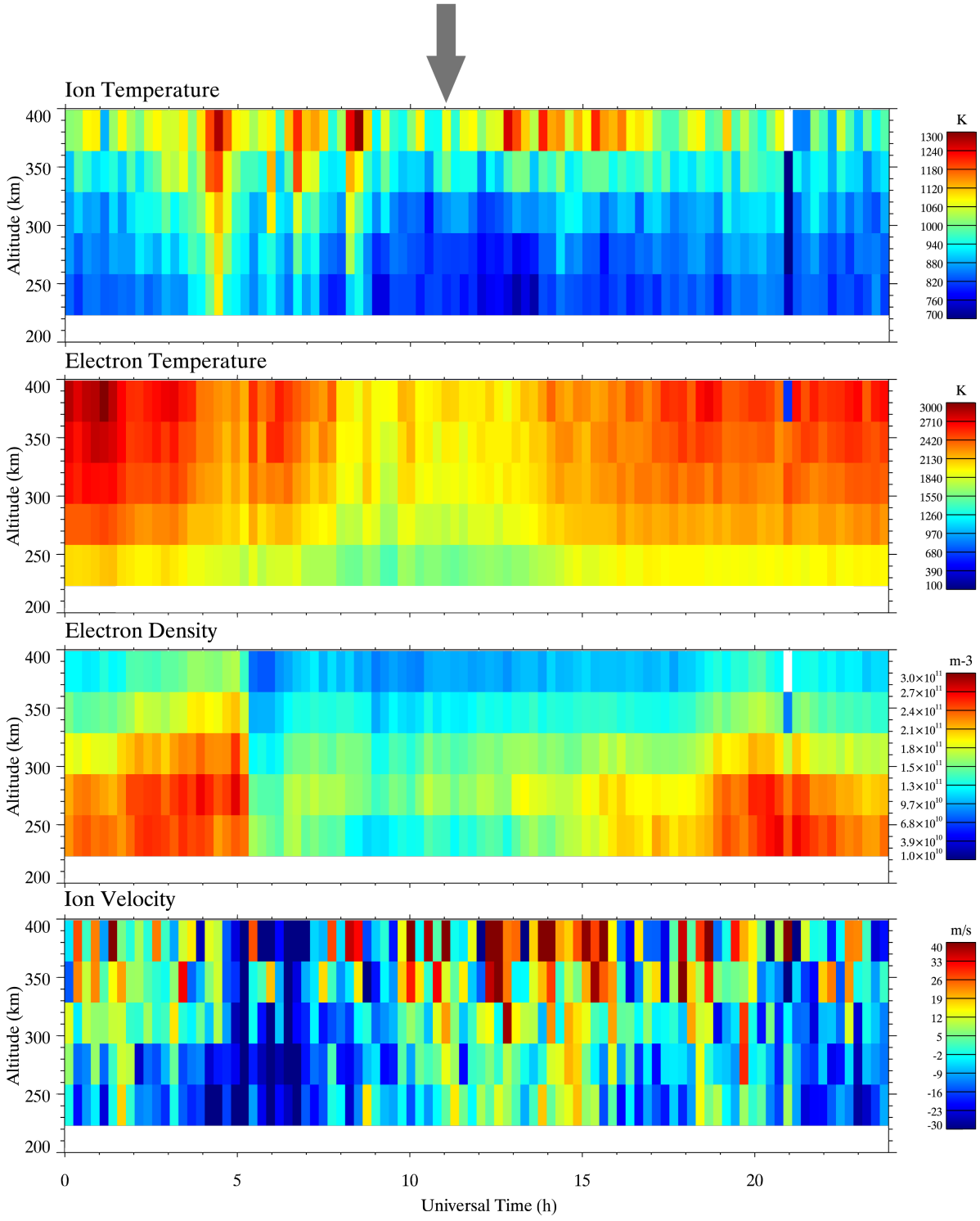

Figure A.5: RTI plots of parameters with 15-minute integration bins on 30/June/2007. (Top panel) T_i. (Second panel from the top) T_e. (Third panel from the top) n_e. (Bottom panel) V_i, positive values are away from the radar. The arrow at the top indicates the approximate location of local midnight in Magnetic Local Time (MLT) coordinates (11:20 UT).

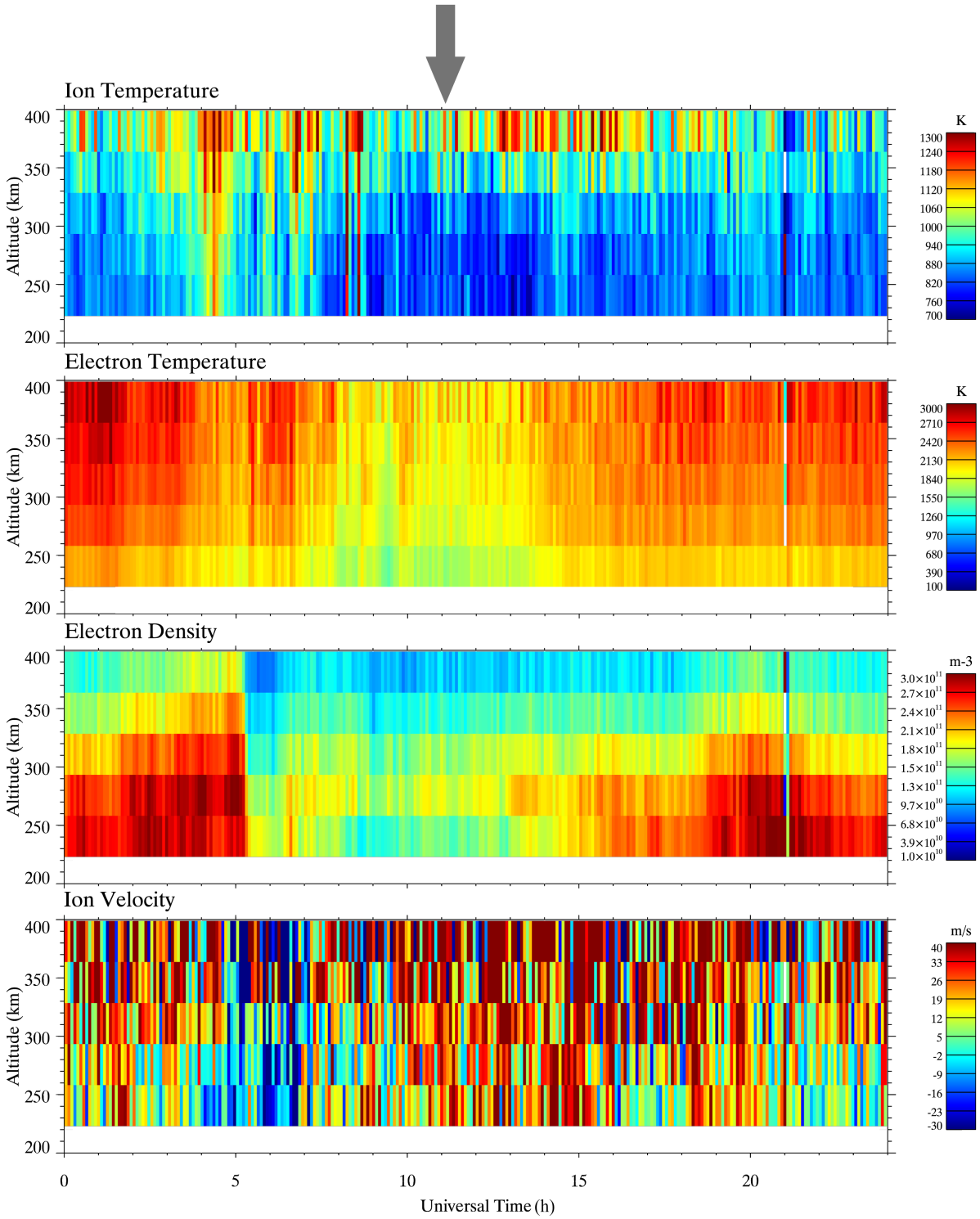

Figure A.6: Same as Figure A.5 but with a 5-minute resolution.

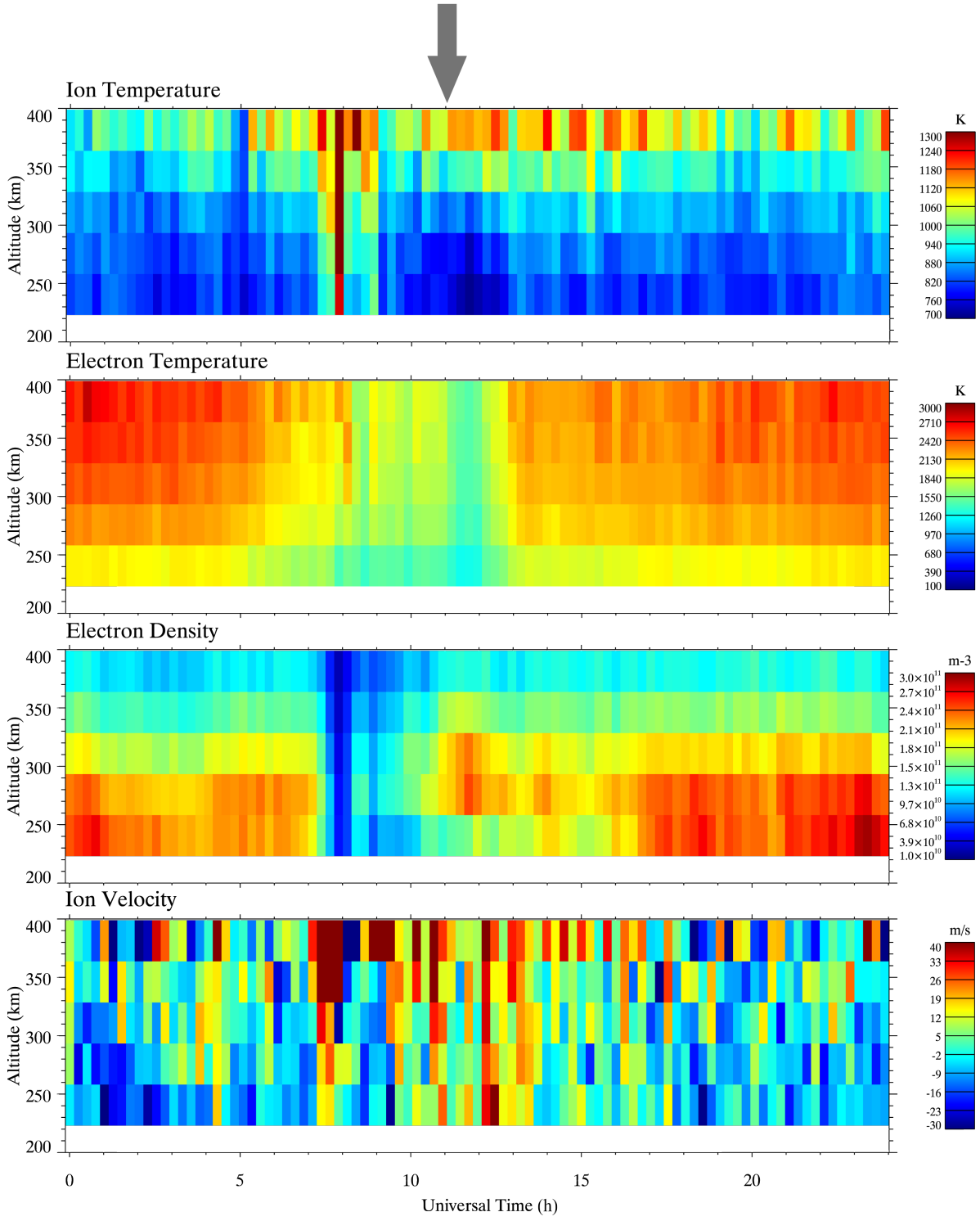

Figure A.7: RTI plots of parameters with 15-minute integration bins on 1/July/2007. (Top panel) T_i. (Second panel from the top) T_e. (Third panel from the top) n_e. (Bottom panel) V_i, positive values are away from the radar. The arrow at the top indicates the approximate location of local midnight in Magnetic Local Time (MLT) coordinates (11:20 UT).

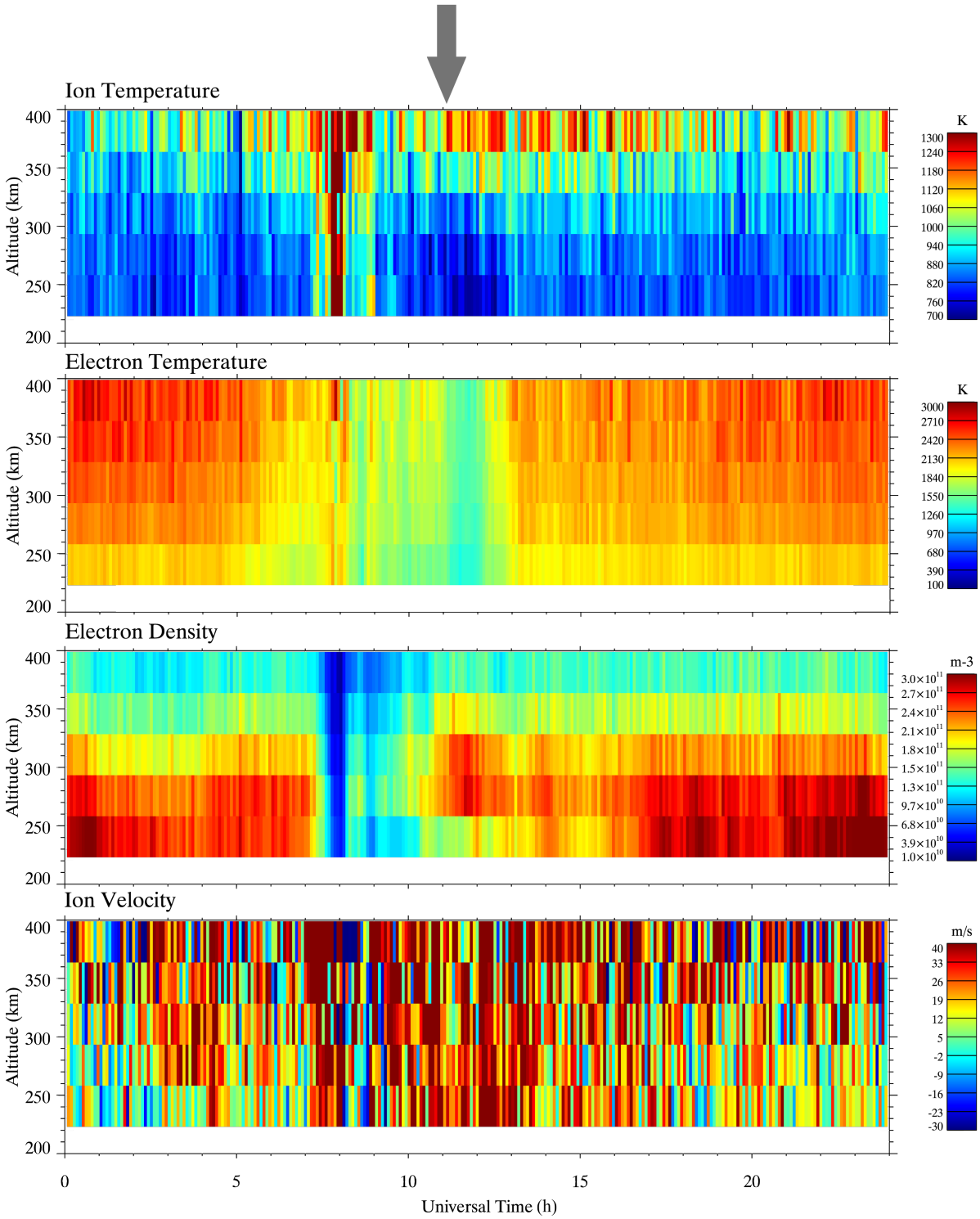

Figure A.8: Same as Figure A.7 but with a 5-minute resolution.

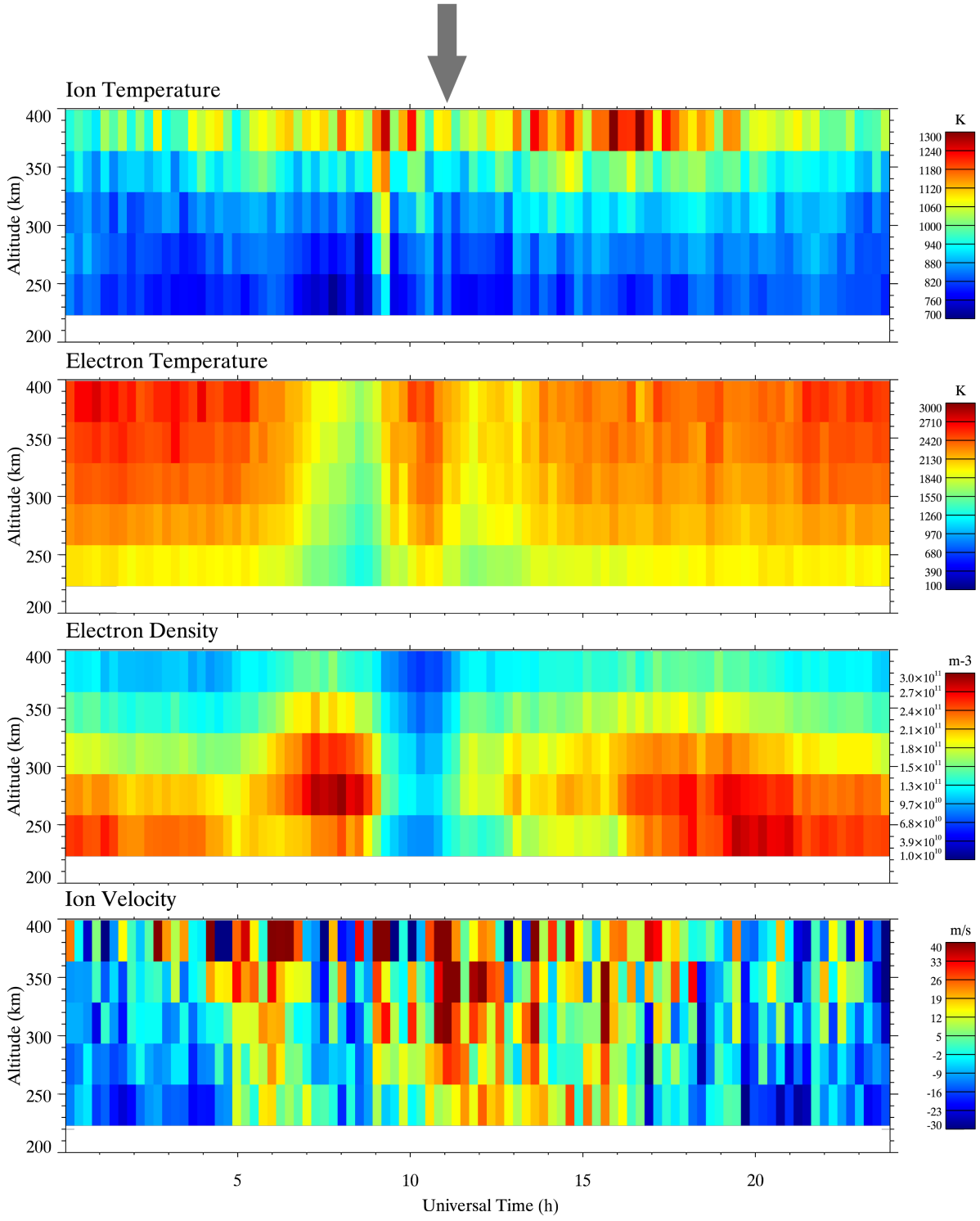

Figure A.9: RTI plots of parameters with 15-minute integration bins on 2/July/2007. (Top panel) T_i. (Second panel from the top) T_e. (Third panel from the top) n_e. (Bottom panel) V_i, positive values are away from the radar. The arrow at the top indicates the approximate location of local midnight in Magnetic Local Time (MLT) coordinates (11:20 UT).

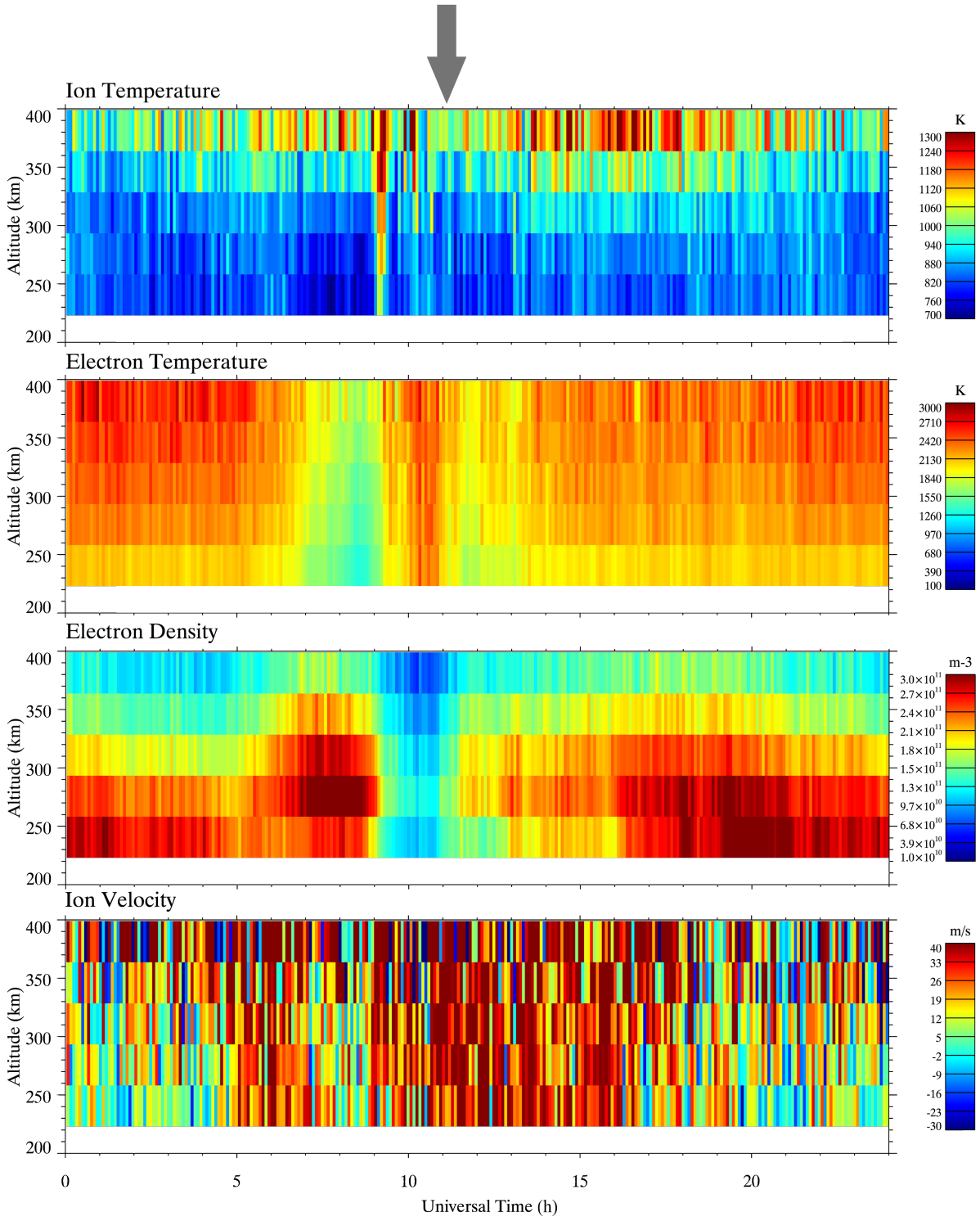

Figure A.10: Same as Figure A.9 but with a 5-minute resolution.

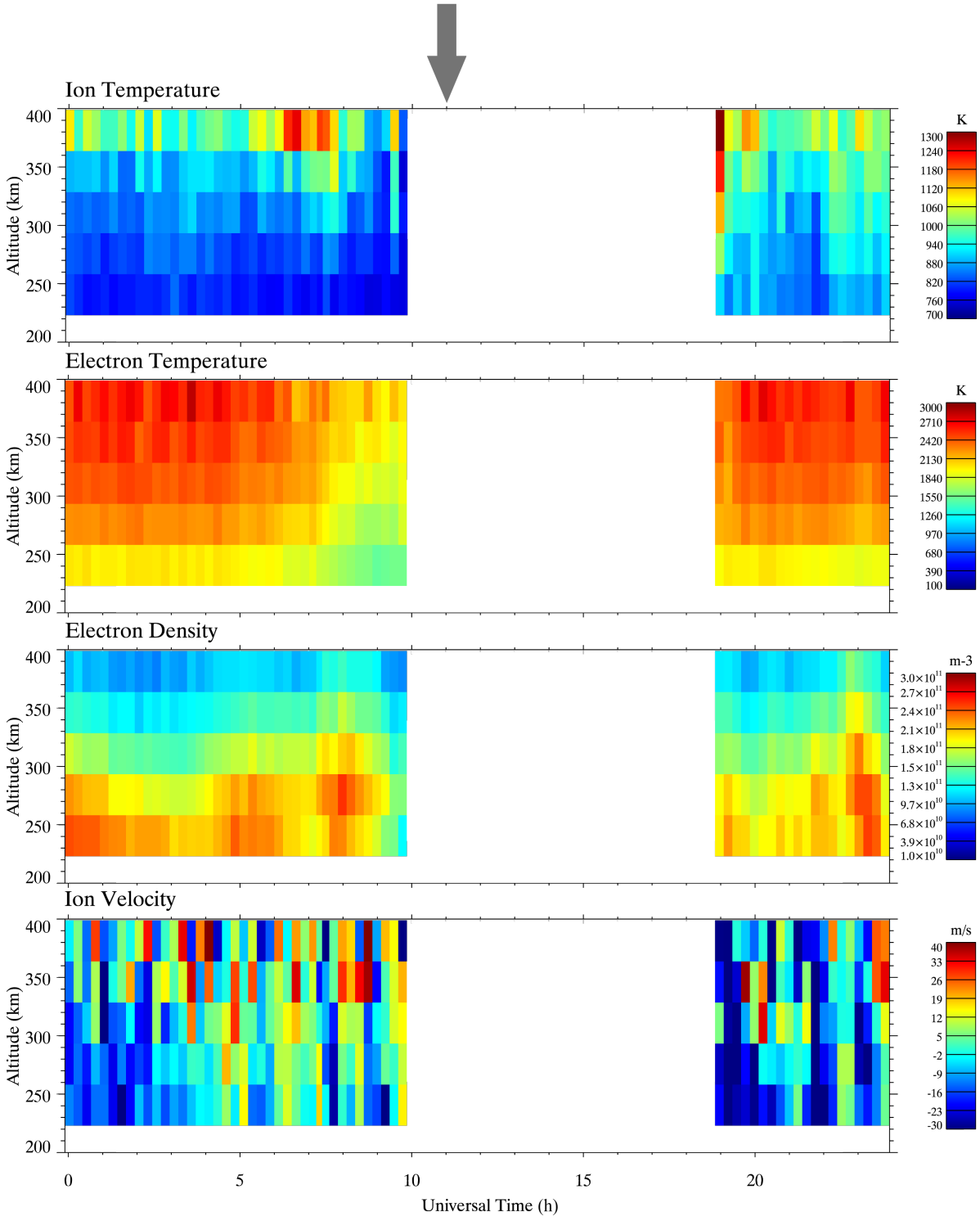

Figure A.11: RTI plots of parameters with 15-minute integration bins on 3/July/2007. (Top panel) T_i. (Second panel from the top) T_e. (Third panel from the top) n_e. (Bottom panel) V_i, positive values are away from the radar. The arrow at the top indicates the approximate location of local midnight in Magnetic Local Time (MLT) coordinates (11:20 UT).

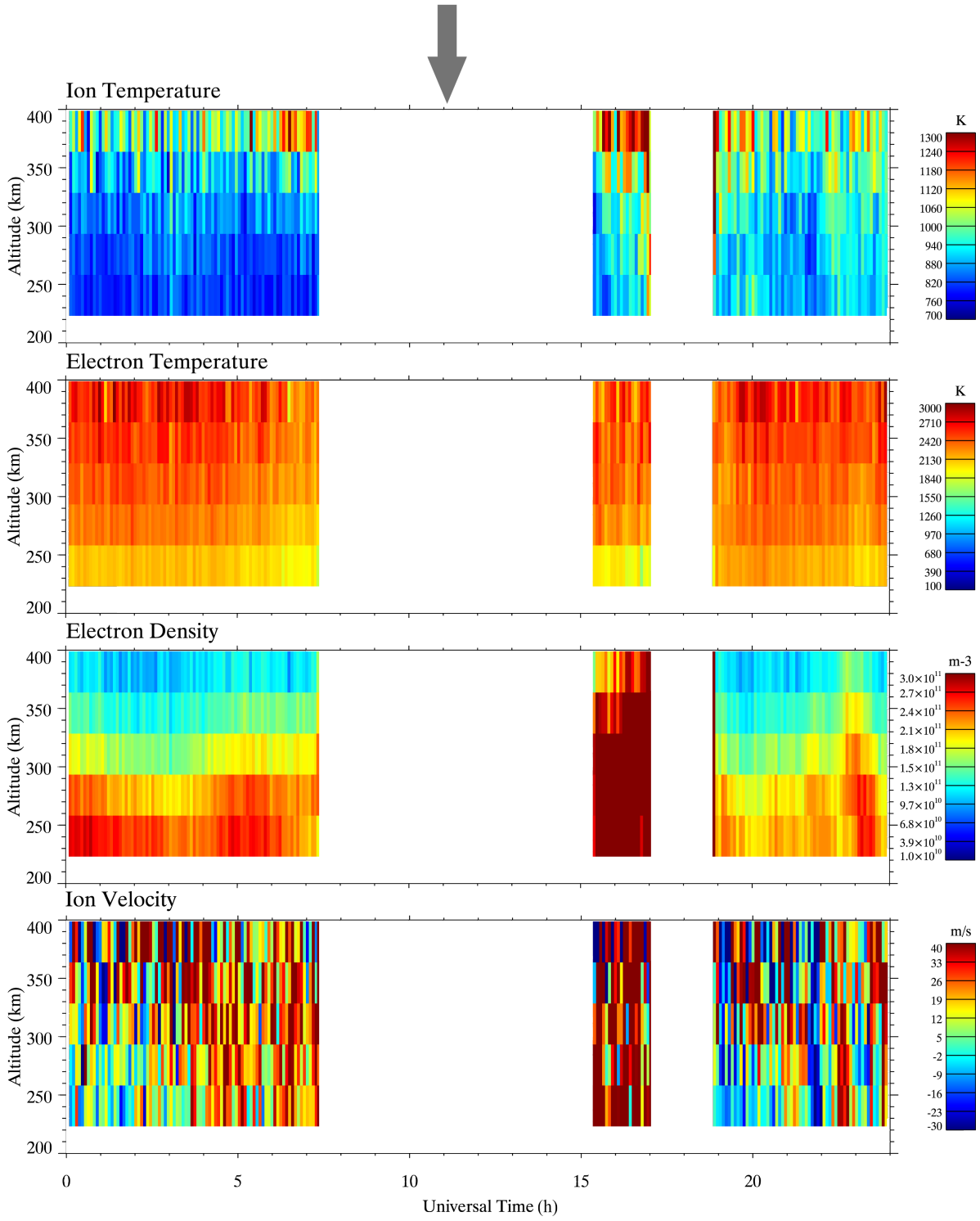

Figure A.12: Same as Figure A.11 but with a 5-minute resolution.

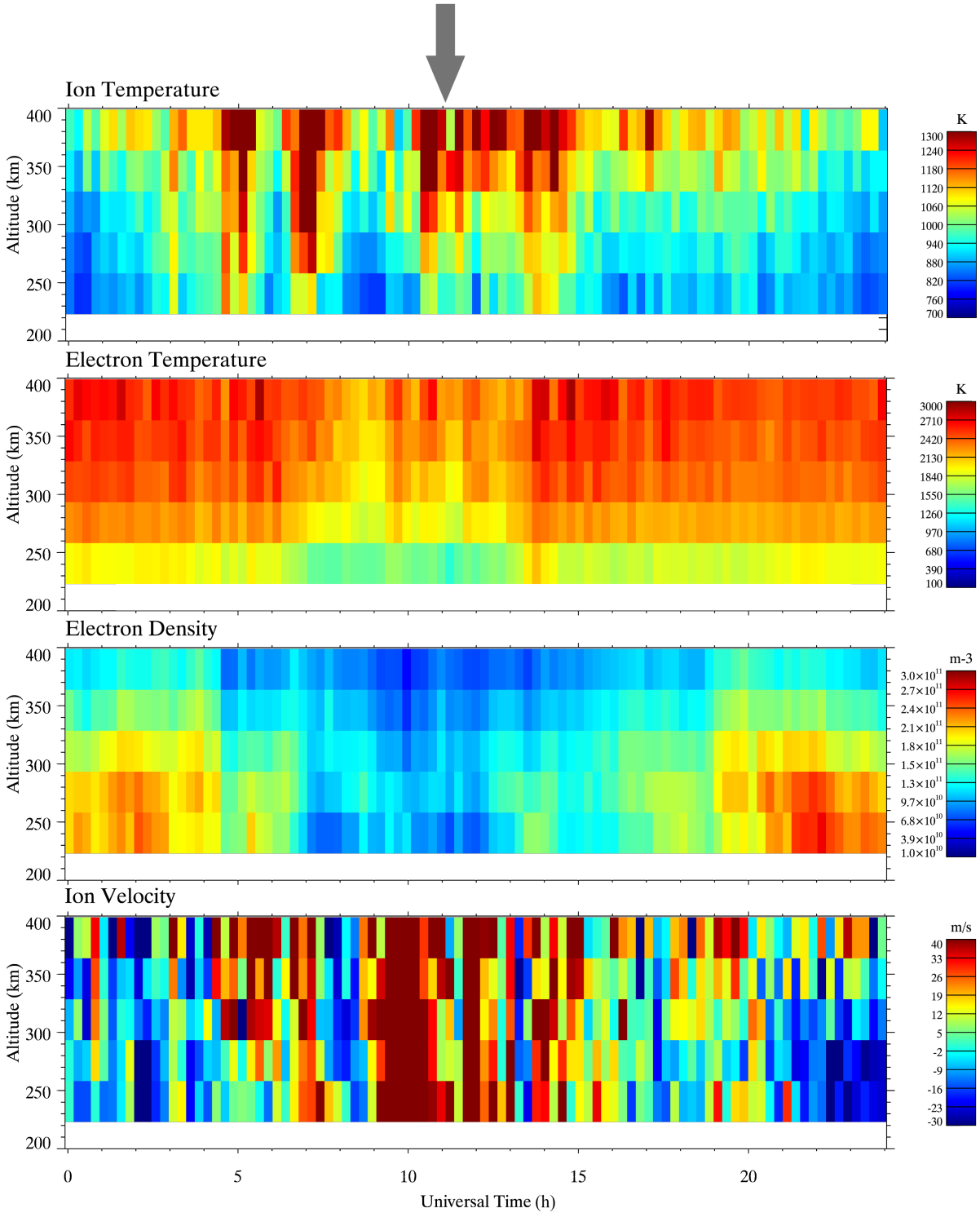

Figure A.13: RTI plots of parameters with 15-minute integration bins on 4/July/2007. (Top panel) T_i. (Second panel from the top) T_e. (Third panel from the top) n_e. (Bottom panel) V_i, positive values are away from the radar. The arrow at the top indicates the approximate location of local midnight in Magnetic Local Time (MLT) coordinates (11:20 UT).

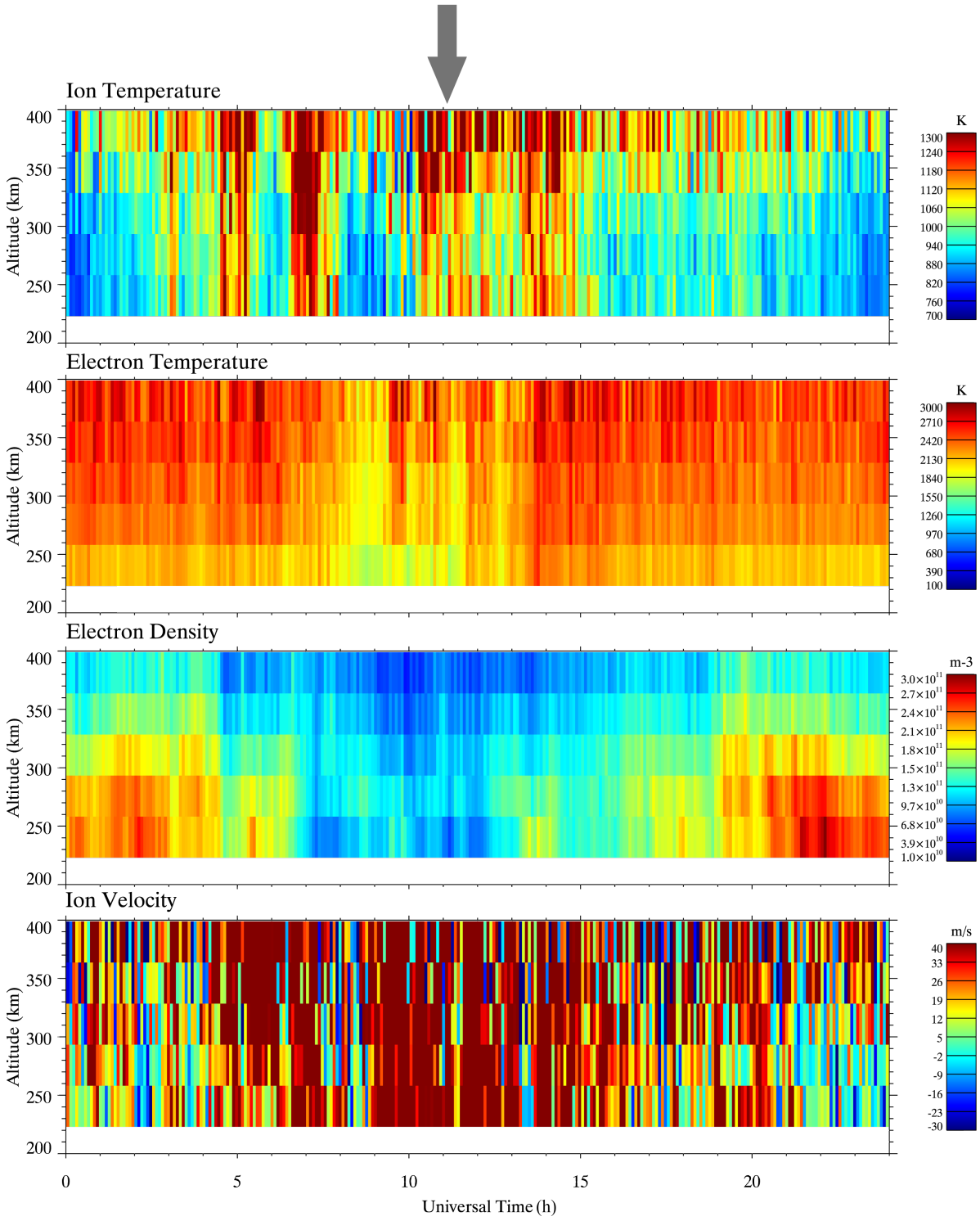

Figure A.14: Same as Figure A.13 but with a 5-minute resolution.

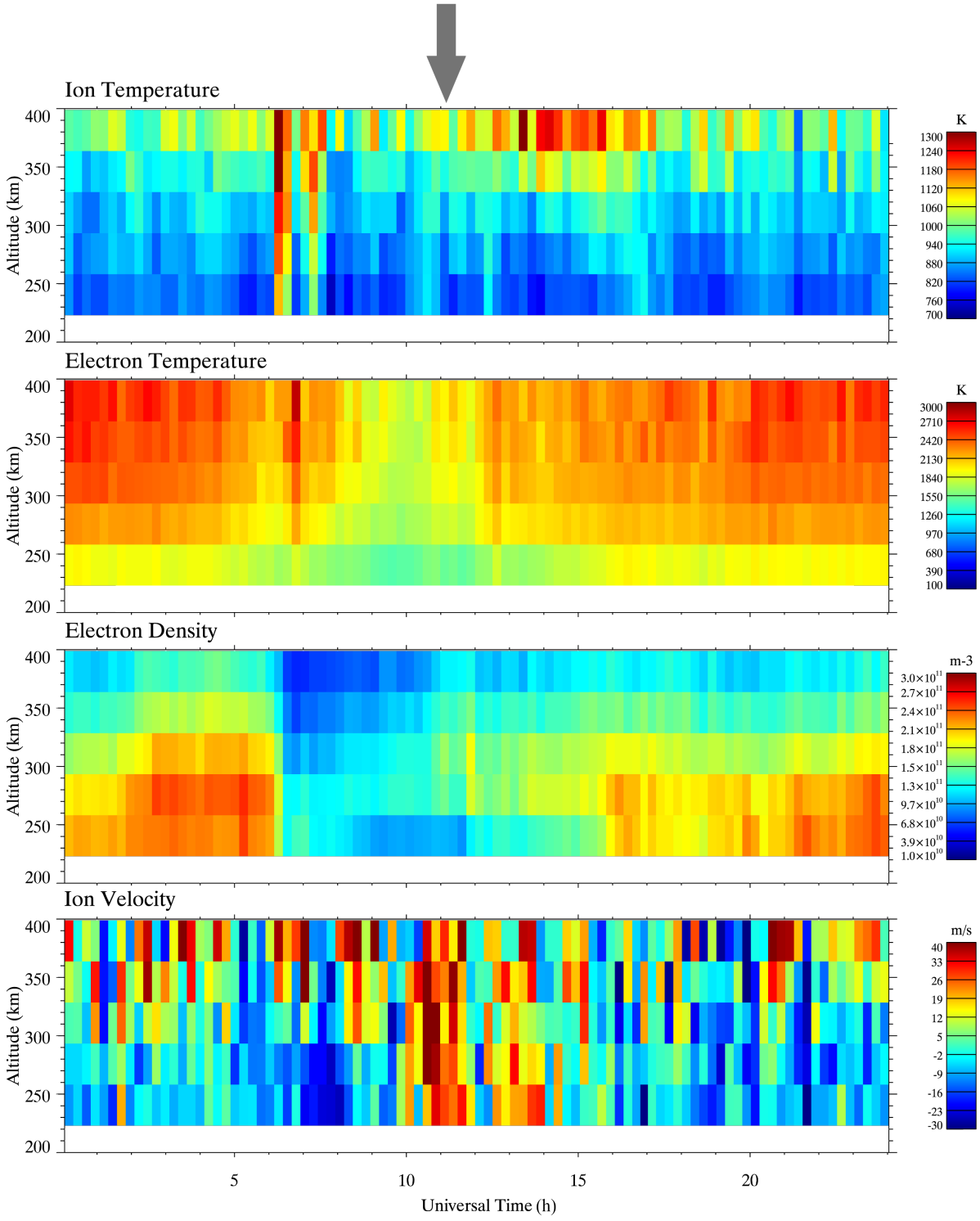

Figure A.15: RTI plots of parameters with 15-minute integration bins on 5/July/2007. (Top panel) T_i. (Second panel from the top) T_e. (Third panel from the top) n_e. (Bottom panel) V_i, positive values are away from the radar. The arrow at the top indicates the approximate location of local midnight in Magnetic Local Time (MLT) coordinates (11:20 UT).

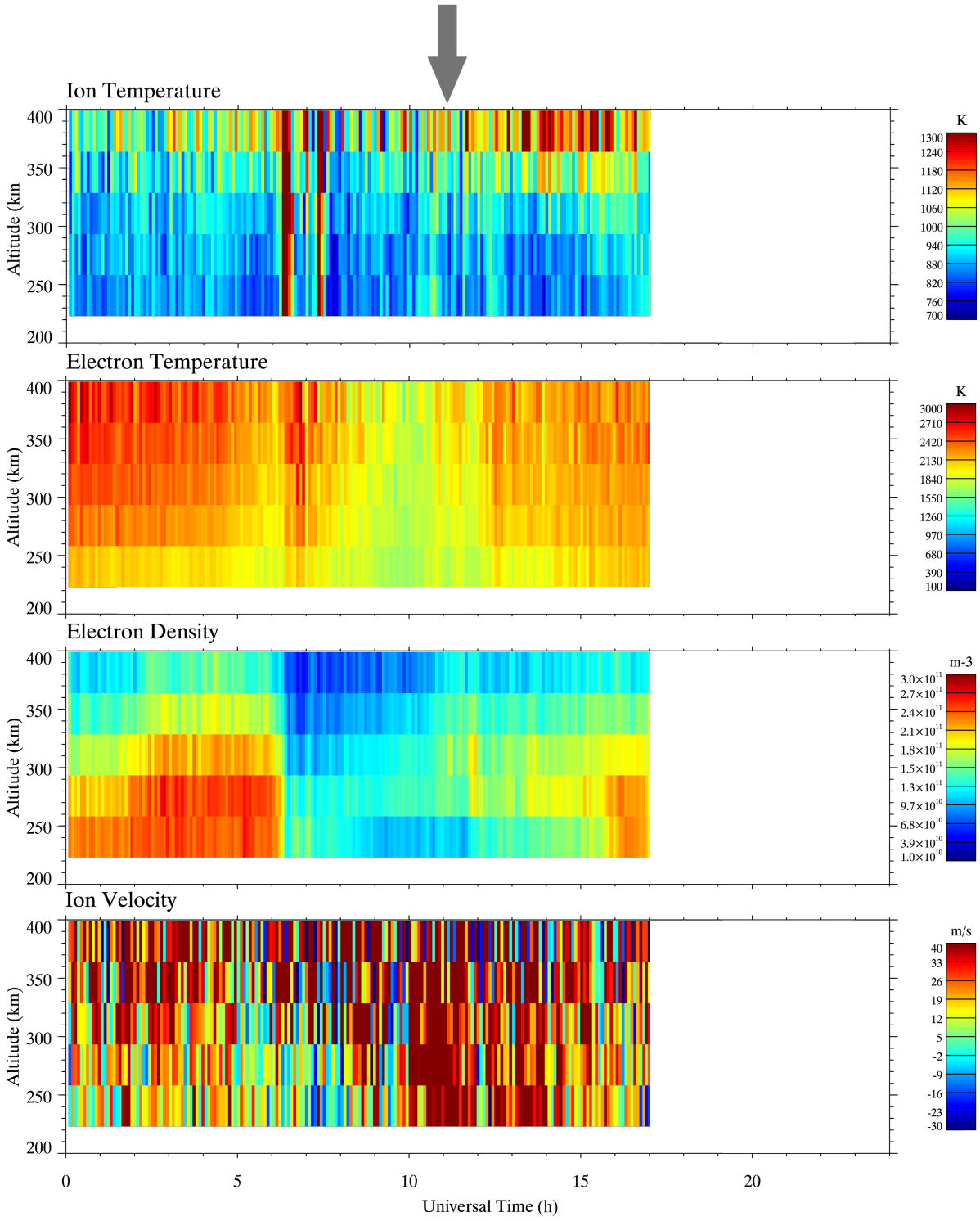

Figure A.16: Same as Figure A.15 but with a 5-minute resolution.

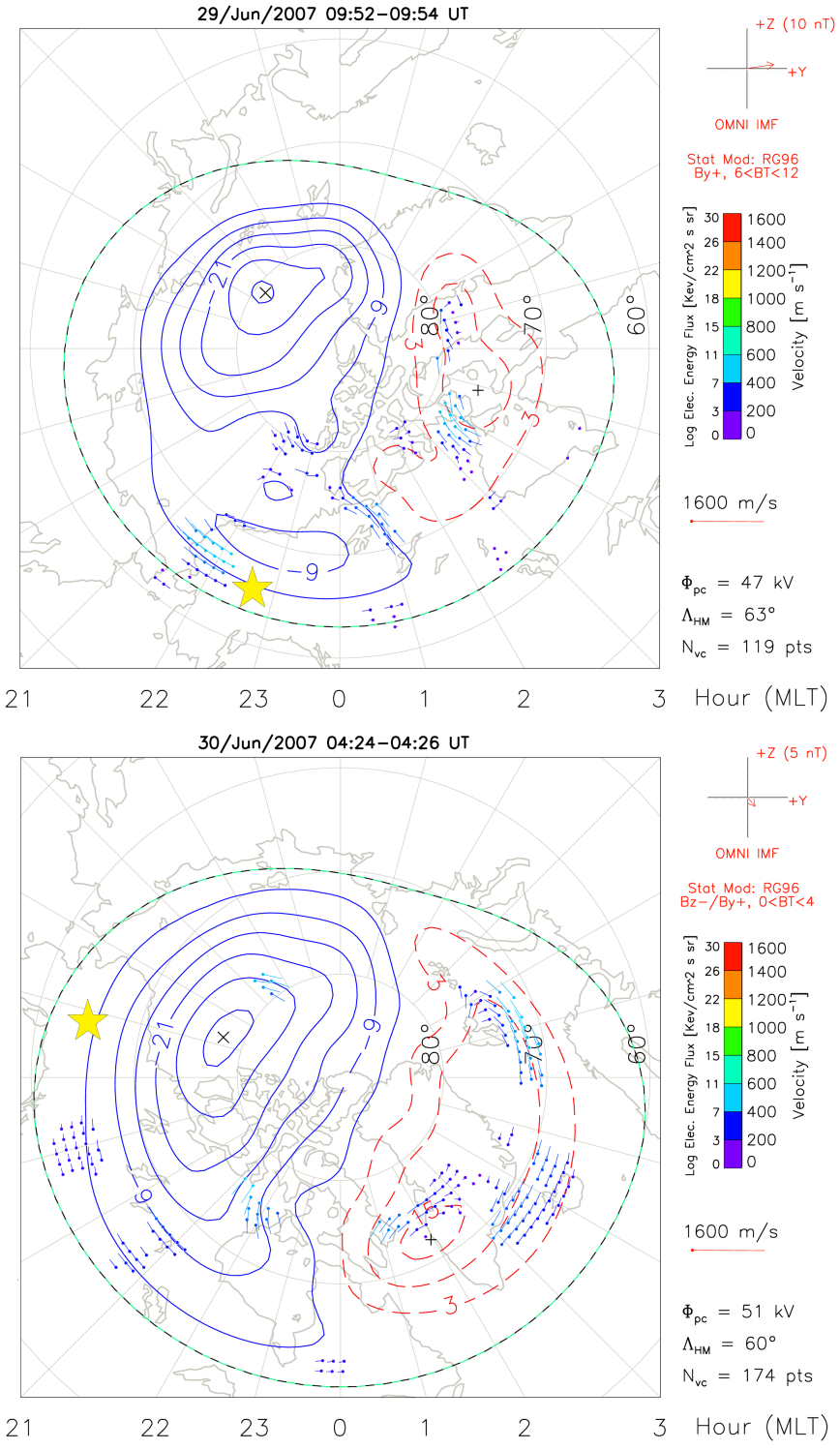

Figure A.17: SuperDARN potential maps for 29/June/2007 and 30/June/2007 at the time of a T_i enhancement. The gold star indicates PFISRs location, while the red and blue circles relate to potential.

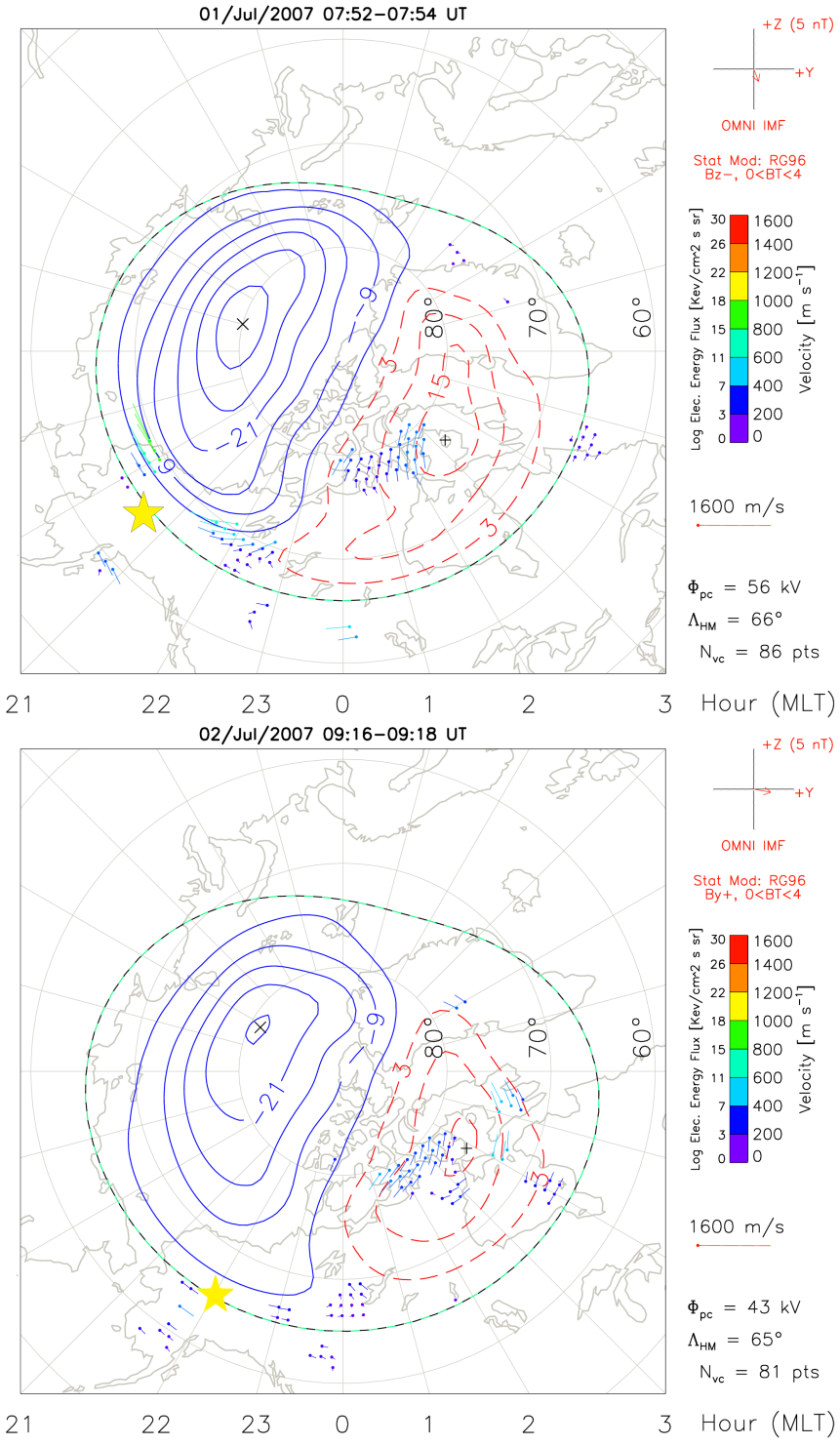

Figure A.18: SuperDARN potential maps for 1/July/2007 and 2/July/2007 at the time of a T_i enhancement. The gold star indicates PFISRs location, while the red and blue circles relate to potential.

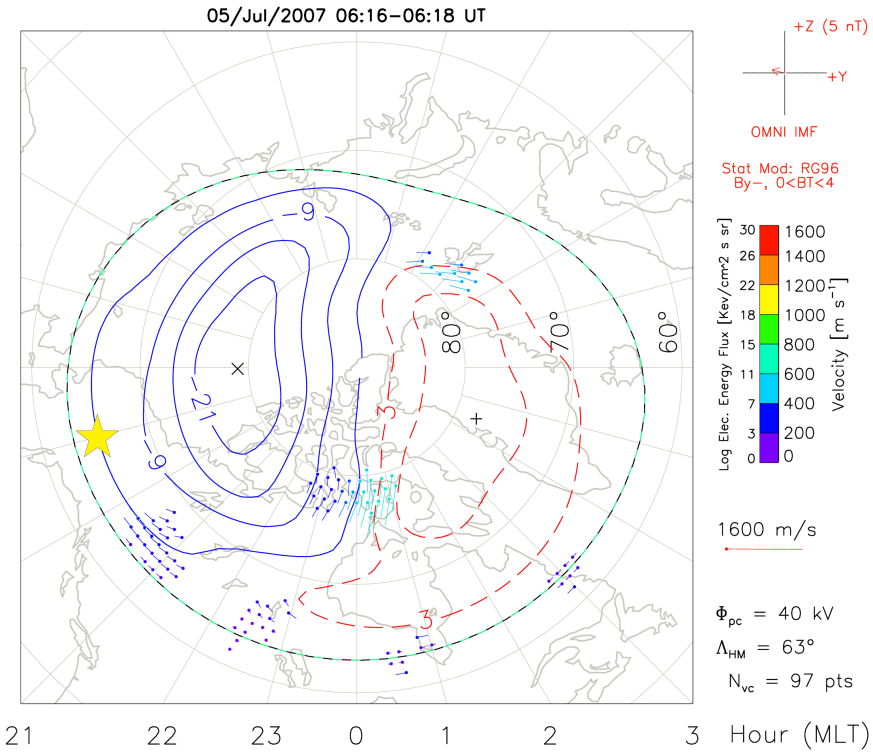

Figure A.19: SuperDARN potential map for 5/July/2007 at the time of a T_i enhancement. The gold star indicates PFISRs location, while the red and blue circles relate to potential.